MULTI-DIRECTIONAL PHASE-CONTRAST FLOW MRI IN REAL TIME

Dissertation
for the award of the degree
"Doctor rerum naturalium"
of the Georg-August-Universität Göttingen

within the doctoral program
Physics of Biological and Complex Systems
of the Georg-August University School of Science (GAUSS)

submitted by

JOST MICHAEL KOLLMEIER
Göttingen, Germany

Thesis Committee

First referee and supervisor

Prof. Dr. Jens Frahm
Biomedizinische NMR
Max-Planck-Institut für biophysikalische Chemie, Göttingen

Second referee

Prof. Dr. Jörg Enderlein
Biophysik / Komplexe Systeme, III. Physikalisches Institut
Georg-August-Universität Göttingen

Prof. Dr. Ulrich Parlitz
Biomedizinische Physik
Max-Planck-Institut für Dynamik und Selbstorganisation, Göttingen

External Referees

Third referee

Prof. Dr. Klaus Scheffler
Abteilung für Hochfeld-Magnetresonanz
Max-Planck-Institut für biologische Kybernetik, Tübingen

Examination Board

Prof. Dr. Jens Frahm

Prof. Dr. Jörg Enderlein

Prof. Dr. Ulrich Parlitz

Prof. Dr. Eberhard Bodenschatz
Fluidphysik, Strukturbildung und Biokomplexität
Max-Planck-Institut für Dynamik und Selbstorganisation, Göttingen

Prof. Dr. Thorsten Hohage
Inverse Probleme, Institut für Numerische und Angewandte Mathematik
Georg-August-Universität Göttingen

Prof. Dr. Helmut Grubmüller
Theoretische und Computergestützte Biophysik
Max-Planck-Institut für biophysikalische Chemie, Göttingen

Date of oral examination: 31 August 2020

TABLE OF CONTENTS

ACRONYMS

CSF	cerebrospinal fluid
FFT	Fast Fourier Transform
FLASH	Fast Low Angle Shot
IRGNM	Iteratively Regularized Gauss Newton Method
MBR	model-based reconstruction
1dMBR	model-based reconstruction for uni-directional flow
mdMBR	model-based reconstruction for multi-directional flow
minTE	minimal TE velocity encoding
MRI	magnetic resonance imaging
NLINV	non-linear inversion
NMR	nuclear magnetic resonance
PC	phase-contrast
RT	real-time
RF	radio-frequency
SFD	smoothing of flow direction
SVE	shared velocity encoding
TE	echo time
TR	repetition time
TV	total variation
VENC	velocity encoding
VNR	velocity to noise ratio
0^{th}GM	zeroth gradient moment
1^{st}GM	first gradient moment

1 INTRODUCTION

Magnetic resonance imaging (MRI) is a potent and versatile imaging technique that has become an indispensable part of clinical diagnostics. In particular, its exceptional soft-tissue contrast and non-invasive nature contribute to the success of this unique imaging modality.
The strength of MRI, further, is due to a large variety of image contrasts based on its sensitivity to different physical quantities. These include the proton density, tissue relaxation times and motion in a general context. More specifically, modern MRI techniques allow imaging of diffusion properties, perfusion effects or, as outlined in this work, the quantification of flow velocities. The underlying technique, phase-contrast (PC) MRI, is a well-established method for the quantitative assessment of blood flow that gives valuable insights in cardiovascular pathologies [1]. Unlike Doppler sonography, PC MRI offers free choice of imaging plane orientation without the need for an acoustic window and the option to quantify velocities in multiple and arbitrary directions.

A major limitation of all MRI applications is the fact that MRI is intrinsically slow. Its line-wise sampling in Fourier space demands repeated excitations of nuclear spins according to the principle of nuclear magnetic resonance (NMR). The excitation rates, on the other hand, are limited by hardware restrictions and waiting times for magnetization recovery, resulting in common temporal resolutions in the order of seconds.

PC MRI suffers even more from temporal limitations, as it requires at least twice as many acquisitions per velocity map compared to standard anatomical MRI. To obtain quantitative velocity maps of adequate spatio-temporal resolution, cardiovascular PC imaging is usually accomplished by ECG-synchronized data acquisitions that average flow information over multiple heart cycles. Such a data-sorting approach, however, naturally comes with limited applicability to irregular heart beats, e.g. observed during arrhythmia, and lacks access to other physiological dynamics such as bulk motion or respiration. Moreover, as multiple heart cycles are required to synthesize an artificial heart beat, conventional PC acquisitions suffer from long acquisition times and often require breath holding.

Real-time (RT) MRI is a powerful alternative to overcome these limitations. It refers to continuous imaging at high temporal resolutions without the need for physiological gating or data sorting. For that reason, RT MRI allows access to (i) beat-to-beat variations and (ii) respiration and further offers (iii) robust imaging under motion and (iv) short scan times.
Originally introduced by Riederer et al. [2] the combination of RT and quantitative PC MRI benefited from the use of high-speed techniques such as echo-planar imag-

ing [3] or spiral data acquisitions [4, 5, 6]. Nevertheless, these imaging methods achieve relatively low spatio-temporal resolutions ($\leq$ 18 fps, $\geq 2.5 \times 2.5$ mm^2).
Considerable progress in RT MRI is made by means of highly undersampled radial acquisitions that are reconstructed iteratively by non-linear inversion [7]. The approach drastically increases the temporal scan efficiency of MRI and thus the temporal resolution of cross-sectional (2D) image series [8]. The basic approach was successfully exploited for RT PC flow MRI [9, 10] and the subsequent upgrade via model-based image reconstruction [11] accomplished quantitative velocity maps at exceptional spatio-temporal resolutions (39 fps, 1.5×1.5 mm^2).

Although technically well advanced, the highly accelerated RT PC MRI method is currently restricted to only one velocity direction perpendicular to the imaging plane (through-plane flow). Uni-directional in-plane flow or multi-directional velocity vectors are not accessible so far, even though three-dimensional velocity information is desired for an accurate evaluation of fluid dynamics [12] and previous studies hinted at its technical feasibility [13, 14].
The problem for multi-directional PC MRI, however, is its demand for additional acquisition time. While uni-directional PC imaging requires two individual scans, three-directional velocity imaging requires four. This fact renders multi-directional PC MRI more time-consuming and a respective RT realization challenging.

This work aims at the development of a PC MRI technique that achieves multi-directional velocity quantification in real time by exploiting highly undersampled radial acquisitions with time-efficient flow encoding and an iterative solution for the non-linear image reconstruction problem.
Opening with a brief overview on the basic principles of PC and RT MRI (Chapter 2) this thesis presents the uni-directional flow technique in Chapter 3 followed by proposals for further improvements. Chapter 4 describes the development of a multi-directional extension and its optimization towards high spatio-temporal resolutions, while Chapter 5 proposes further methodological refinements. Chapter 6 addresses the technical accuracy and presents a correction strategy to eliminate background phase errors by concomitant magnetic fields [15] which in its original form was not applicable to radial RT MRI. In vitro and in vivo results of the novel imaging methodology are demonstrated in Chapter 7 and Chapter 8 concludes with a summary and outlook.

2

BASICS

2.1 MAGNETIC RESONANCE IMAGING

MRI was introduced in 1973 by Paul Lauterbur [16] and since then undergoes an ongoing methodological development. The underlying concept comprises the following three essential components:

STATIC MAGNETIC FIELD: A static magnetic field B_0 introduces an energy gap between spin-up and spin-down quantum mechanical states of hydrogen nuclei which for an ensemble of spins results in a macroscopic magnetic moment aligned with the external field B_0.

RADIO-FREQUENCY PULSE: Following the concept of NMR, a radio-frequency (RF) pulse is used to excite nuclei by switching their spin states. As a result the macroscopic magnetization vector tilts towards the transversal plane (perpendicular to B_0) where it performs a precession. According to the laws of electromagnetic induction the precessing magnetization induces an electrical current in nearby receiver coils. This current constitutes the fundamental signal of MRI.

MAGNETIC FIELD GRADIENTS: In order to spatially allocate the MRI signal, magnetic field gradients G are used. By spatially (and temporally) adjusting the magnetic field, the Lamorfrequency ω_L of the precessing magnetization vector is controlled as described in Equation 2.1. This link between spin position r and its precession frequency describes the key principle of signal localization for the creation of an MR image.

$$\omega_L(r) = \gamma(B_0 + G\,r) \tag{2.1}$$

Here, γ denotes the nucleus-specific gyromagnetic ratio. Based on this elementary relationship, the three spatial dimensions can be encoded by sequential gradient switching on all three physical axes. Their temporal order is illustrated in Figure 2.1 showing the basic pulse sequence diagram used throughout this work.

Cross-sectional (2D) imaging relies on a slice-selection gradient played out parallel to the selective RF excitation pulse with frequency $\omega_L(r)$. As a result, the resonance condition is only fulfilled for a two-dimensional plane and thus only the spins in this slice are excited. Neighboring nuclei show different Lamor frequencies causing their spins to remain in equilibrium.
The excited slice is subjected to a spin echo [17] or gradient echo [18] generating a signal response recorded in receiver coils. At the same time, read gradients provide encoding of the two remaining spatial dimensions. As illustrated in Figure 2.1, the combination of x and y-gradients specifies a projection direction along which the

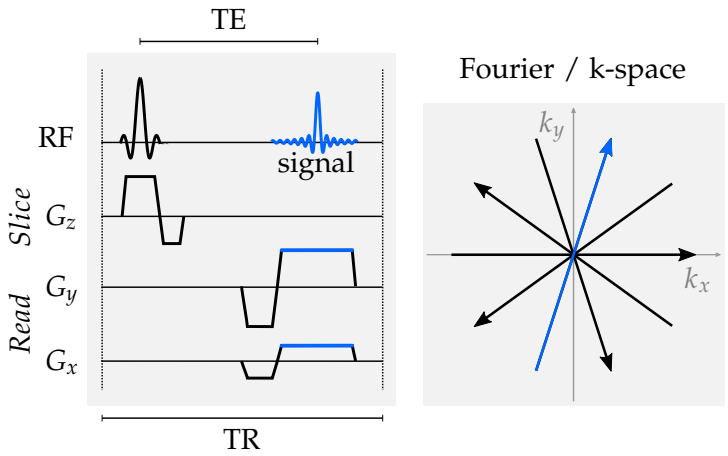

Figure 2.1: Sequence diagram and radial sampling in Fourier space. The gradient amplitudes during signal acquisition *(blue)* determine the spoke orientation in k-space.

frequencies of the MRI signal are modulated according to Equation 2.1. This way, the acquired signal represents the Fourier-transform of the desired image along the specified direction. To obtain the full image, the excitation and read-out process is repeated with rotating projection directions until the whole Fourier-space, also known as k-space, is sampled line-by-line. Finally, the image is obtained by a 2D inverse Fourier transformation.

The basic principle of line-wise k-space sampling is fundamental in MRI. Nevertheless, different sampling trajectories are possible. Phase encoding as used for more frequent Cartesian k-space sampling or for volumetric (3D) imaging is not exploited in this work and instead well document in [19].

The image contrast of MRI is mainly based on varying spin densities and differences in the magnetization relaxation, summarized by the phenomenological Bloch Equations:

$$\frac{\mathrm{d}}{\mathrm{d}t}\vec{M}(t) = \gamma\left[\vec{M}(t) \times \vec{B}(t)\right] - \begin{pmatrix} \frac{M_x(t)}{T_2} \\ \frac{M_y(t)}{T_2} \\ \frac{M_z(t)-M_0}{T_1} \end{pmatrix} \tag{2.2}$$

The first part describes the precession of the magnetization vector $\vec{M}$, while the second part refers to a longitudinal recovery towards the equilibrium magnetization M_0 and a simultaneous decay of transversal magnetization. The two exponential processes are characterized by the time constants T_1 and T_2, respectively.

The question which parameter dominates the image contrast is determined by the sequence type and more specifically by the echo time (TE) and the repetition time (TR), both illustrated in Figure 2.1. Using the Fast Low Angle Shot (FLASH) sequence [18] with small flip angles and thus short TE and TR this work exclusively covers T_1-weighted images.

2.2 PHASE-CONTRAST MRI

PC MRI provides quantitative assessment of flow velocities by utilizing the phase of the complex MRI signal. Originally introduced by E. L. Hahn [20], PC MRI has evolved to a prominent branch of quantitative MRI in clinical diagnostics [21, 1]. The underlying principles rely on additional magnetic field gradients that imprint a phase ϕ according to:

$$\phi(\tau) = \gamma \int_0^\tau G(t)\, x(t) \mathrm{d}t \tag{2.3}$$

Here, $x(t)$ denotes the spin's trajectory which is expanded by a Taylor series to point out the dependency on the spin's velocity v.

$$\phi(\tau) = \gamma \int_0^\tau G(t)\ (x_0 + v\, t\ \ldots)\, \mathrm{d}t \tag{2.4}$$

$$= \gamma\, x_0 \underbrace{\int_0^\tau G(t) \mathrm{d}t}_{0^{th}\mathrm{GM}} + \gamma\, v \underbrace{\int_0^\tau t\, G(t) \mathrm{d}t}_{1^{st}\mathrm{GM}} + \ldots \tag{2.5}$$

The equation renders the zeroth gradient moment (0^{th}GM) and first gradient moment (1^{st}GM) decisive for velocity encoding and imposes specifications on the gradient design. A bipolar gradient as illustrated in Figure 2.2 fulfills the demands by nulling the 0^{th}GM (area under curve) and introducing a specific 1^{st}GM responsible for velocity encoding. While static spins show zero net phase, the velocity of moving spins is encoded linearly in the phase of their complex MRI signal.

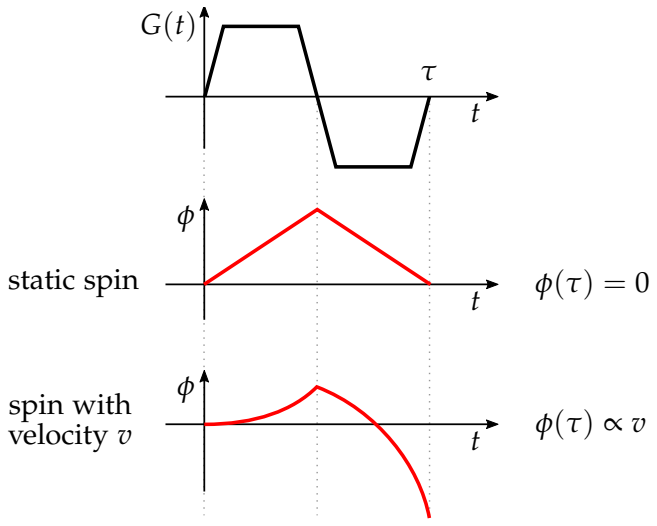

Figure 2.2: Bipolar gradient and phase evolution in PC MRI.

Beside the flow-encoding (FE) measurement, PC MRI requires the knowledge on the phase background Φ_0. This can be understood by the fact that the phase generally describes a relative quantity and the definition of phase zero in MRI is commonly affected by experimental inaccuracies such as off-resonances or field inhomogeneities.

Therefore, a reliable velocity determination relies on a second measurement usually given by a flow-compensating (FC) reference scan that determines Φ_0 using a 1^{st}GM of zero. Other variants of velocity encoding are addressed in Chapter 3 and 4.
The most decisive parameter in PC MRI, called velocity encoding (VENC), specifies the velocity field of view (in cm/s).

$$\text{VENC} = \frac{\pi}{\gamma \, \Delta 1^{st}\text{GM}} \tag{2.6}$$

Here, $\Delta 1^{st}$GM describes the 1^{st}GM-difference between the encoding steps. Serving as the proportionality factor between v and ϕ the VENC scales reciprocal to 1^{st}GM and directly affects the velocity to noise ratio (VNR). On the one hand, the VENC is favored small to maximize the VNR, while on the other hand, required to be large enough ($> v_{max}$) in order to avoid phase wraps at $\phi = \pm\pi$ [21].

2.3 REAL-TIME MRI

RT MRI based on undersampled radial FLASH and image reconstruction by iteratively regularized non-linear inversion (NLINV) achieves very high spatio-temporal resolutions due to a favorable combination of an effective data acquisition [22] and an advanced image reconstruction [7]. Both concepts are presented in the following.

2.3.1 *Acquisition: Undersampled Radial FLASH*

The basis for a fast MRI acquisitions is given by its sequence. The RT MRI relies on the gradient-echo based FLASH sequence exploiting small flip angles and spoiling by random RF phases [23]. In contrast to spin-echo based sequences, the FLASH technique allows rapid imaging due to short TE and TR. These short repetition times lay the foundation for fast line-by-line k-space sampling assuring a fast acquisition per line.
Further acceleration is achieved via undersampling. The concept describes the acquisition of less k-space lines than demanded by the Shannon-Nyquist-Theorem and naturally translates into shorter acquisition times per image. The drawback, however, is the occurrence of severe undersampling artifacts due to insufficient k-space coverage if traditional image reconstructions are used (Fourier transform). An advanced image reconstruction, on the other hand, presented below and the sophisticated sampling pattern illustrated in Figure 2.3 enable tolerable imaging even with highly undersampled raw data sets.

Figure 2.3 shows the radial sampling pattern for seven successive frames. In contrast to Cartesian sampling the radial imaging inherently oversamples the k-space center where most of the image energy is located and thus provides higher motion robustness and more importantly, benign undersampling behavior [24]. Both features render radial imaging favorable for RT MRI.

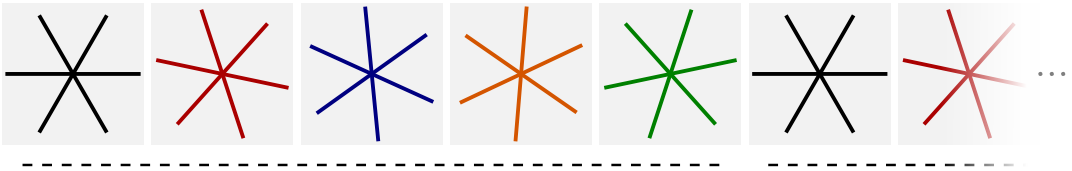

Figure 2.3: Turn-based sampling pattern of undersampled radial FLASH. The k-space trajectories of successive frames show a constant angular displacement and repeat after an odd number of turns.

For each frame an odd number of projections (spokes) is uniformly distributed along 360° and the pattern rotated in the next frames. This way each frame acquires spatial information complementary to the previous which can be exploited during image reconstruction (temporal regularization). After an odd number of turns (usually 5), the sampling pattern repeats. The radial raw data is interpolated onto a Cartesian grid (Gridding) in order to render the Fast Fourier Transform (FFT) algorithm applicable during image reconstruction.
Last but not least, modern MRI machines register the MR signal in multiple receiver coils. This principle of *parallel imaging* describes another important concept of the RT MRI data acquisition. The individual coil elements perceive the MR signal from different perspectives and thus contribute to its spatial allocation. With known coil sensing profiles, parallel imaging supports the image restoration of undersampled data sets [25, 26, 27].

2.3.2 *Reconstruction: Nonlinear Inversion*

To reconstruct raw data subjected to severe undersampling the temporally regularized NLINV [28, 29, 8] algorithm is used. Figure 2.4 demonstrates its performance by comparison to the direct image reconstruction by FFT suffering from severe image artifacts. NLINV, on the other hand, restores images of good quality.

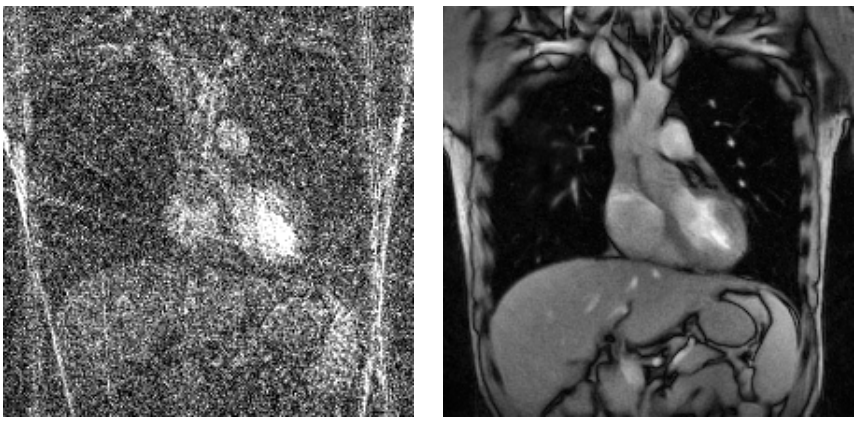

Figure 2.4: FFT reconstruction *(left)* and iterative image reconstruction by temporally regularized NLINV *(right)* of undersampled radial data of the human thorax.

The underlying principle of NLINV describes an iterative and joint estimation of the desired image ρ and the receiver coil sensitivities c_j. The reconstruction is formulated as an optimization problem that describes the MR signal creation in the forward model F:

$$F_j : \mathrm{x} \mapsto \mathrm{y} = P\,\mathcal{F}\left\{\,\rho \cdot c_j\,\right\} \qquad \text{with} \quad \mathrm{x} = \begin{pmatrix} \rho \\ c_1 \\ \vdots \\ c_N \end{pmatrix}$$

Here, $\mathcal{F}$ denotes the Fourier transform, P the sampling operator and x the unknown [7]. The non-linear problem is solved by the Iteratively Regularized Gauss Newton Method (IRGNM) [30] relying on a step-wise linearization $\mathrm{y} \approx DF(\mathrm{x}_n)d\mathrm{x} + F(\mathrm{x}_n)$. Here, $DF(\mathrm{x})$ describes the derivative obtained via Jacobian matrix, x_n an initial guess and y the measured raw data. The linearized problem is then solved for the update $d\mathrm{x}$ to minimize the functional:

$$\underbrace{\|DF(\mathrm{x}_n)d\mathrm{x} - (\mathrm{y} - F(\mathrm{x}_n))\|^2}_{\text{data fidelity}} + \alpha_n \underbrace{\|\mathrm{x}_n + d\mathrm{x}_n - \lambda\,\mathrm{x}_0\|^2}_{\text{regularization}} \tag{2.7}$$

This formulation assures a solution that matches the raw data (data fidelity) and includes prior knowledge on the solution (regularization) in order to stabilize the ill-posed problem. The corresponding update rule for each Gauss-Newton step reads:

$$\mathrm{dx} = \left(DF^H(\mathrm{x}_n)[\mathrm{y} - F(\mathrm{x}_n)] + \alpha_n(\mathrm{x}_n - \lambda\,\mathrm{x}_0)\right)\left(DF^H(\mathrm{x}_n)DF(\mathrm{x}_n) + \alpha_n I\right)^{-1} \tag{2.8}$$

This linear equation is solved by means of the conjugate gradient method. The IRGNM downsizes the regularization strength α_n for each Gauss-Newton step rendering the algorithm robust in the beginning far from the solution and faster in the end close to the solution.
To resolve the ambiguity imposed by the product of ρ and c_j, the NLINV algorithm forces the coil sensing profiles c_j to be spatially smooth. This prior knowledge is incorporated by a preconditioning matrix that transforms all c_j such that the L_2 norm regularization penalizes high spatial frequencies and acts as a Sobolev norm [7].
The reconstruction further benefits from temporal regularization based on the assumption that successive frames of a continuous time series show similar image content (and coil profiles). This additional regularization is included by penalizing the difference of successive frames. For that reason, x_0 in Equation 2.8 refers to the previous frame and the damping factor $\lambda = 0.9$ is introduced to avoid an accumulation of noise.

In a post-processing step a temporal median filter is applied to compensate for remaining radial streaking artifacts. This retrospective filtering is addressed in Chapter 3.2.3 including proposals for improving the application on complex data.

2.4 EXPERIMENTAL EQUIPMENT AND RESOURCES

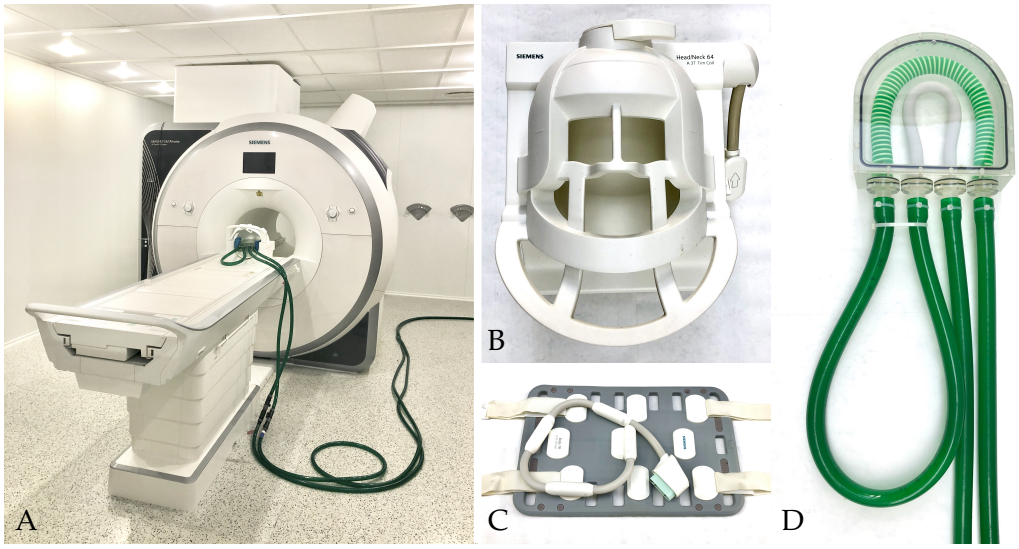

Figure 2.5: A: MRI machine and tubing system for flow phantom, B: head coil, C: thorax coil, D: water-driven flow phantom.

All experiments in this work are performed on a MRI system operating at 3 T *(Magnetom Prisma fit, Siemens Healthcare, Erlangen, Germany)*. Different receiver coil systems are used depending on the human body part (in vivo) or the phantom's size (in vitro). Heart measurements rely on a 18-channel thorax coil (Fig.2.5.C) plus suited elements of the spine coil (integrated into patient table), while head measurements are conducted with a 64-channel head coil (Fig.2.5.B). Flow phantom measurements use a larger 20-channel head coil.
In vitro experiments base on an in-house developed flow phantom (Fig.2.5.D). The phantom consists of two bended plastic tubes with diameter of 1 and 2 cm mimicking the human aortic arch. The setup is water driven by an adjustable pump *(Ocean-Plus, COMET-Pumpen Systemtechnik, Pfaffschwende, Germany)* with flow rates of up to 10 L/min and controlled via digital flow meter. As electrical pump and flow meter are prohibited in the shielded MR scanner room, both components are placed outside and connected to the phantom by tubing of roughly 7 m length as shown in Figure 2.5.
In vivo measurements are performed on young healthy subjects mostly recruited along students of the local university. Written informed consent, according to the recommendations of the local ethics committee, was obtained from all volunteers prior to MRI.
MRI sequence programming is performed within the C++ based Siemens IDEA VD13D sequence development framework. The foundation for this work is given by the 2D radial FLASH sequence used for anatomical RT MRI. Image analysis is performed and reconstruction algorithms prototyped in MATLAB *(Mathworks, Massachusetts, USA)*, while approved reconstruction techniques are implemented on a graphics processing unit (GPU) *(GeForce GTX 580, NVIDIA, Santa Clara, CA)* benefiting from shorter computation times.

3

UNI-DIRECTIONAL PHASE-CONTRAST MRI

The work of this thesis is founded on uni-directional (1d) RT PC flow MRI. The first part of this chapter presents its current state mainly developed by Joseph et al. [9] and Tan et al. [11]. The second part highlights technical developments implemented within the scope of this thesis.

3.1 CURRENT STATE OF REAL-TIME PHASE-CONTRAST MRI

Following to the technical achievements of RT MRI for qualitative anatomical imaging in 2010 [29, 8], Joseph et al. [9, 31] developed a PC MRI technique in 2012 that exploits the benefits gained from RT MRI. Untenberger et al. [10] extended this RT PC method by improving the data acquisition and in 2017 Tan et al. [11] made another significant contribution by formulation of a model-based reconstruction for 1d PC flow data. These steps are briefly described in the following.

3.1.1 *Image Acquisition*

The RT PC data acquisition is based on the radial FLASH sequence as used for anatomical imaging. Two different measurement steps are performed alternately. The first as a phase reference measurement and the second as the actual flow measurement including a bipolar gradient. Figure 3.1 shows the pulse sequence and illustrates the flow encoding in slice-selection direction (z-axis). The result is a flow sensitivity perpendicular to the imaging plane, termed through-plane flow. On the x and y-axis, flow-compensating read gradients are applied that simultaneously null 0^{th}GM and 1^{st}GM.

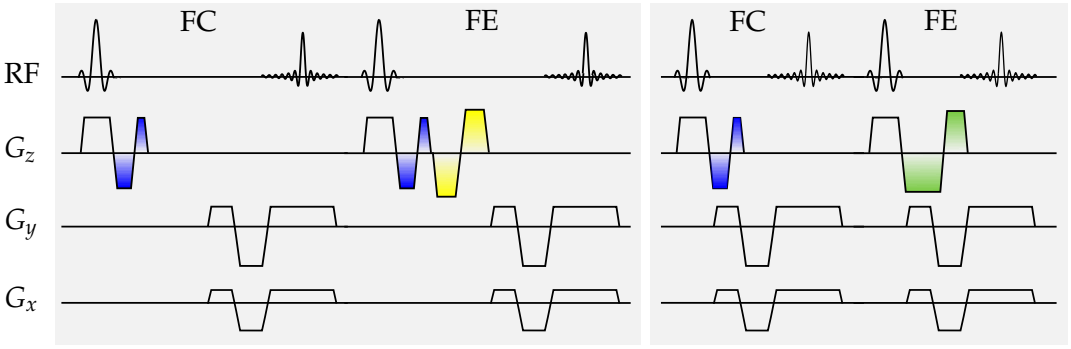

Figure 3.1: Pulse sequence for uni-directional PC MRI. The flow-compensating measurement (FC) is succeeded by a flow-encoding step (FE). *Left:* An independent bipolar gradient *(yellow)* is responsible for flow encoding. *Right:* A fusion *(green)* of flow gradient lobes with flow-compensating gradients *(blue)* accelerates the acquisition.

A fusion of flow-compensating and flow-encoding gradients as described in [32] enables an accelerated sequence and therefore a faster data acquisition in total. The temporal resolution further benefits from the use of an asymmetric echo. Introduced by Untenberger et al. [10] for this specific application, information on one side of the outer k-space is omitted and each spoke is acquired in less time. This gain of temporal resolution is well balanced with the loss of spatial information when using a gradient echo of 20% asymmetry. That corresponds to using 80% of the original spoke's length.
For both measurements the same highly undersampled radial trajectory is used. The acquisition of only few spokes per frame (5 or 7 spokes) achieves short sampling times. That corresponds to severe undersampling (acceleration by a factor of around 50) and the need for an advanced image reconstruction.

3.1.2 *Image Reconstruction*

3.1.2.1 *Phase-Contrast using Non-linear Inversion*

The phase-sensitive NLINV reconstruction yields two complex image time series, ρ_{FC} and ρ_{FE}, reconstructed from the differently encoded FC and FE raw data sets (Fig. 3.1). Both streams are reconstructed independently and quantitative velocity maps are obtained in a post-processing step by a phase difference operation.

$$\Delta\phi = \arg\left(\rho_{\mathrm{FC}} \cdot \rho_{\mathrm{FE}}^{*}\right) = \arg\left(M_{\mathrm{FC}} \cdot M_{\mathrm{FE}} \cdot \exp(i\phi_{\mathrm{FC}} - i\phi_{\mathrm{FE}})\right)$$

In addition, a common magnitude image is obtained by the geometric mean of the two streams M_{FC} and M_{FE}. To alleviate residual streaking artifact, the magnitude image is subjected to a post-processing median filter. The PC map, however, is obtained without temporal filtering to ensure temporal accuracy of the quantitative velocity values.
The overall reconstruction procedure is depicted in Figure 3.2. Note that the temporal regularization only applies for the two individual image time series but not for the velocity map of interest.

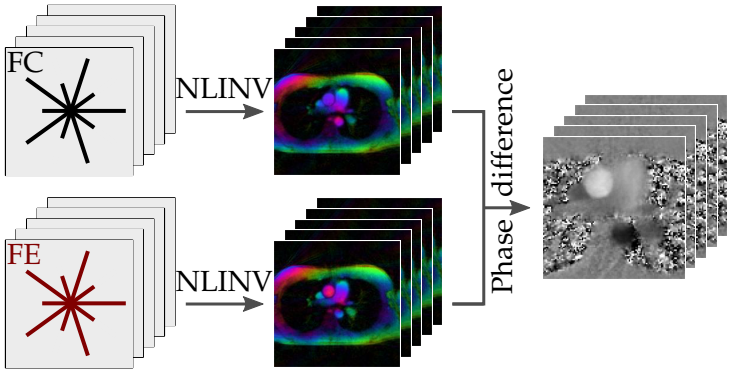

Figure 3.2: Flow chart of NLINV-based PC image reconstruction with differing color-coded phase in the image time series at the human aorta.

3.1.2.2 *Model-based Reconstruction*

The model-based reconstruction (MBR) includes the phase-difference operation by directly estimating the PC map. It can be understood as an extension of NLINV that solves the non-linear inverse problem iteratively by estimating a common image ρ and coil profiles c for both flow-encoded measurements, and the velocity map v in addition. The model assumes the encoding steps to only differ in phase. The forward operator for the j^{th} coil profile and the l^{th} flow-encoding step reads:

$$F_{j,l} : \mathrm{x} \mapsto P_l \, \mathcal{F} \left\{ \rho \cdot \mathrm{e}^{i \cdot S_l \cdot v} \cdot c_j \right\} \qquad \text{with} \quad \mathrm{x} = \begin{pmatrix} \rho \\ v \\ c_1 \\ \vdots \\ c_N \end{pmatrix} \quad \text{and} \quad S_l = [0, 1]$$

Here, v is the desired velocity map, $\mathcal{F}$ the Fourier transform, P_l the projection according to the sampling pattern and S_l the encoding index of the l^{th} flow-encoding step. N indicates the total number of coil elements. While ρ and c_j are complex parameters, v is constrained to be real.
With the introduction of an additional parameter to be estimated, the optimization problem expands. To treat all parameters equally during the iterative optimization and to ensure a reasonable convergence, the derivatives for the respective parameters need to be balanced. This is achieved by internally scaling the velocity map [33]. Figure 3.3 illustrates the procedure of the MBR and thereby points out the conceptional difference towards the NLINV-based PC reconstruction. The results obtained by both methods are compared in Figure 3.4. The underlying data is acquired at the human aorta in a transversal slice orientation with a voxel size of $1.5 \times 1.5 \times 6$ mm^3, 7 spokes and a temporal resolution of 28 fps.

The results of the MBR show significant improvements in image quality over the NLINV approach. The MBR better exploits the redundancy inherent in both encoding steps and allows for the temporal regularization of the desired phase-difference map. As a consequence, the phase noise in signal-weak regions (e.g. lungs) is

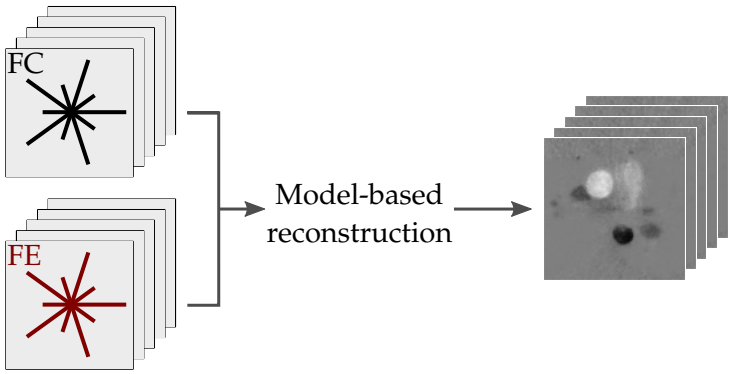

Figure 3.3: Flow chart of model-based PC image reconstruction. In comparison to the NLINV-based approach (Figure 3.2), the velocity map is estimated directly.

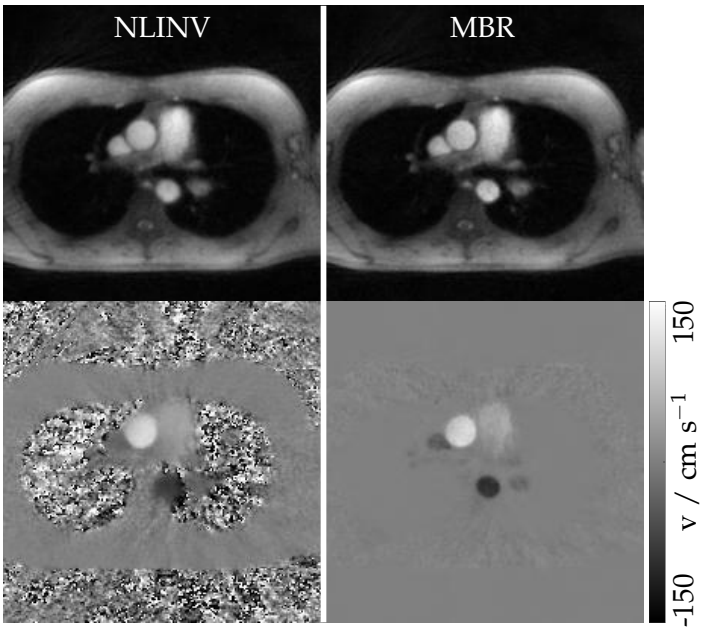

Figure 3.4: Comparison of uni-directional PC MRI obtained by NLINV and MBR. Magnitude images *(top)* are comparable. Judged by the absence of phase noise and an improved spatial acuity, the velocity maps *(bottom)* of the MBR benefit significantly.

completely suppressed. Furthermore, the vessels of interest gain spatially sharper definition. An overall improved spatio-temporal accuracy is achieved, as the MBR allows for even higher degrees of undersampling. While formerly 7 spokes per frame and flow encoding were used [9], the MBR is successfully applied in combination with only 5 radial spokes [11].

3.2 METHODOLOGICAL EXTENSIONS AND TECHNICAL IMPROVEMENTS

While the primary goal of this thesis is the extension to multi-directional RT flow MRI, potential for further improvements of the uni-directional method was found. The resulting technical developments are summarized in the following.

3.2.1 *Relaxation of Flow Encoding Gradients*

In the original implementation [9], flow-encoding gradients are executed as fast as possible, i.e. as fast as the restrictions of a maximum gradient amplitude G and of a tolerable slew rate $\frac{dG}{dt}$ permit. As soon as additional time is available for example due to a longer TE or more time-consuming gradients on other axes, it is advantageous to avoid dead times and to expand the flow gradients in time. This step is not straightforward as the preservation of zeroth and first gradient moments has to be respected by non-linear adaptations of the gradient amplitudes.

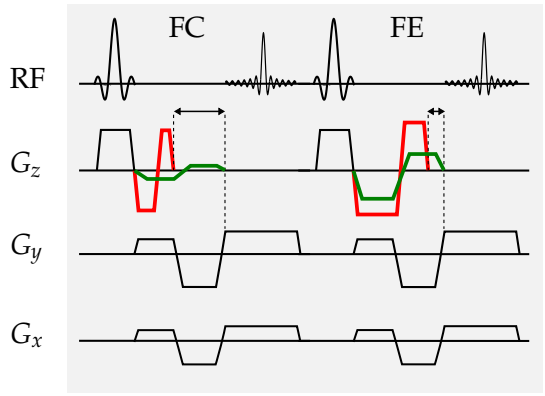

Figure 3.5: Relaxation of flow-encoding gradients. The fastest possible realization *(red)* of flow-compensating or encoding gradients is expanded *(green)*.

A new implementation depicted in Figure 3.5 enables the temporal dilatation by recalculating the amplitudes of the relaxed gradients in a way that both the zeroth gradient moment (responsible for echo formation) and the first gradient moment (flow encoding) are preserved. This way, the occurrence of peripheral nerve stimulation (PNS) in patients is decreased without compromising acquisition time.
PNS arise from inductive currents that are strong enough to cause irritating sensations in the nervous system. By gradient relaxation the time derivative of the magnetic flux density dB/dt is reduced and any PNS accordingly. As a side effect, concomitant field contributions (s. Chap. 6) decrease as well.
The sequence modifications neither affect the image quality nor quantitative flow values which is validated in comparative experiments *(not shown)*.

3.2.2 *Gradient Delay Correction*

Gradient delays summarize time deviations from the nominal gradient waveform due to experimental errors such as eddy currents. As the gradient waveform determines the spatial encoding and sampling trajectories, gradient delays lead to displacements in k-space. These are particularly critical for radial imaging and must be corrected for.
Ideas of Block and Uecker [34] and further adaptations by Untenberger et al. [10] condensed in a gradient delay estimation based on the correlation of approximately opposing spokes. The technique determines the shift in spoke direction as a function of spoke angle [35] and compensates for it in the pre-processing gridding routine.
Even though well accepted and routinely applied for radial RT imaging, the limitations of the correlation-based gradient delay estimation became apparent in the context of this work. Falsely estimated gradient delays were found to be a contributing factor to errors in the velocity maps, since a displacement in k-space is directly reflected as a linear phase shift in the image domain and thus in the PC maps.
Subsequent efforts to also consider oblique slice orientations by means of a rotation matrix could not overcome fundamental problems of the method. These include the demand for a minimum number of spokes to meet the assumption that the spokes are sufficiently opposed. In RT PC MRI, however, the demand for high temporal resolutions and therefore low number of spokes compromises that prerequisite. Moreover, the gradient delay estimation method is weakened by the fact that even perfectly opposing spokes do not guarantee robust gradient delay estimations, as the spokes can be subject to a perpendicular shift that is not registered.
In parallel to the investigations and improvement attempts in this work, Rosenzweig et al. [36] developed an alternative method that estimates the gradient delays for radial imaging more reliably. By determining intersection points of nearly perpendicular spokes, both parallel and perpendicular k-space shifts can be quantified. The method uses the same underlying angular dependency [35] but fundamentally different data correlation that performs more robustly especially for a low number of spokes.
Due to the superiority of this so-called RING method [36], it is integrated into the pre-processing procedure for RT PC MRI. Adaptations for the applicability to PC MRI include the estimation of global delay parameters which are assumed to be constant over different flow encodings and over time. The intersection points are determined for each flow encoding individually using the initial N^{turns} frames of a time series. After that, the data sets are combined to allow for a joint and more reliable data fitting of global delay parameters. This procedure is rendered eligible by experimental investigations as no significant differences were found in joint or individual gradient delay estimations.

3.2.3 *Median Filter*

To compensate for remaining radial streaking artifacts a temporal median filter is applied to the image time series. The time window size of the pixel-by-pixel operating median is given by the number of turns (s. Fig. 2.3) which effectively removes the undesired streaking artifacts in a post-processing step.
In standard anatomical imaging only the magnitude image is of interest and the complex nature of the MRI signal neglected. Consequently, the current median filter was implemented to only focus on magnitude images and to disregard the effect on corresponding phase values. Using further post-processing filters [37], however, which operate on complex data, the phase information becomes relevant.
Investigations performed in the scope of this work revealed that the median filter by current status introduces phase inconsistencies and artifactual complex images as pointed out in Figure 3.6. Especially areas of fast intensity changes (lips and tongue in speech MRI) are affected in phase, real- and imaginary part. Even though the desired magnitude images are not corrupted directly, the artifacts in real- and imaginary part can translate into the magnitude image by the denoising via non-local means [37] operating on complex images.

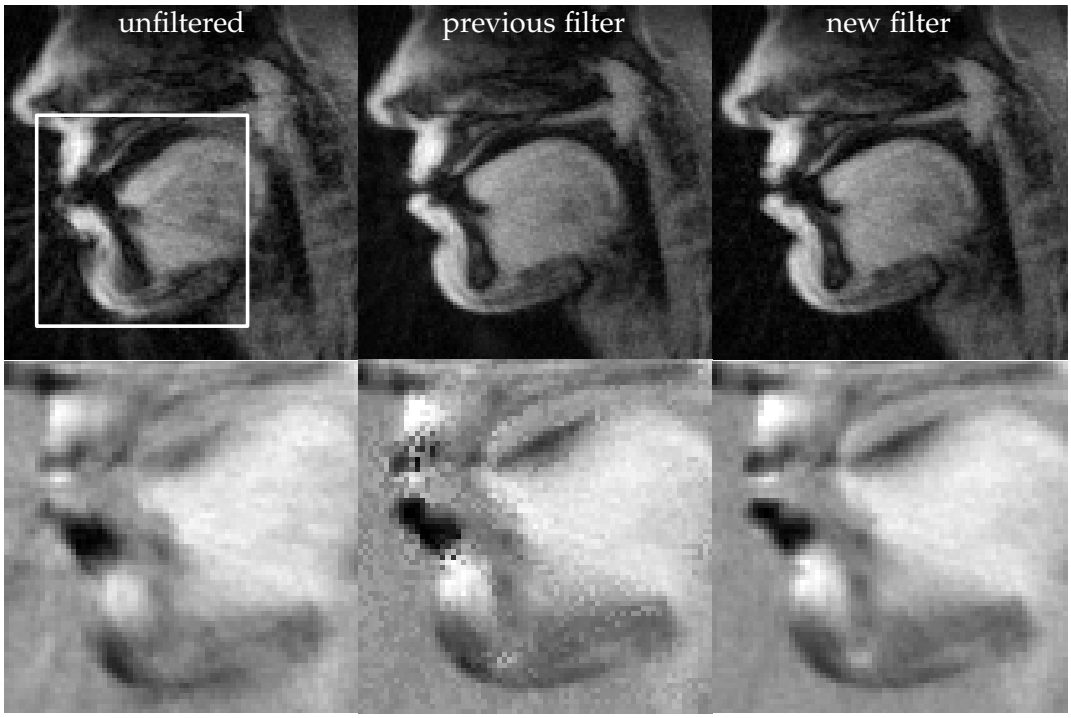

Figure 3.6: Performance of new median filter. Magnitude images *(top)* and real part *(bottom)* of RT speech MRI. While the previous implementation results in phase inconsistencies, the latter are avoided using two temporal median filters on real and imaginary part individually.

To avoid the undesired artifact creation, this work proposes to apply two individual median filters on real and imaginary part. Investigations using numerical simulations and various experimental data sets render the proposed technique superior to

the previous implementation and to a vector median [38] judged by the complete suppression of the previously occurring artifacts.
The new filter treats real and imaginary part independently which better reflects the underlying characteristics of uncorrelated noise in both receiving channels and thus allows a reliable performance on complex data.

3.2.4 *Reduction of Acquisition Time*

PC MRI offers different ways of realization. In each measurement step, the 1^{st}GM determines the type and strength of the velocity encoding. In the classic one-sided encoding technique, the initial 1^{st}GM is zero (flow-compensating reference measurement) whereas the following step provides the full 1^{st}GM defined by the VENC (Equation 2.6).
As the velocity is obtained by a difference operation, it is possible to distribute the flow encoding between the two steps. The so-called balanced approach exhibits halved 1^{st}GMs of opposite sign and offers various advantages, that are more detailed discussed regarding multi-directional flow in Chapter 4.
For uni-directional flow with merged imaging and flow gradients, another option exists that aims at minimal acquisition time. Instead of specifying individual 1^{st}GMs, only the difference has to be fixed (as determined by the VENC). The resulting degree of freedom allows to optimize the gradient waveforms for a given slice selection gradient that imposes an own 1^{st}GM that has to be compensated for. By means of this gradient design optimized regarding execution time, a minimum TE is achieved [32]. Figure 3.7 illustrates the different sequences for uni-directional through-plane flow.

Figure 3.7: Sequence designs for uni-directional through-plane flow. The specified difference in 1^{st}GM can be realized by different individual values. By choosing α such that the last gradient lobe *(green)* is mirrored the minTE approach guarantees the fastest execution for a given slice selection gradient.

In this thesis, the minimal TE velocity encoding (minTE) by Bernstein et al. [32] is implemented for radial RT PC MRI and validated using in vitro and in vivo measurements. The method's potential regarding short TE is investigated under different imaging scenarios representative for RT 1d PC flow applications.

While the improvement in the high-VENC regime (200 cm/s) for aortic flow is modest (4% speed up), significant potential is found for small values (10 cm/s) as applied for measurements of cerebrospinal fluid (CSF) flow. In this case, an acceleration of around 30% is achieved. Due to its reciprocal relation, small VENC values rely on large gradient moments that are more efficiently applied by minTE than by one-sided velocity encoding. Figure 3.8 shows a comparison of CSF results obtained by both methods and their optimized protocols. The benefit of minTE was invested either in four more spokes or two more spokes in combination with higher spatial resolution. The temporal resolution in these examples is kept constant at 125 ms (8 fps).

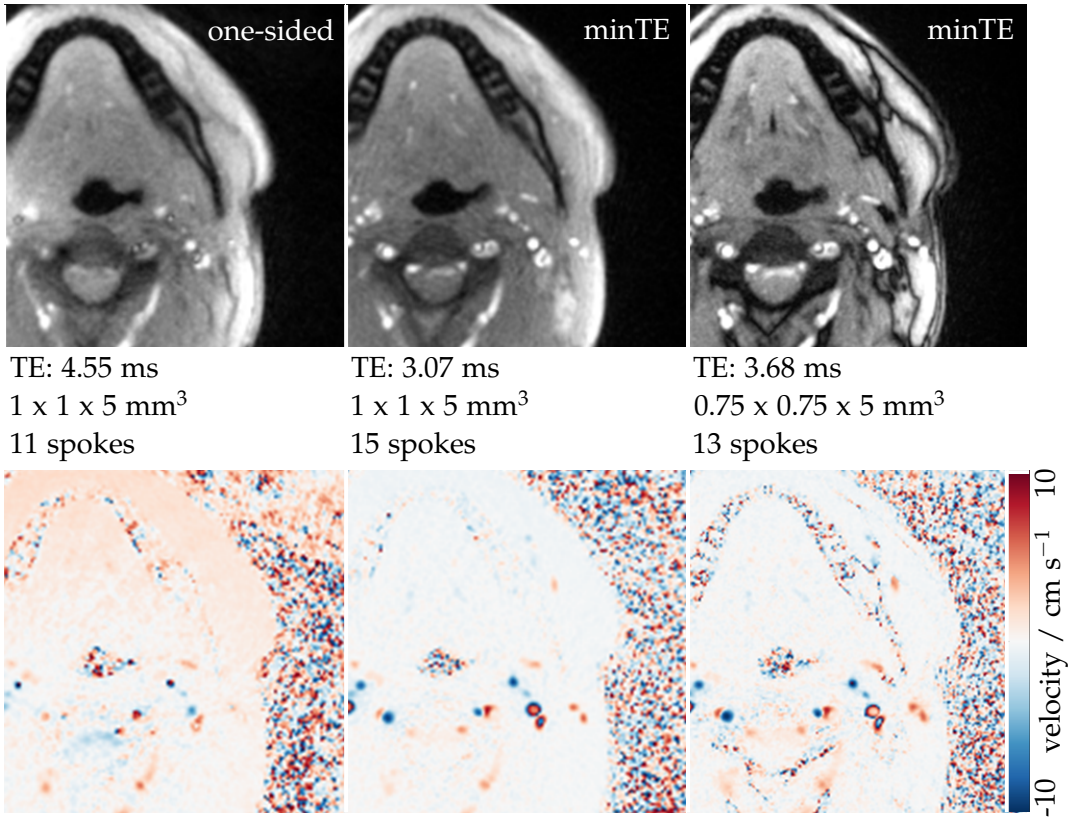

Figure 3.8: Sequence and protocol comparison for CSF measurements. Magnitude *(top)* and PC maps *(bottom)* of a transversal cross-section at C3 level. The introduction of minTE flow encoding improves the spatio-temporal resolution significantly. At the same time the accuracy benefits. The formerly used one-sided approach *(left)* exhibits a long TE and phase offset errors in static tissue *(redish jar area)*.

In addition to improved spatial information, the accuracy of the velocity quantification benefits under minTE acquisitions. Phase offset errors in static tissue are more pronounced using the one-sided velocity encoding and most likely arise due to concomitant field contributions - a topic addressed more detailed in Chapter 6. In short, all imaging and flow gradients imprint an additional phase that cancels out in PC maps if both encoding steps would exhibit the same gradient waveform. As the minTE gradients are designed more similarly than the asymmetric gradient design of the one-sided method, the latter exhibits larger phase errors in quantitative

PC maps. These errors are evident in Figure 3.8.
While previous RT PC studies [39, 40] on CSF flow dynamics applied the one-sided acquisition scheme, novel and ongoing studies rely on the new minTE implementation. The results published in Aktas et al. [41] gained from improved spatial definition and higher accuracy as described above. CSF dynamics as one of the application fields of RT PC MRI is addressed in Chapter 7.

In conclusion, the minTE velocity encoding contributes significantly to improve 1d RT PC MRI. Not only in the demonstrated low-flow regime but also for higher velocities minTE generally is the favorable choice as the approach guarantees the shortest TE - a parameter of high relevance in RT imaging aiming at fast acquisition times.

4

DEVELOPMENT OF MULTI-DIRECTIONAL PHASE-CONTRAST MRI

This chapter describes the methodological development of multi-directional RT PC MRI. The chapter divides into an acquisition and image reconstruction part, followed by results and alternative visualization techniques. While this chapter lays the foundation for multi-directional velocimetry, Chapter 5 presents further methodological improvements and concludes with a summary over both chapters. Final results and application examples of the novel imaging technique are presented in Chapter 7. Parts of this chapter have been published in *NMR in Biomedicine* [42].

4.1 IMAGE ACQUISITION

The pulse sequence and more particularly the gradient design represents a descriptive and one of the most informative parts of the image acquisition. The modifications performed to obtain multi-directional flow sensitivity are described in detail, followed by different velocity encoding strategies and notes on the k-space trajectory and acquisition order.

4.1.1 *Pulse Sequence Design*

The pulse sequence for multi-directional PC MRI is based on the radial FLASH sequence as used for RT anatomical imaging (s. Chap. 2 and 3). Flow sensitivity is integrated by a bipolar gradient. Its orientation defines the direction in which the velocity is to be quantified. In Chapter 3, this direction is limited to the velocity component perpendicular to the imaging slice (through-plane flow). In this chapter, in-plane flow is realized by placing bipolar gradients on one or both read axes.
The execution of additional bipolar gradients comes at the expense of an increased TE. In PC MRI, however, TE is a crucial parameter that is generally desired to be short. The reasons for that include i) the prerequisite for short TR and thus high temporal resolution, ii) the support of assuming constant velocities during echo formation, and iii) the prevention of dephasing effects.
This work presents different concepts of flow gradient design aiming at a TE reduction and thus an acceleration of the PC sequence with in-plane flow sensitivity. The individual steps described in the following and illustrated in Figure 4.1 were implemented sequentially and their performance investigated experimentally.

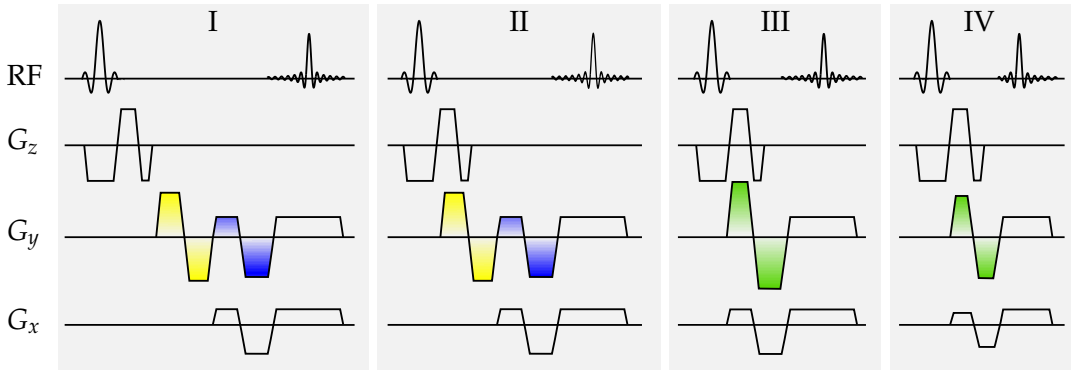

Figure 4.1: Sequence optimization for in-plane PC. The timing gradually reduces from I to IV. I: Independent flow-encoding *(yellow)* and compensating gradients *(blue)*, II: overlapping gradients, III: merged flow gradients *(green)*, and IV: asymmetric echo.

- Overlapping Gradients: Gradient lobes that imprint phases on different axes can be played out simultaneously. In fact, only the slice selection gradient during RF excitation and the read gradient during signal readout must be executed isolatedly, i.e. without any gradients on other axes. Flow-encoding gradients on the read axis may overlap with flow-compensating gradients on the slice axis. As a consequence, the pulse sequence can be squeezed in time (I $\rightarrow$ II).

- Fusion of Flow Gradients: Flow-encoding and imaging gradients can be combined. Following ideas introduced by Bernstein et al. [32] the flow-encoding and flow-compensating gradient lobes can be merged into more time-efficient gradient lobes (II $\rightarrow$ III). While originally introduced for Cartesian sampling with a constant read gradient G_R, read gradients rotate during radial sampling as a function of the projection angle φ. That principally complicates a gradient fusion as the rotation of G_R has to be taken into account, lest the flow-encoding direction would rotate as well. The respective technique, developed here, has been published in [42]. Starting with the optimized gradient waveform for a Cartesian readout with in-plane flow sensitivity in x-direction, the gradient amplitudes for radial sampling are modulated as follows:

$$G_R^x(\varphi) = G_R \cos(\varphi) \tag{4.1}$$

$$G_I^x(\varphi) = G_I \cos(\varphi) - 2M_V \frac{1-\cos(\varphi)}{(w_O + w_I)(w_I - r)} \tag{4.2}$$

$$G_O^x(\varphi) = G_O \cos(\varphi) + 2M_V \frac{1-\cos(\varphi)}{(w_O + w_I)(w_O - r)} \tag{4.3}$$

Here, r and w denote the minimal gradient ramp time and the duration of inner (I) and outer (O) gradient lobe, respectively. A derivation is given in Chapter A.1 in the appendix. The method enables the readout gradient strength to be modulated by the projection angle as necessary for radial

sampling, while the first gradient moment M_V responsible for flow encoding remains constant in x-direction. In other words, the technique calculates the minimal TE neccessary to achieve *radial* imaging yet *cartesian* flow quantification.

- ASYMMETRIC ECHO: Asymmetric echoes shorten read gradients and in-plane flow-encoding gradients. Using an asymmetric echo as described in [10] less sampling points are acquired in k-space and read gradients are shortened accordingly. That results in smaller zeroth and first gradient moments which have to be compensated for. As a consequence also flow-compensating and merged flow-encoding gradients are potentially shorter. All in all, shorter TE are achieved at the tolerable expense of less information in outer k-space (III $\rightarrow$ IV).

Each intermediate step was validated experimentally using the established through-plane flow technique [9, 10] as ground truth. The experiments relied on the flow phantom operated at constant flow of 5 $^{l}/_{\text{min}}$. Uni-directional in-plane velocity was acquired with independent (I), overlapping (II), and merged gradients (III), plus merged gradients and asymmetric echo of 20% (IV) (compare to I-IV in Fig. 4.1). A field of view (FOV) of 192×192 cm^2 was used with 1.5×1.5 mm^2 in-plane resolution and 6 mm slice thickness. The VENC was set to 200 cm/s and 7 spokes are acquired per flow encoding and frame. With TR of 5.36, 4.02, 3.25, and 2.93 ms the temporal resolution improved from 13 up to 24 frames per second (fps). Image reconstruction is performed using NLINV.

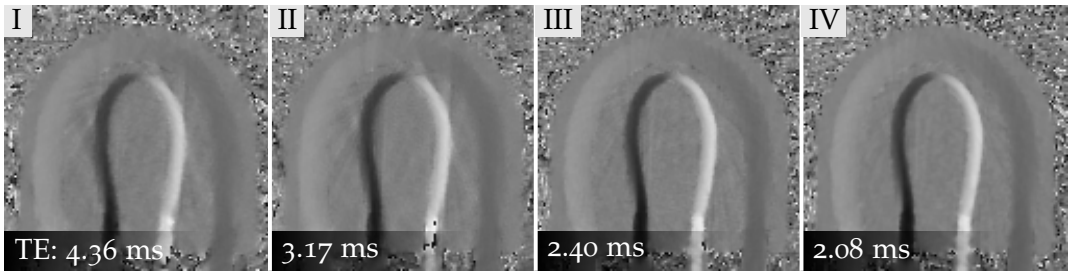

Figure 4.2: Experimental results of TE reduction for in-plane PC using the flow phantom (Fig. 2.5.D). I - IV as in Fig. 4.1. While all methods agree in terms of quantitative values, the fastest version achieves the best image quality judged by the least amount of artifacts and highest image sharpness.

Figure 4.2 summarizes the results and demonstrates an agreement of all methods in terms of velocity values. The individual protocols differ significantly in minimum execution time. For the given example, TE was more than halved by the optimization steps, which constitutes a substantial acceleration. Remarkably, throughout the tested parameter range the best image quality was achieved with the fastest acquisition judging from the higher image sharpness and less image artifacts for the fastest pulse sequence. This finding can be ascribed to the fact that shorter TE reduce the influence of intra-voxel dephasing and the amount of T_2 decay which translates into higher SNR.

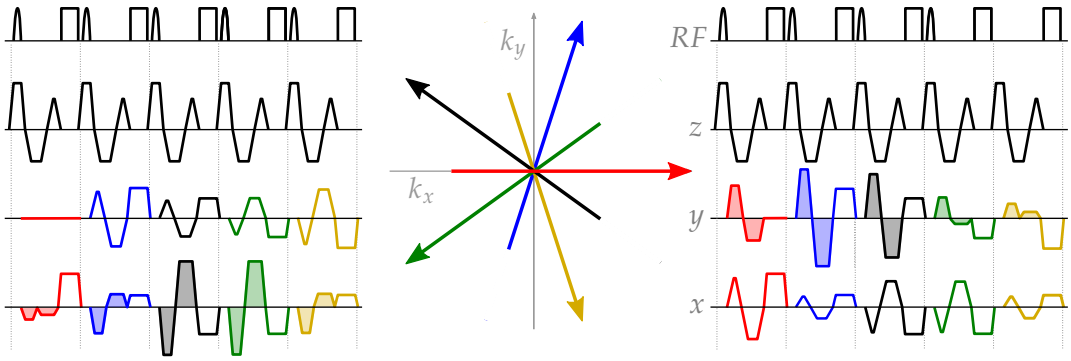

Figure 4.3: Schematic pulse sequence for in-plane PC based on radial FLASH with flow sensitivity in x-direction *(left)* and in y-direction *(right)*. The flow-compensated reference step is not shown. Flow encoding is included in the shaded gradient lobes. Individual colors indicate different radial spokes in k-space *(center)*.

Based on the optimized gradient design, full two-directional in-plane flow sensitivity is achieved by encoding the velocity in x and y-direction sequentially. Here, the gradient projection rules (Eq. 4.1 to 4.3) apply to y with $\cos(\varphi)$ replaced by $\sin(\varphi)$. Figure 4.3 illustrates the pulse sequence design for both perpendicular in-plane velocity components with corresponding spokes in k-space. Full flow compensation is applied on all (non-flow-encoding) axes.
The presented pulse sequence benefits from all gradient design concepts listed above and thereby lays the foundations for multi-directional RT PC flow MRI.

4.1.2 *Velocity Encoding Strategies*

This subchapter builds on the flow-sensitive radial FLASH sequence described above and presents different velocity encoding schemes for the realization of uni- and multi-direcitonal flow.

Uni-directional PC flow consists of two flow-encoding steps. The standard approach, the so-called *one-sided* method, includes a flow-compensating reference scan (1^{st}GM = 0) and a flow-encoding step with the 1^{st}GM defined by the VENC. Therefore, the velocity of interest v is measured only in the second encoding, while both encodings share the phase reference Φ_0. This encoding is represented in matrix notation in Equation 4.4.
Multi-directional velocity encoding, i.e. 2d and 3d flow, in the one-sided approach is achieved by adding one or two respective encoding steps as described by Equation 4.5 and 4.6. All velocity measurements share a common phase reference scan. The order of encodings steps can principally be changed and also any combination of different velocity components is possible. In the following, the term 2d flow refers to the measurement of both in-plane flow components and 3d flow describes the addition of through-plane flow (v_z).

$$os1\text{d}: \quad \begin{pmatrix} e_1 \\ e_2 \end{pmatrix} = \begin{pmatrix} 1 & 0 \\ 1 & 1 \end{pmatrix} \begin{pmatrix} \Phi_0 \\ v \end{pmatrix} \tag{4.4}$$

$$os2\text{d}: \quad \begin{pmatrix} e_1 \\ e_2 \\ e_3 \end{pmatrix} = \begin{pmatrix} 1 & 0 & 0 \\ 1 & 1 & 0 \\ 1 & 0 & 1 \end{pmatrix} \begin{pmatrix} \Phi_0 \\ v_x \\ v_y \end{pmatrix} \tag{4.5}$$

$$os3\text{d}: \quad \begin{pmatrix} e_1 \\ e_2 \\ e_3 \\ e_4 \end{pmatrix} = \begin{pmatrix} 1 & 0 & 0 & 0 \\ 1 & 1 & 0 & 0 \\ 1 & 0 & 1 & 0 \\ 1 & 0 & 0 & 1 \end{pmatrix} \begin{pmatrix} \Phi_0 \\ v_x \\ v_y \\ v_z \end{pmatrix} \tag{4.6}$$

As the flow-compensated scan (e_1) is free of velocity information, only half ($os1\text{d}$) or even one fourth ($os3\text{d}$) of the time is invested to measure each velocity component. On the one hand, that fact leads to a sharp temporal footprint (time window of flow data acquisition), on the other hand, it renders the one-sided velocity encoding ineffective in comparison to the following alternative.
The *balanced* flow encoding method is free of flow-compensated zero-measurements. Instead, each velocity component is encoded in every step and therefore measured multiple times. Equations 4.7 - 4.9 specify the encoding matrices for balanced 1d, 2d and 3d flow.

$$bal1\text{d}: \quad \begin{pmatrix} e_1 \\ e_2 \end{pmatrix} = \frac{1}{2} \begin{pmatrix} 1 & -1 \\ 1 & 1 \end{pmatrix} \begin{pmatrix} \Phi_0 \\ v \end{pmatrix} \tag{4.7}$$

$$bal2\text{d}: \quad \begin{pmatrix} e_1 \\ e_2 \\ e_3 \end{pmatrix} = \frac{1}{2} \begin{pmatrix} 1 & -1 & 1 \\ 1 & 1 & 1 \\ 1 & 1 & -1 \end{pmatrix} \begin{pmatrix} \Phi_0 \\ v_x \\ v_y \end{pmatrix} \tag{4.8}$$

$$bal3\text{d}: \quad \begin{pmatrix} e_1 \\ e_2 \\ e_3 \\ e_4 \end{pmatrix} = \frac{1}{2} \begin{pmatrix} 1 & 1 & 1 & 1 \\ 1 & 1 & -1 & -1 \\ 1 & -1 & 1 & -1 \\ 1 & -1 & -1 & 1 \end{pmatrix} \begin{pmatrix} \Phi_0 \\ v_x \\ v_y \\ v_z \end{pmatrix} \tag{4.9}$$

The $bal1\text{d}$ and $bal3\text{d}$ encoding schemes are well-known in the literature [43, 44] and relate to the Hadamard transform [45]. For this reason also the name *Hadamard encoding* is commonly used for balanced 3d flow.

For 2d flow, with its three encoding steps, a Hadamard transformation is not defined, as the latter requires a power of two (2^n) in matrix size. The encoding proposed here is a compromise that only meets the most important criteria for balanced velocity encoding. It exhibits an equal distribution of velocity encoding and a constant absolute 1^{st}GM in all encoding steps. Unlike *bal*1d and *bal*3d the vector sum of all 1^{st}GMs for *bal*2d does not sum up to zero which is observed to be disadvantageous for a model-based image reconstruction *(s. Chap. 4.3.1)*. The alternative of a uniform distribution of 1^{st}GM vectors in triangular shape (120° angular displacement) would sum up to zero but would not meet the prerequisite of a constant absolute 1^{st}GM for each velocity component individually, wherefore the *bal*2d approach as given in Equation 4.8 is preferred.
Figure 4.4 illustrates the one-sided and balanced methods for 1d, 2d and 3d flow. The individual 1^{st}GMs responsible for flow encoding are represented as bold vectors. The flow-compensation scans are displayed as black dots (vectors of length zero).

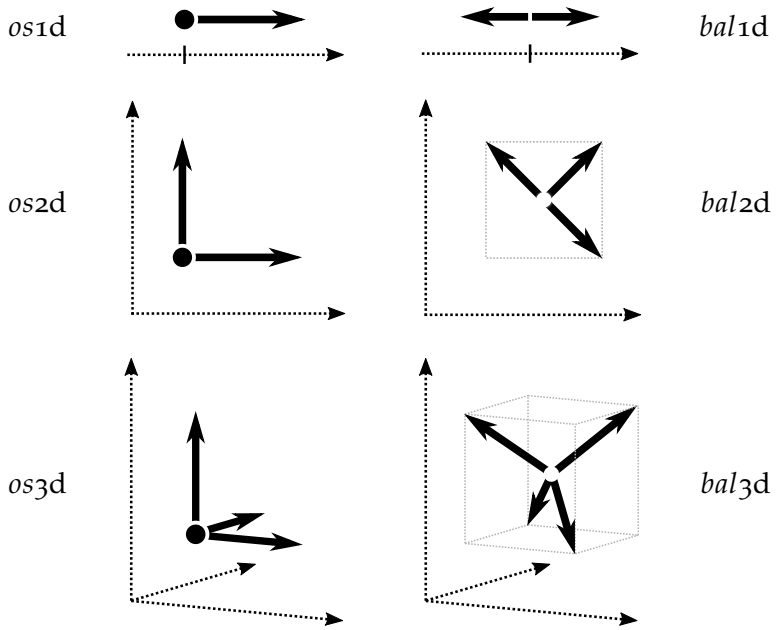

Figure 4.4: Velocity encoding strategies for 1d, 2d and 3d flow. One-sided acquisition schemes with flow compensating reference measurement *(left)* and balanced acquisition schemes *(right)*. The bold vectors represent the first gradient moments responsible for velocity encoding.

In comparison, the balanced methods exhibit overall smaller first gradient moments than the one-sided methods to cover a comparable dynamic velocity range. This goes along with a potentially faster execution of respective gradient lobes and thus shorter TE. Furthermore, the balanced approach benefits from constant absolute 1^{st}GMs (constant vector length in Fig.4.4) and thus constant degrees of intra-voxel phase dispersion. As the flow-induced phase dispersion reduces the MR signal strength, the magnitude images of the individual flow encodings are expected to be more similar for the balanced method which matches the assumptions of the model-based image reconstruction (shared ρ).

For each flow direction the VENC can be set independently of the other directions, whereby the lowest value (longest TE) predicts the sequence timing (constant TR). For that reason this work only covers isotropic velocity encoding.
More advanced encoding strategies are conceivable which aim at higher dynamic ranges or higher VNR [46, 47, 48]. On the downside, these methods come at the expense of additional encoding steps and thus lower temporal resolution. For that reason, this work focuses on the velocity encoding strategies listed above exhibiting the minimum number of encoding steps (= number of velocity components plus one) and thus the potentially shortest acquisition times.

4.1.3 *k-Space Trajectory*

Another important aspect of the data acquisition is the choice of k-space trajectory. Based on the turn-based radial sampling pattern used for anatomical RT imaging (Fig. 2.3) the same sets of spokes are used for all flow-encoding measurements. Uni-directional RT PC MRI as described in Chapter 3 has exclusively been performed using this trajectory, denoted as SAMESPOKES, and multi-directional velocity encoding in this chapter adapts this basic trajectory for multiple encodings.
Alternative radial trajectories that better exploit the redundancy of different flow-encoding measurements by using complementary k-space information are addressed at a later stage in Chapter 5.2.

4.1.4 *Acquisition Order*

The data acquisition can be performed either *sequentially* (acquisition of all spokes $s_1 - s_N$ of e_1 before switching to e_2) or spoke *interleaved* (first spoke s_1 of e_1 followed by s_1 of e_2). All pulse sequences are implemented in a way that both options are available to the operator of the MRI scanner.
Even though the choice is expected to have no effect on the nominal temporal resolution, this work recommends to use a sequential acquisition scheme for the one-sided method. The other way around would take away the advantage of a sharp temporal footprint. For the balanced strategy, the interleaved option is preferred as it best supports the balanced nature of the approach and shows a higher motion robustness in combination with the MBR.

4.2 IMAGE RECONSTRUCTION

This chapter covers the transformation of raw data into image time series of multi-directional velocity maps. The first part addresses the applicability of the image reconstruction techniques of uni-directional PC MRI (Chap. 3) and in the second part an extension of the MBR to multiple flow directions is proposed that estimates velocity vectors.

4.2.1 *NLINV-based and 1d Model-based Reconstruction*

The NLINV-based approach relies on individual reconstructions of the two, three or four differently encoded data streams. PC velocity maps are obtained in a post-processing step by inversion of the respective encoding matrix S. The inverse S^{-1} is applied to the phase of all encoding steps to compute the velocity-vector components. A common magnitude image is generated by averaging. Lacking a direct regularization of the velocity maps, however, the NLINV approach is inferior to the MBR (see Chapter 3.1.2).
The MBR developed by Tan et al. [11] is designed for uni-directional flow and therefore limited to phase difference estimations between two encoding steps. For more flow encodings, the MBR is performed multiple times in sequential executions.
The choice of which encoding steps build a pair for the phase difference estimation is straightforward for the one-sided velocity encoding as the PC difference always relates to the flow-compensating phase reference acquisition. Here, the 1d reconstructions of multi-directional acquisitions benefit from temporal interpolation of the phase reference data as published in [42].
For balanced velocity encoding, however, the choice of flow encodings is ambiguous and the applicability of the model-based reconstruction for uni-directional flow (1dMBR) hindered. On top of that, the execution of multiple 1dMBRs is highly redundant as it is based on repeated estimations of the same image content ρ and same coil profiles c_j.

4.2.2 *Model-based Reconstruction for Multi-directional Flow*

This work takes up on the idea of a direct velocity estimation (and regularization) [11] and formulates a model-based reconstruction for multi-directional flow (mdMBR). Instead of estimating only one velocity map v, the extension of the 1dMBR implies the estimation of multiple velocity maps $v_{1...D}$ (one for each velocity component) simultaneous to the reconstruction of image content ρ and the coil sensitivity maps c_j. The new forward model F for the j^{th} coil and the l^{th} flow encoding reads:

$$F_{j,l} : \mathrm{x} \mapsto P_l \, \mathcal{F} \left\{ \rho \cdot \exp\left(i \sum_{d=1}^{D} S_{d,l} \cdot v_d \right) \cdot c_j \right\} \qquad \text{with} \quad \mathrm{x} = \begin{pmatrix} \rho \\ v_1 \\ \vdots \\ v_D \\ c_1 \\ \vdots \\ c_N \end{pmatrix} \tag{4.10}$$

Here, D denotes the number of velocity components, making the number of required encoding steps to be $D+1$. P_l and $\mathcal{F}$ describe the sampling pattern and the discrete Fourier transform, respectively.
While flow encoding is represented by a scalar parameter S in 1dMBR, the indices $S_{d,l}$ now form a $D \times D+1$ matrix to indicate flow-compensating or flow-encoding measurements for each velocity component individually. These encoding matrices refer to either one-sided or balanced encoding (Eq. 4.4 to 4.9), or any other velocity encoding desired.
Just as temporally regularized NLINV [8] and the 1dMBR [11], the mdMBR is formulated as an optimization problem that is solved by the IRGNM relying on a stepwise linearization. The Frechét derivative of the forward operator $DF(\mathrm{x})$ used in each linear substep for the j^{th} coil element and the l^{th} encoding is calculated by applying the Jacobian matrix to F:

$$\begin{aligned} DF_{j,l}(\mathrm{x}) \begin{pmatrix} \mathrm{d}\rho \\ \mathrm{d}v_1 \\ \vdots \\ \mathrm{d}v_D \\ \mathrm{d}c_1 \\ \vdots \\ \mathrm{d}c_N \end{pmatrix} &= P_l \, \mathcal{F} \left\{ \exp\left(i \sum_{d=1}^{D} S_{d,l} v_d \right) \left[c_j \, \mathrm{d}\rho + \rho \, \mathrm{d}c_j + \sum_{d=1}^{D} \rho \, c_j \, i \, S_{d,l} \, \mathrm{d}v_d \right] \right\} \\ &= \mathrm{dy}_{j,l} \end{aligned}$$

The operator $DF(\mathrm{x})$ maps the deviation of the unknowns dx to the deviation in gridded raw data $\mathrm{dy}_{j,l}$. The adjoint operator $DF^H(\mathrm{x})$ operates in the opposite direction and maps dy to dx as follows:

$$DF^H(\mathrm{x}) \begin{pmatrix} \mathrm{dy}_{1,1} \\ \vdots \\ \mathrm{dy}_{N,1} \\ \\ \vdots \\ \\ \mathrm{dy}_{1,D+1} \\ \vdots \\ \mathrm{dy}_{N,D+1} \end{pmatrix} = \begin{pmatrix} \sum_{j=1}^{N} c_j^* \left[\sum_{l=1}^{D+1} \mathrm{e}^{-i \sum_{d=1}^{D} v_d \cdot S_{d,l}} \cdot \mathcal{F}^{-1} \{ P_l^H \mathrm{dy}_{j,l} \} \right] \\ \\ \Re \left(\sum_{j=1}^{N} \rho^* c_j^* \left[\sum_{l=1}^{D+1} i \, S_{1,l} \, \mathrm{e}^{-i \sum_{d=1}^{D} v_d S_{d,l}} \mathcal{F}^{-1} \{ P_l^H \mathrm{dy}_{j,l} \} \right] \right) \\ \vdots \\ \Re \left(\sum_{j=1}^{N} \rho^* c_j^* \left[\sum_{l=1}^{D+1} i \, S_{D,l} \, \mathrm{e}^{-i \sum_{d=1}^{D} v_d S_{d,l}} \mathcal{F}^{-1} \{ P_l^H \mathrm{dy}_{j,l} \} \right] \right) \\ \\ \sum_{l=1}^{D+1} \rho^* \mathrm{e}^{-i \sum_{d=1}^{D} v_d \cdot S_{d,l}} \cdot \mathcal{F}^{-1} \{ P_l^H \mathrm{dy}_{1,l} \} \\ \vdots \\ \sum_{l=1}^{D+1} \rho^* \mathrm{e}^{-i \sum_{d=1}^{D} v_d \cdot S_{d,l}} \cdot \mathcal{F}^{-1} \{ P_l^H \mathrm{dy}_{N,l} \} \end{pmatrix}$$

Here, * denotes the point-wise complex conjugation and $\Re$ constraints the velocity maps to be real-valued, such that the flow-encoding steps only differ in phase.
The IRGNM is initialized with $\mathrm{x}_0 = (\rho = 1, v_i = 0, c_j = 0)$ and iteratively updates x in a sequence of regularized linearizations of the signal model. Here, the same update rule as used for the temporally regularized NLINV algorithm applies (Equation 2.7 and 2.8).
To balance the derivates of the unkowns, $\mathrm{d}\rho$ and $\mathrm{d}v_i$, the automatic scaling approach [33] from the 1dMBR is exploited and each velocity component scaled individually during reconstruction. The mdMBR algorithm is implemented on a single GPU and all image reconstructions at this stage are performed offline, i.e. after data acquisitions.

4.3 RESULTS

4.3.1 *Numerical Phantom*

The mdMBR was validated using a numerical phantom which generates simulated raw data. Here, the reference values are known precisely and experimental errors, such as eddy currents or field inhomogeneities, are ruled out. A very basic phantom was designed consisting of three different circles, each representing one of the 3d velocity components. The phantom's phase reference is homogeneous at 0° and all velocity values set at 100°. By means of the analytical Fourier transform highly undersampled radial raw data sets were generated with 5 spokes per flow encoding and frame. The mdMBR was compared to the 1dMBR and both, the one-sided and balanced flow encoding, were tested.

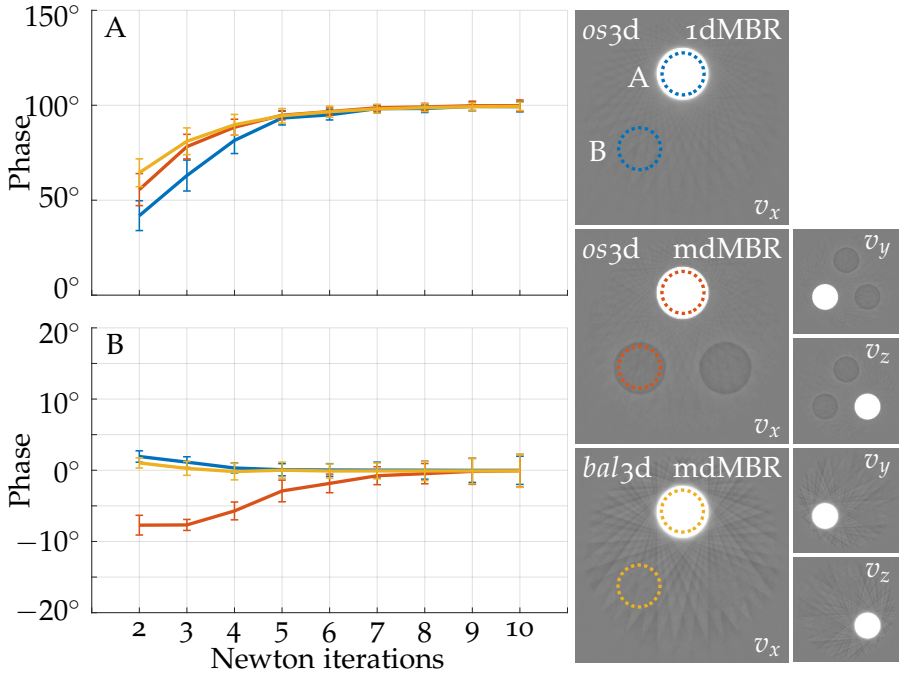

Figure 4.5: Convergence of 1d and 3d model-based reconstructions for numerical flow phantom. The ROI evaluations reveal that all methods approach the reference values of 100° and 0°. The fastest convergence is obtained for the balanced velocity encoding method. Velocity maps obtained after 6 Newton iterations are shown on the right. Note that the 1dMBR yields only one velocity component, while the mdMBR approach estimates velocity vectors.

Figure 4.5 shows the convergence of the iterative image reconstruction variants. The ROI evaluation in one selected velocity map reveals that all methods converge to the reference values. This implies a correct implementation and satisfying performance of the new reconstruction technique.
Nevertheless, differences in the convergence behavior are observed. For low numbers of Newton steps the simultaneous estimation of multiple velocity maps of the *os*3d flow data set deviates from the other methods. Negative velocity values are observed in regions where the ground truth predicts velocities of zero and non-zero

velocity components in other directions. This effect is apparent in dark circles in the *os*3d-velocity map in Figure 4.5. As a consequence, for *os*3d a higher number of Newton iterations is required.
The balanced approach (*bal*3d) is observed to be beneficial for the optimization process. The velocity maps are estimated more accurately, i.e. without any "cross-talk" between different velocity components (no dark circles in Fig. 4.5). Nevertheless, for this method the amount of radial streaking artifacts is slightly increased. For quantitative imaging, however, accurate measurements are more crucial, wherefore the balanced encoding technique is preferable over the one-sided encoding method.

The reason for the different convergence behaviors is found in different estimates of the image content ρ. Its phase values which physically describe the phase reference Φ_0 are not equally well reconstructed. Figure 4.6 shows the phase maps for the numerical phantom and points out that only the balanced approach is in accordance with the ground truth as it delivers a homogenous phase reference map that is free of velocity information. The one-sided approach on the other hand yields phase maps that are affected by encoded velocities apparent by the circles that refer to areas of flow.

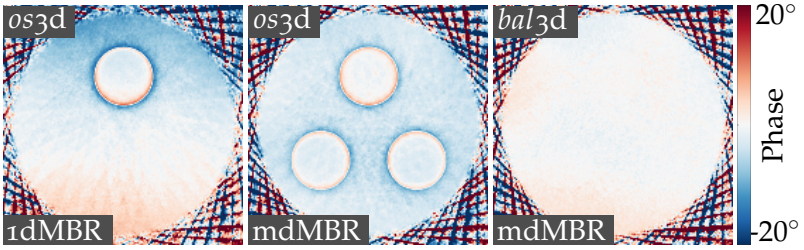

Figure 4.6: Estimated phase reference maps (phase of ρ) of undersampled numerical phantom in correspondence to the velocity maps given in Figure 4.5. While the one-sided methods show deviations from the ground truth (zero), the balanced encoding scheme yields an accurate and homogenous phase reference map.

Initializing all velocity maps with zero, the first estimate for ρ is formed by an unweighted summation over all encoding steps. This can be seen with $v_d = 0$ in the first entry of the adjoint operator $DF^H(\mathrm{x})$. For *bal*3d the summation along the encoding dimension results in a clean phase reference ($\Phi_0 = 0$) despite any encoded velocities as they naturally cancel out by design of the encoding strategy. For *os*3d, however, the phase reference is affected ($\Phi_0 \neq 0$) when the estimate assumes $v_d = 0$ but non-zero velocities are present in the data. As a consequence the flow structures (here circles) are apparent in the phase reference maps (Fig. 4.6)
The difference can be understood by comparison of the encoding matrices (Eq. 4.9 and 4.6) and a summation along the encoding dimension. While *bal*3d yields zero, the sum is non-zero for *os*3d, and thus the initial estimate of the phase of ρ includes encoded velocity information. Likewise, the vector sum of the 1^{st}GMs illustrated in Figure 4.4 is zero for *bal*3d, and non-vanishing for *os*3d.
An affected phase reference directly translates into corrupted velocity estimates and explains the "cross-talk" of different velocity components under *os*3d encoding and its inferior convergence behavior.

4.3.2 *In Vitro: Flow Phantom*

After simulating the outcome of acquisition and reconstruction techniques, the feasibility of multi-directional RT PC MRI is demonstrated experimentally. Using the flow phantom under constant flow conditions, Figure 4.7 shows the realization of 2d RT PC MRI.
The experiments were conducted using a VENC of 120 cm/s, $1 \times 1 \times 5$ mm^3 voxel-size, 192 mm FOV, 10° flip angle, and 5 spokes per velocity encoding. With TE/TR of 2.54/3.51 ms for *os*2d and 2.36/3.33 ms for *bal*2d, single frames were acquired within 53 and 50 ms, respectively.
The iterative reconstruction techniques yield velocity maps of high image quality considering the substantial degree of undersampling. In particular, the maps offer high spatio-temporal resolution and are characterized by the lack of phase noise in regions without MRI signal support. The flow patterns are clearly recognizable in the quantitative velocity maps and are supported by qualitative flow information in the anatomical magnitude images.

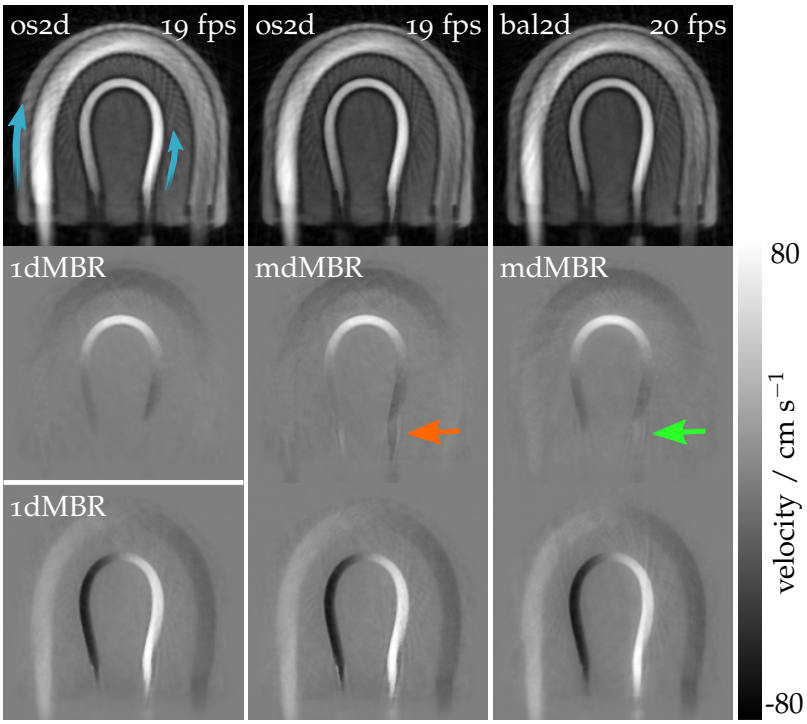

Figure 4.7: Two-directional RT PC variants using the flow phantom (Fig. 2.5.D). Magnitude images (*top*) and two quantitative in-plane velocity maps are shown. The orange arrow indicates an area of false velocity values in the one-sided method. Balancing the velocity encoding scheme reduces this effect (green arrow). Blue arrows indicate the flow direction.

The comparison of acquisition and reconstruction variants essentially confirms the findings of the numerical phantom above. The mdMBR of the *os*2d measurements exhibits velocity "cross-talk" artifacts (*orange arrow*) due to the reasons explained in the pervious section (Chap. 4.3.1). Unfortunately, also its balanced counterpart,

*bal*2d, is not completely free of the "cross-talk" phenomenon. The respective encoding matrix (Eq. 4.8) reveals that the summation over the odd number of encoding steps is non-zero. That is because naturally, there is no way of finding three real-valued numbers of same magnitude that sum up to zero[1]. Consequently, the *bal*2d encoding strategy can be sensitive to wrong velocity allocation via corrupted phase reference estimations as observed for one-sided encoding (*os*1d, *os*2d and *os*3d). Fortunately, the effect for *bal*2d is smaller and the experiments reveal that the *bal*2d method still outperforms the one-sided alternative *os*2d.
To achieve fully balanced conditions in future applications of 2d velocity measurements, adding a fourth encoding step for *bal*2d is conceivable. In this work, however, this step is not considered as it compromises the temporal resolution.
Another difference of both encoding variants affects the choice of acquisition parameters. The balanced method exploits lower first gradient moments allowing shorter TE. The *os*2d achieves a temporal resolution of 19 fps and *bal*2d manages 20 fps. While the difference is moderate for the given example in the high-VENC regime, it is potentially more pronounced for lower VENC values (= higher gradient moments) and again renders the balanced approach preferable.

4.3.3 *In Vivo: Aortic Arch*

The next step in evaluating the novel imaging techniques is the in-vivo application on human subjects. Figure 4.8 shows the results of 3d flow at the human aortic arch being one of the largest blood vessels with high flow values and rapid velocity changes and a potential candidate for future clinical applications.
The experimental parameters included: VENC = 150 cm/s, $1.8 \times 1.8 \times 6$ mm^3 spatial resolution, 320 mm FOV, 5 spokes, and TE/TR = 2.12/3.12 ms resulting in 16 fps temporal resolution. Systolic frames of a continuous time series are shown for the different acquisition and reconstruction techniques of 3d velocity encoding.
The results demonstrate the realization of 3d PC MRI at high spatio-temporal resolution under free breathing conditions and without pro- or retrospective data sorting. Quantitative velocity maps in all three orthogonal flow directions are obtained with minimal undersampling artifacts and good image quality considering the fact that only five different projections (spokes in k-space) are acquired per frame.

A comparison of presented acquisition and reconstruction variants reveals an underestimation of velocities by the 1dMBR. This can be ascribed to the slower convergence as already observed for the numerical phantom (Chap. 4.3.1). The multi-directional reconstructions achieve higher and more reliable quantitative velocity values.
The mdMBR of the *os*3d data exhibits areas of velocity "cross talk" artifacts. The phenomenon is evident in the through-plane (TP) flow map at the descending aorta and constitutes a clear exclusion criterion.
The *bal*3d acquisition and mdMBR yield the best results. The benign convergence behaviour results in robust quantitative velocity values without any cross talk

1 Likewise, the Hadamard transformation is only defined for *bal*1d and *bal*3d but not *bal*2d.

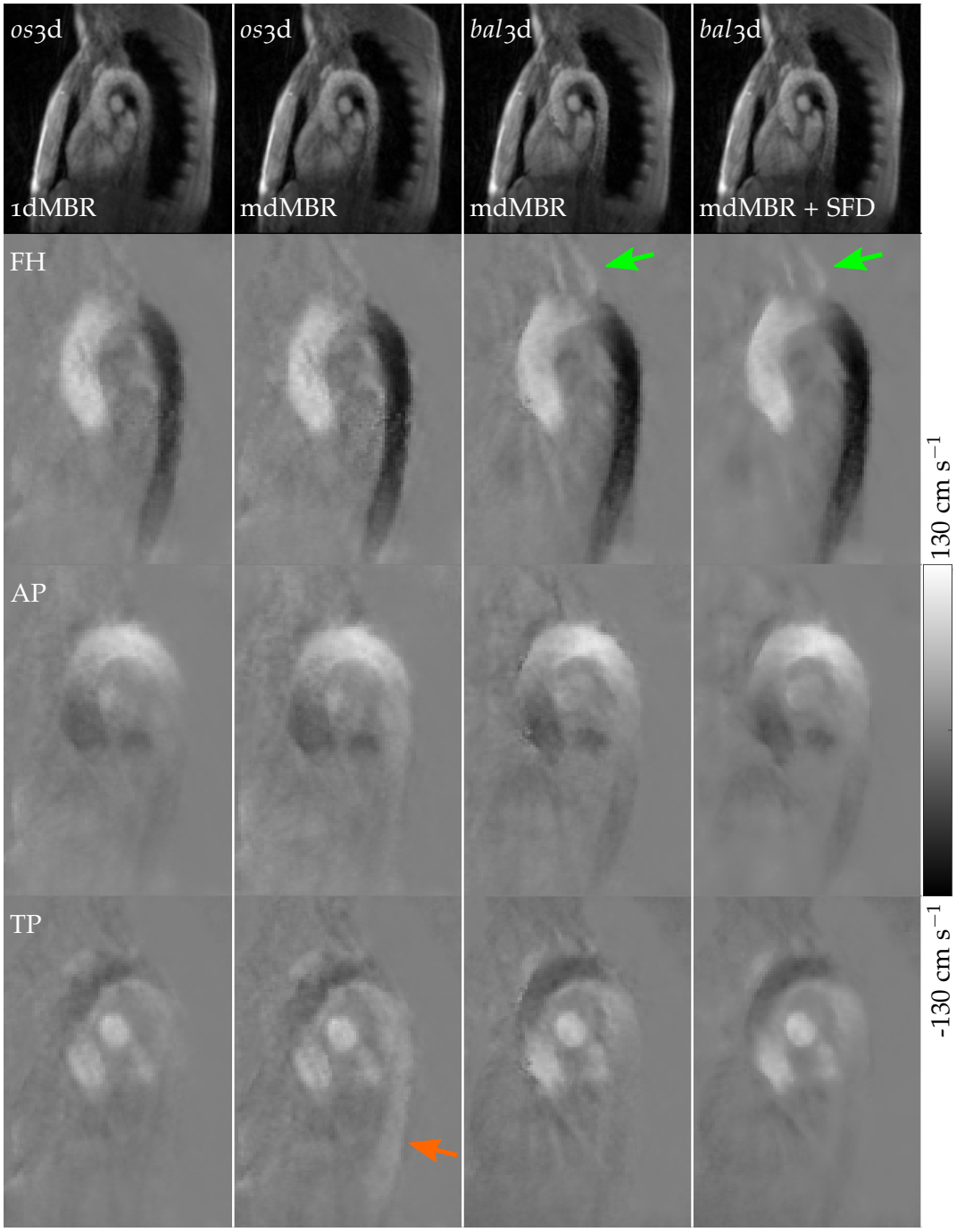

Figure 4.8: Three-directional RT flow variants at the aortic arch. Magnitude images (*top*) and quantitative velocity maps in feet-head (FH), anterior-posterior (AP) and through-plane (TP) direction. The single systolic frames are taken from a continuous time series acquired at 16 fps. The orange arrow indicates false velocity values and the green arrows point on subclavian artery branches not visible in the other reconstructions. Smoothing of the flow direction (SFD) further improves the image quality as described in Chapter 5.1.

artifacts. Furthermore, the small subclavian artery branches are better identifiable in this data set.

In conclusion, the in-vitro and in-vivo results prove the feasibility of multi-directional RT PC MRI based on undersampled radial FLASH and iterative non-linear image reconstruction. Differences in the velocity encoding strategy and corresponding reconstruction variants of the novel mdMBR render the balanced encoding scheme superior to the one-sided alternative.

4.4 VISUALIZATION

This chapter presents additional ways of visualizing multi-directional flow data. In the classical approach individual velocity maps are visualized in grayscale, as shown in the examples above. Zero flow is represented in gray, whereas black and white correspond to the maximum velocity in opposite directions and multi-directional flow is displayed by its individual velocity components.
Instead of using the cartesian representation, any vector can be described by its length and orientation (polar representation) which in the present context are termed speed and flow direction. Depending on the clinical application the display of these quantities may be helpful and potentially more intuitive to read.

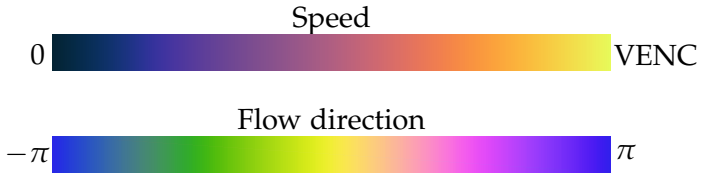

Figure 4.9: Color maps for speed and flow direction.

Figure 4.9 shows color maps proposed for both quantities taken from [49] and [50]. For the special case of 2d in-plane flow, speed and in-plane flow direction can be combined into a joint representation using the color wheel given in Figure 4.10. It visualizes absolute velocities as brightness and includes the flow direction by color coding.

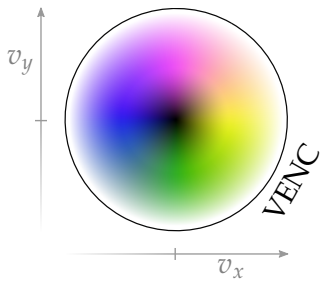

Figure 4.10: Color wheel for 2d in-plane flow.

An overlay on the corresponding T_1-weighted magnitude images M may add further insights resembling Doppler ultrasound. Because the almost noiseless PC maps require no masking, overlay images I may easily be calculated by a linear combination for example in RGB space. In this work, the linear combination is performed for speed values smaller than half their maximum and higher velocity values are displayed completely:

$$I^{\mathrm{RGB}} = \begin{cases} S^{\mathrm{RGB}} & \text{for } S \geq S^{max}/2 \\ \alpha \cdot S^{\mathrm{RGB}} + (1-\alpha) \cdot M^{\mathrm{RGB}} & \text{for } S < S^{max}/2 \end{cases} \quad \text{with} \quad \alpha = \frac{2\,S}{S^{max}}$$

Here, S represents the speed (square root of sum of squares over velocity components) and S^{max} its maximum close to the VENC. The formula is either used for overlaying the speed map S onto the magnitude image M or the 2d in-plane flow map IPF visualized by the color wheel. Figure 4.11 demonstrates both visualization techniques for 2d in-plane flow encoding in a circular flow phantom with tangential inlet.

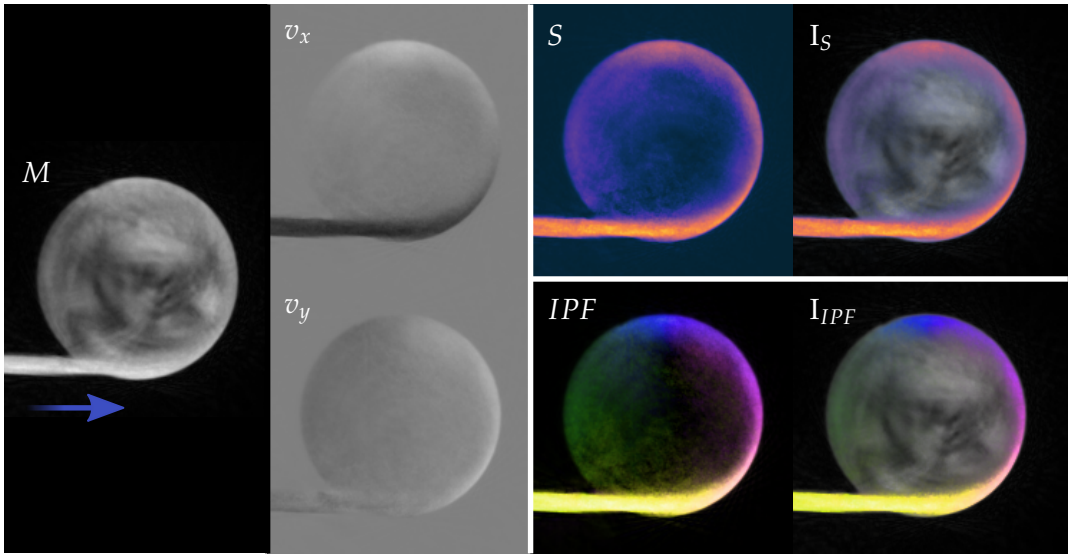

Figure 4.11: Visualizations for 2d flow in circular phantom with tangential inlet. *From left to right:* Magnitude image, PC maps, speed *(top)* and in-plane flow map *(bottom)* plus overlays onto the magnitude image. On the right, three images are combined into one joint representation.

The approach provides the viewer with information of velocity maps and anatomy in a single image. While the PC maps best cover high velocities close to the VENC, qualitative information of low flow is captured in the magnitude image. The latter inherently posses a flow sensitivity due to inflow and dephasing effects.
Figure 4.12 and Figure 4.13 demonstrate speed and in-plane flow visualization for the aortic arch. The in-plane flow image is limited to 2d velocity encoding, whereas the speed image is applicable to 3d velocity encoding as well.

Alternative representations, such as vector plots, were found unfavorable due to the high spatial resolution of the quantitative velocity maps and streamlines or pathlines that commonly rely on more extensive post-processing steps preclude a direct online display. The proposed technique on the other hand is free of any user interaction such as streamline seeding or masking and can be generated fully automatedly. Using combined flow information in a single image makes it potentially easier and faster to capture the flow dynamics of interest which is especially relevant for future interactive RT imaging.

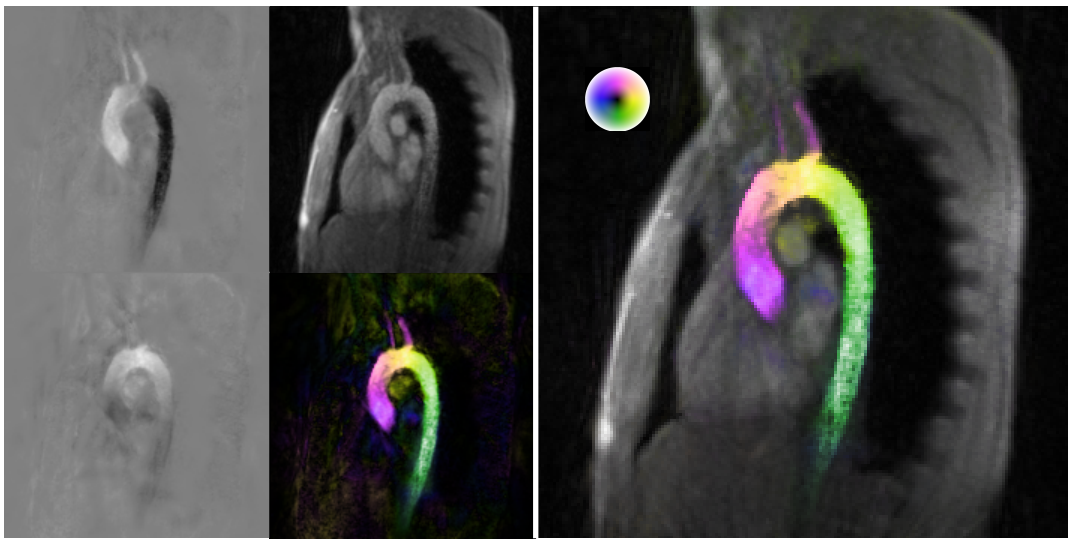

Figure 4.12: Visualization of 2d in-plane flow in the aortic arch. Colors indicate the flow direction by means of the color wheel given in Figure 4.10.

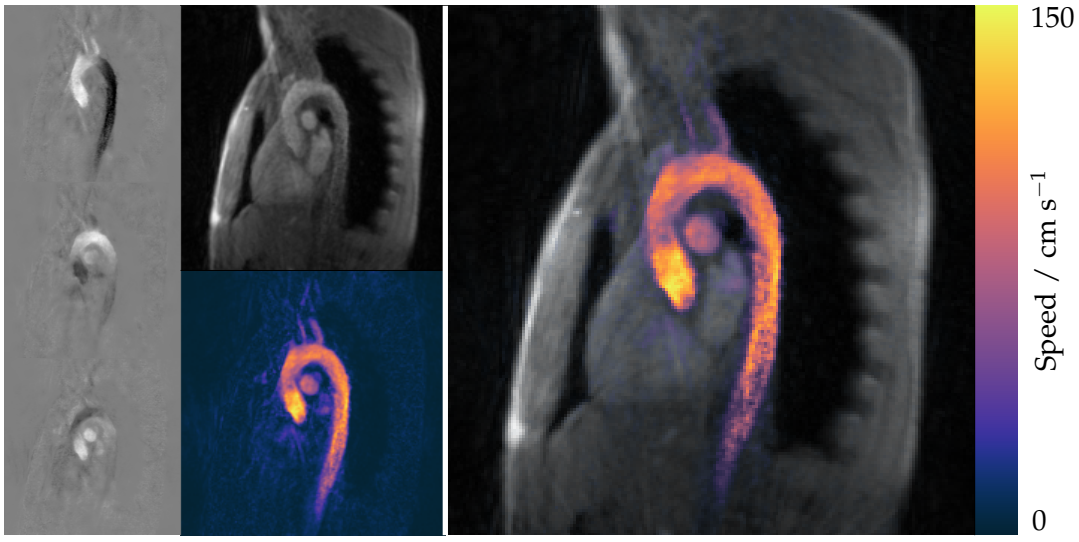

Figure 4.13: Visualization of speed in aortic arch acquired using 3d velocity encoding. Information relevant to peak velocity estimation is condensed from four into one image.

4.5 DISCUSSION

For the first time, this work demonstrates the feasibility of multi-directional velocity quantification using PC MRI in real time. The basic flow sensitivity (Chapter 3) was extended to in-plane velocity measurements and the corresponding pulse sequence was gradually optimized laying the foundation for time-efficient velocity encoding and thus fast imaging. Different velocity encoding strategies are presented and evaluated, as well as an associated model-based image reconstruction that estimates velocity vectors from highly undersampled data sets.
The results point out the benefits of balanced velocity encoding which i) has generally smaller gradient moments and thus allows potentially shorter acquisition times and ii) at the same time favors the convergence of the iterative image reconstruction. At this point, the advantages of the novel reconstruction technique (mdMBR) include the applicability to balanced velocity encoding and in comparison to its uni-directional variant (1dMBR), the combination of raw data from more than two different flow encodings. However, redundancy inherent in these flow encodings was not yet fully exploited. Chapter 5 starts there and introduces refinements for the multi-directional RT PC MRI technique.

5

REFINEMENTS

The mdMBR introduced in Chapter 4.2 reconstructs velocity vectors based on the assumptions that all velocity encoding steps share the same image content ρ and coil sensitivities c_j. Prior knowledge on the velocity vectors themselves so far has not yet been included. Ways to do so are presented in this chapter that begins with the introduction of a velocity denoising strategy. Subsequently, the use of complementary k-space information and the concept of shared velocity encoding present further refinements of multi-directional RT PC MRI.

5.1 SMOOTHING OF FLOW DIRECTION

This work proposes to incorporate a denoising strategy into the iterative image reconstruction that is based on the assumption that velocity vectors of adjacent pixels are likely to point in similar directions. This prior knowledge is incorporated by forcing the map indicating the flow direction to be spatially smooth. For that purpose, a discrete 2D Gaussian smoothing kernel is applied after each Gauss Newton iteration.

Methods

In a first step, the speed S and flow direction D for two velocity components v_1 and v_2 are calculated:

$$S = \sqrt{v_1^2 + v_2^2} \tag{5.1}$$

$$D = \operatorname{atan2}(v_1, v_2) \tag{5.2}$$

Next, D is smoothed by the convolution with a Gaussian kernel K which observes phase periodicity.

$$D^{\dagger} = D \otimes K \tag{5.3}$$

Whereby phase jumps from π to $-\pi$ are preserved and not falsely smoothed out. The filter strength is specified by the standard deviation σ of the Gauss kernel, which simultaneously determines the size of the corresponding convolution kernel $n = 2\lceil 2\sigma \rceil + 1$ avoiding the introduction of additional parameters. The velocity components with smoothed orientation are then given by:

$$v_1' = S \cdot \sin(D^{\dagger}) \tag{5.4}$$

$$v_2' = S \cdot \cos(D^{\dagger}) \tag{5.5}$$

Note that this way, the velocity vector length S remains untouched and only the vector orientation is changed. Neighboring vectors are oriented according to their vicinity.
At this stage, the approach does not account for the reliability of a specific vector orientation. Instead, the random orientation of a noisy vector close to zero contributes the same as the one of an accurately determined high velocity vector. That is compensated for by means of a weighted average specified by the linear combination of the original and the filtered velocity:

$$\alpha = {}^{S}/_{VENC} \tag{5.6}$$

$$v_1' = \alpha \cdot v_1 + (1-\alpha) \cdot S \cdot \sin(D^{\dagger}) \tag{5.7}$$

$$v_2' = \alpha \cdot v_2 + (1-\alpha) \cdot S \cdot \cos(D^{\dagger}) \tag{5.8}$$

While areas of low flow ($\alpha \approx 0$) experience total filtering, high velocities near the VENC ($\alpha \approx 1$) stay untouched. This selected filtering allows effective denoising and simultaneously preserves accurately measured data. Velocities in the mid range ($\alpha \approx 0.5$) benefit from the linear combination by an implicit denoising. Even though S is not touched explicitly, the averaging of two vectors differing in orientation reduces the length of the resulting vector. Therefore, S is reduced implicitly whenever velocity vectors do not fit the orientation of their surroundings.
The smoothing of flow direction (SFD) is performed after each Newton iteration for all pairs of velocity components. While the implementation for 2d velocity encoding is straightforward, SFD is performed three times for 3d velocity encoding (once for each pair of v_i) and the final maps obtained by averaging.

Results

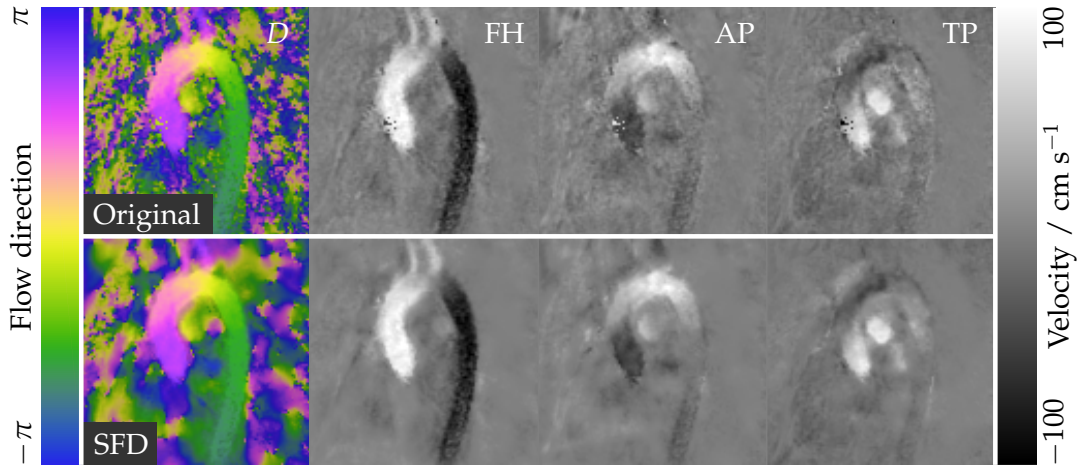

Figure 5.1: Smoothing of flow direction (SFD) with $\sigma = 2$ for 3d flow in the aorta. On the left, the in-plane flow direction is shown.

Figure 5.1 demonstrates the performance of SFD for 3d velocimetry in the aorta with the same experimental parameters as listed in Chapter 4.3.3. The noise level is

reduced without compromising image sharpness in the velocity maps. As the Gauss smoothing is limited to the vector orientation but not its individual components, vessel boundaries may remain sharp without being blurred.
On top of that, SFD prevents the occurrence of phase wrap artifacts in the given example apparent in the ascending aorta. Velocity values exceeding the VENC run the risk of being interpreted as negative values ($\pi + \epsilon \rightarrow -\pi + \epsilon$) resulting in flow directions that are not in accordance with their vicinity. Here, the procedure of SFD can be understood as turning corrupted velocity vectors back to their right orientation. In the same way, partial volume artifacts at the vessel's boundary are reduced.
Note that the unfiltered flow direction map is already spatially smooth along the aortic arch. No abrupt chances of flow direction occur, which inspired the idea of improving the velocity maps by SFD.

The SFD performance depends on the choice of σ defining the filter's size and strength. While too small σ render the filter ineffective, too large values run the risk of loosing detailed flow information of smaller scales. This relation is demonstrated in Figure 5.2 covering SFD results with $\sigma = 0, 1, 2, 5$ and 10 pixels.
With increasing σ the noise level and residual streaking artifacts decrease and the results approach clean velocity maps where only the large scale flow pattern of interest remains. However, as can be seen in the difference images, too high σ values affect the actual velocities of interest and thus the method's validity as a quantitative imaging tool. Therefore, a more conservative choice of σ is advisable. A value of $\sigma = 2$ pixels was found to best balance both extremes for the examples shown.
Figure 5.3 demonstrates the effect of SFD for different numbers of Newton iterations. With SFD the creation of numerical noise and phase wrap artifacts are consistently suppressed. That allows a higher number of Newton iterations corresponding to a gain in accuracy, which would normally go along with increased noise levels as the regularization strength decreases.
It is important to mention that the filters performance benefits from its iterative application (rather than applying it in one final post-processing step) by eliminating phase wraps in each Newton step's initial image.

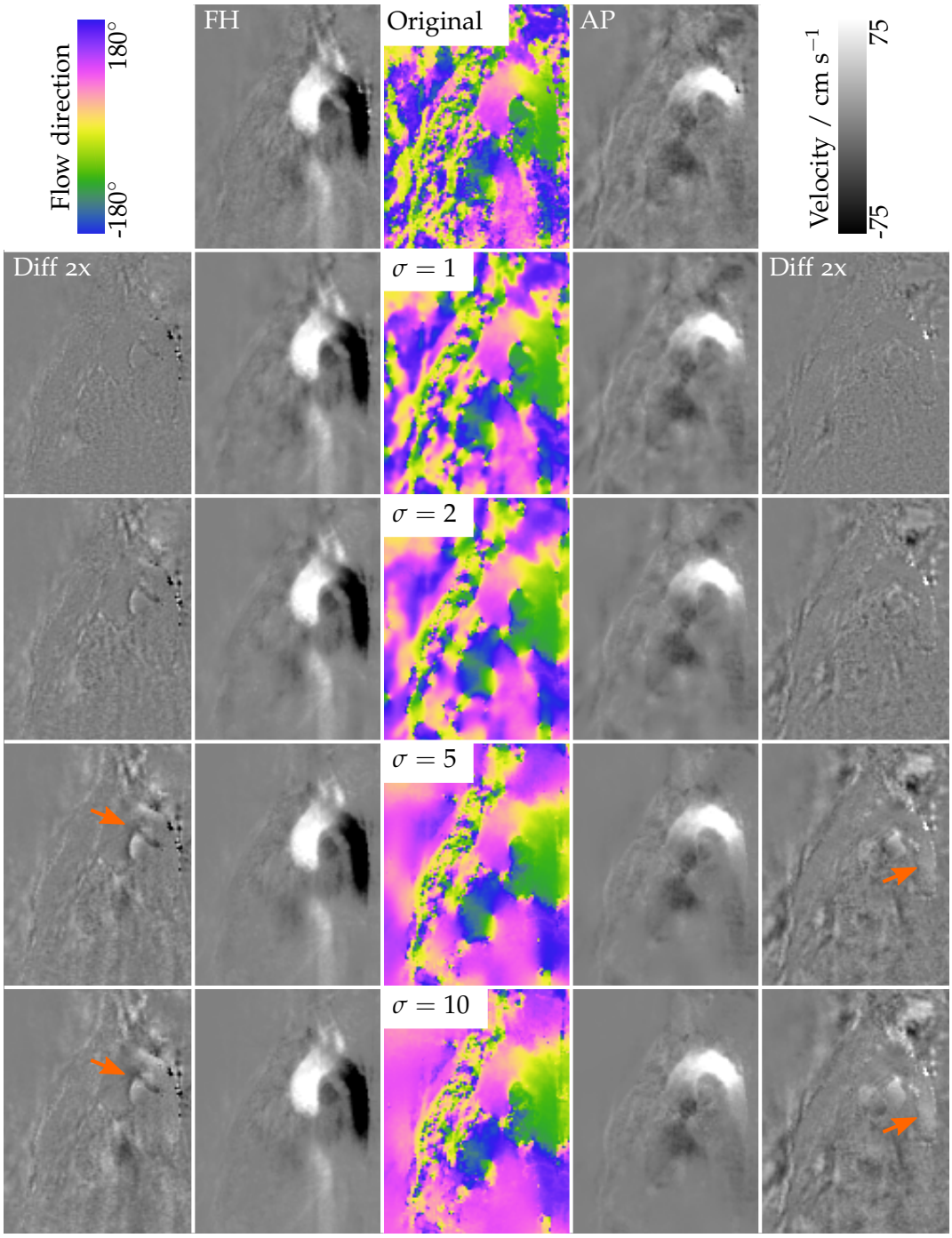

Figure 5.2: Smoothing of flow direction for different filter strengths. The choice of σ balances i) the degree of artifact and noise suppression and ii) the loss of flow information in smaller structures. Note that for all values the sharp edges of vessel boundaries in the velocity maps are preserved, as the smoothing is limited to the flow direction. Orange arrows indicate regions where the velocity of interest is affected.

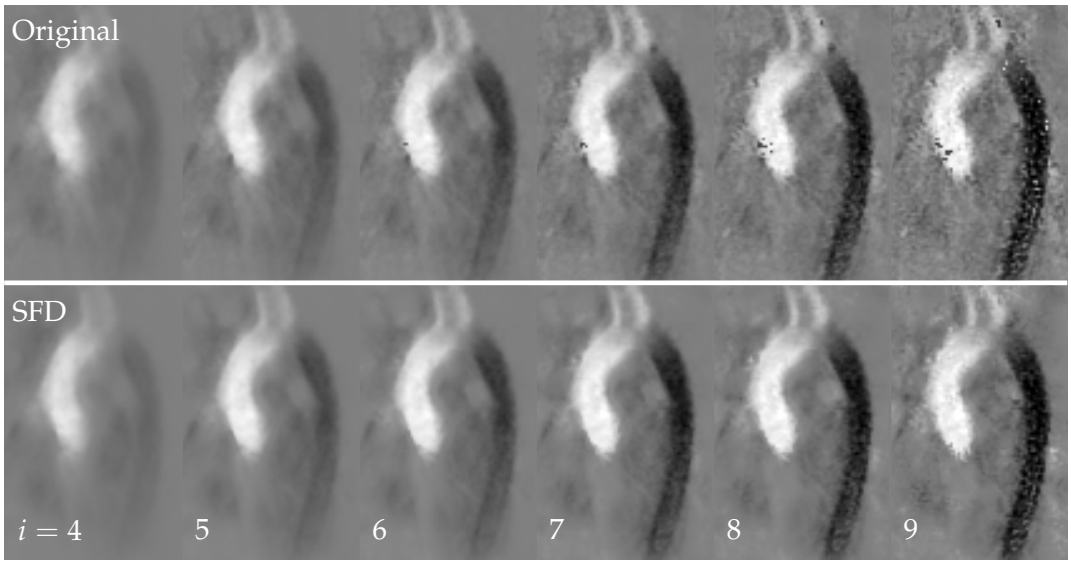

Figure 5.3: Smoothing of flow direction (SFD) for different Newton iterations. FH velocity maps are shown acquired by 3d velocity encoding in the aortic arch. SFD suppresses the creation of noise and phase wrap artifacts. For $i = 7$ the reconstruction is converged and the noise level acceptable.

Discussion

SFD relates to the assumption of blood to be incompressible and divergence-free which is exploited in several *4D flow* techniques [51, 52, 53] to improve volumetric velocity estimations. Due to the fundamental difference of volumetric (3D) and cross-sectional (2D) imaging, however, the reported approaches are not directly applicable to this work, as for 2D imaging the spatial dimension (and derivative) perpendicular to the imaging plane are not accessible and a 2D divergence freedom would be violated by any through-plane flow. SFD presents a heuristic workaround to correlate individual velocity components and thereby improve their estimation. It is computationally inexpensive and most importantly points out the potential of coupling the vector components during their joint reconstruction. The results show that a correlated estimation better exploits the redundancy inherent in the velocity components than an independent estimation does.
Further investigations might focus on locally adaptive filter strengths for SFD or on more elaborated velocity denoising techniques e.g. based on total variation [54]. Moreover, it is desired to incorporate the prior knowledge, e.g. on smooth flow directions, as an additional regularization term in the mdMBR.

5.2 COMPLEMENTARY SETS OF SPOKES

In PC MRI the flow encodings differ in phase. Their magnitude images, however, are known to be nearly identical. Using the SAMESPOKES k-space trajectory described in Chapter 4.1.3, the novel multi-directional RT PC method does not fully exploit the redundancy inherent in all flow-encoding steps. Instead, all differently encoded measurements rely on the same undersampled radial k-space information for the estimation of common parameters (ρ and c_j).
Complementary spokes, on the other hand, are expected to make better use of the redundancy and thus improve the image reconstruction. In this class of trajectories, different projections for successive flow-encodings are acquired as illustrated in Figure 5.4.

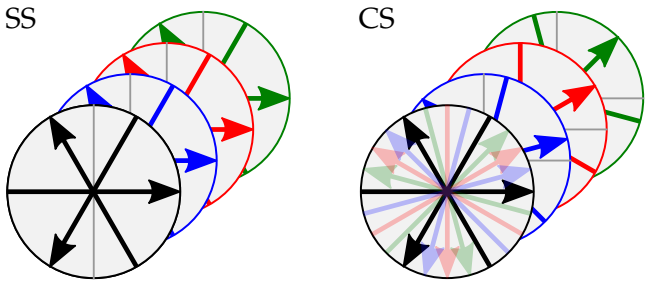

Figure 5.4: Same (SS) and complementary sets of spokes (CS). Colors indicate different flow-encoding steps of one frame for 3d velocity encoding.

Radial k-Space Trajectories

This work presents different trajectories that exhibit complementary sets of spokes for uni- or multi-directional PC MRI:

- TILTEDENCODING: This trajectory follows the turn-based radial sampling pattern, but tilts successive flow-encoding steps by a ixed angular increment that is controlled by TF to allow flexibility. The tilting factor TF defines the tilting angle as given in Table 5.1. Figure 5.4 shows a tilting factor of $TF = 0.5$. For $TF = 0$ the SAMESPOKES trajectory is obtained.

- GOLDENANGLE: This trajectory is based on a constant azimuthal displacement from spoke to spoke given by the golden angle Φ_{GA} as proposed in [55]. The constant radial progression by the non-rational golden angle precludes any repetition of spoke orientations and thus provides temporal incoherence. For this sampling pattern it is important to distinguish between an interleaved and a sequential data acquisition (s. Chap 4.1.4).

- HYBRID: This approach describes a combination of the upper two. A homogeneous spoke distribution is chosen for each frame and each encoding is tilted as for TILTEDENCODING. The angular increment from frame to frame, however, is given by the golden angle Φ_{GA}. This way, incoherence in time is obtained without any repetitions while still each frame exhibits a homogenous distribution of spoke angles.

All radial sampling schemes are characterized by means of three different angles: the *spoke angle* φ_S (radial increment from spoke to spoke within single frame and encoding), the *flow encoding angle* φ_E (radial increment between successive flow-encoding steps), and the *frame angle* φ_F (radial increment of the first encoding from frame to frame). Table 5.1 lists the individual angles for the four different k-space trajectories.

	Spoke angle φ_S	Enconding angle φ_E	Frame angle φ_F
SAMESPOKES	2π / N_S	0	2π / $(N_S\, N_T)$
TILTEDENCODING	2π / N_S	$TF \cdot 2\pi/(N_S\, N_E)$	2π / $(N_S\, N_T)$
GOLDENANGLE *interl.*	$N_E\, \Phi_{GA}$	Φ_{GA}	$N_S\, N_E\, \Phi_{GA}$
GOLDENANGLE *sequ.*	Φ_{GA}	$N_S\, \Phi_{GA}$	$N_S\, N_E\, \Phi_{GA}$
HYBRID	2π / N_S	$TF \cdot 2\pi/(N_S\, N_E)$	Φ_{GA} / N_S

Table 5.1: Radial increments for k-space trajectories as function of the number of spokes N_S, the number of flow-encoding steps N_E, and the number of turns N_T. The tilting factor is denoted as TF and Φ_{GA} describes a golden angle [55].

All four trajectories have their respective pros and cons. SAMESPOKES, TILTEDENCODING and HYBRID exhibit a homogeneous spoke distribution per frame and flow encoding, which is especially beneficial for low numbers of spokes. The distribution for the GOLDENANGLE trajectory, however, highly depends on the choice of golden angle [56].
The non-repetitive nature of HYBRID and GOLDENANGLE trajectories improves the sampling of static tissue as always new k-space information is acquired. On the other hand, both trajectories are incompatible with the temporal median filter which cannot effectively remove streaking artifacts without any repetitions in time domain. For this reason, the trajectories are excluded as potential options. Nevertheless, both are listed for the sake of completeness and are potentially promising for alternative and retrospective reconstruction methods that rely on incoherence in time domain and need no median filter (e.g. compressed sensing). In the following, only the remaining two turn-based options, SAMESPOKES and TILTEDENCODING, are applied and further discussed.

Experiments

The TILTEDENCODING with $TF = 0.5$ (s. Tab. 5.1) ensures the combination of complementary spokes to provide a uniform distribution of spoke angles (Figure 5.4). This approach was studied and compared to the SAMESPOKES ($TF = 0$) using the flow phantom (in vitro) and experiments acquired at the aortic arch (in vivo). Three-directional measurements relied on *bal*3d velocity encoding and 5 spokes per encoding like previous experiments. The phantom data was acquired with a VENC of 120 cm/s and TE/TR = 2.08/3.13 ms at $1 \times 1 \times 5$ mm^3 spatial and 15 fps temporal resolution. The in vivo data set was measured at 16 fps temporal and

$1.8 \times 1.8 \times 6$ mm^3 spatial resolution with a VENC of 180 cm/s, $\sigma_{\text{SFD}} = 2$ pxl and TE/TR = 2.12/3.12 ms.

Results

Figure 5.5 summarizes the results obtained using the SAMESPOKES and TILTEDENCODING trajectories. Looking at the flow phantom in particular, the use of complementary spokes visibly reduces residual streaking artifacts and increases image sharpness in the magnitude image. The complementary spatial information adds up in k-space and supports the estimation of the common parameter ρ.
The velocity maps, however, do not benefit in the same way. Here, complementary spokes result in slightly more artifacts and a less homogenous image background. As different flow encodings cover different spatial frequencies in outer k-space, the phase difference is less well defined and the resulting maps are observed to be more prone to experimental errors. These include off-resonances due to fat in the abdominal wall or breast region that show sharp edges at the air-tissue boundary. Nevertheless, the actual flow regions of interest are unaffected, which proves that an image reconstruction under complementary k-space information is principally feasible.

Conclusion

It remains to be evaluated whether the improved image quality of magnitude images under complementary spokes, or the robustness of the velocity maps under same spokes is more decisive for a respective PC MRI application.

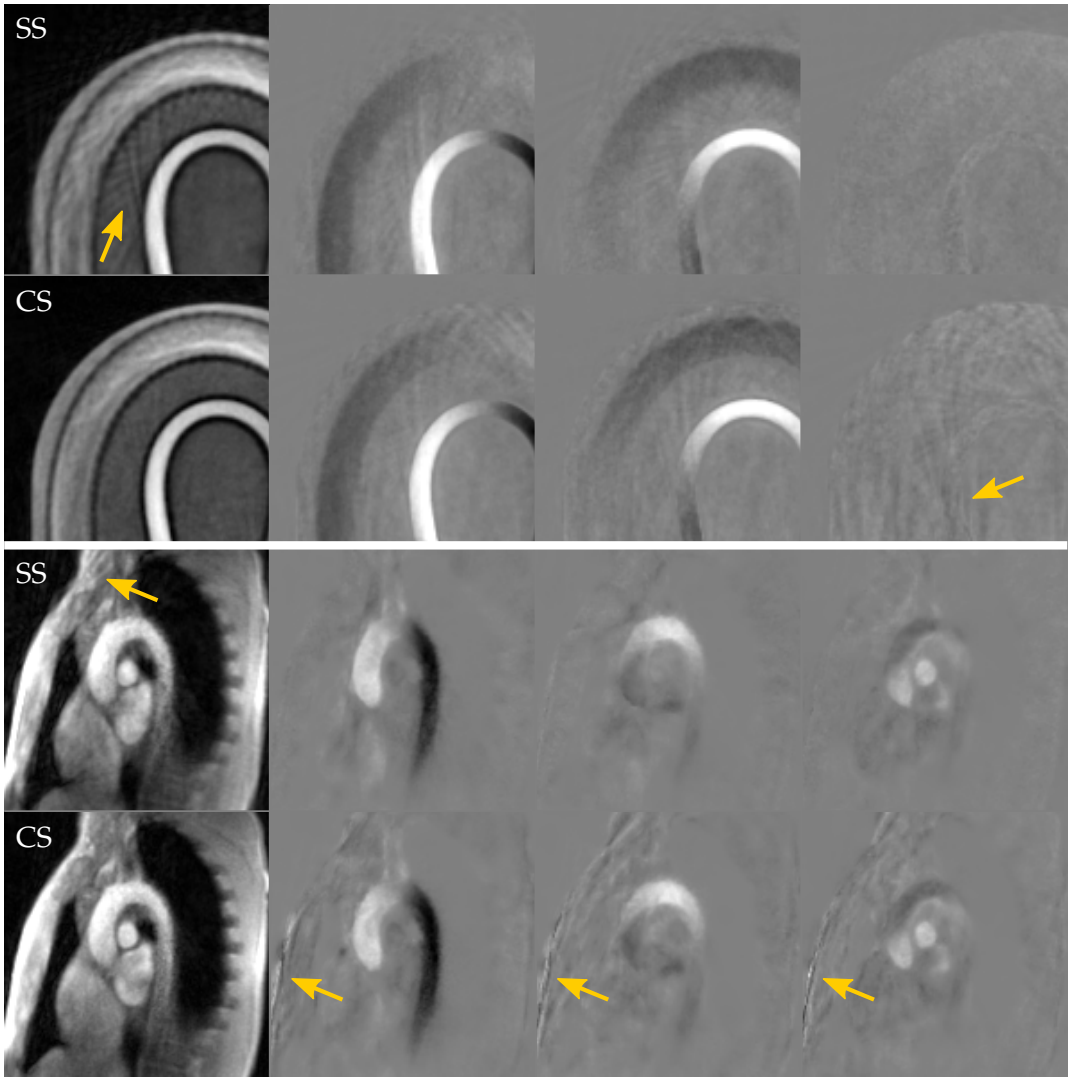

Figure 5.5: Same (SS) and complementary sets of spokes (CS) for 3d velocity encoding of flow phantom (s. Fig. 2.5.D) and human aorta. While magnitude images improve under the use of CS, PC maps slightly deteriorate in the periphery. Yellow arrows point out radial streaking artifacts. Main vessels of interest show no quantitative difference.

5.3 SHARED VELOCITY ENCODING

The use of complementary k-space information allows to increase the number of frames for dynamic PC imaging. Instead of limiting the phase-difference operation to encoding steps of one specific frame, additional velocity maps are created in between successive frames. Figure 5.6 illustrates this principle of shared velocity encoding (SVE) for 1d, 2d and 3d flow. Each encoding step is exploited multiple times for the definition of a phase-difference map. Consequently, the frame update rate increases. The corresponding acceleration factor scales with the number of encoding steps. While for 1d encoding the frame rate is doubled, SVE under 3d encoding achieves an acceleration by a factor of four.

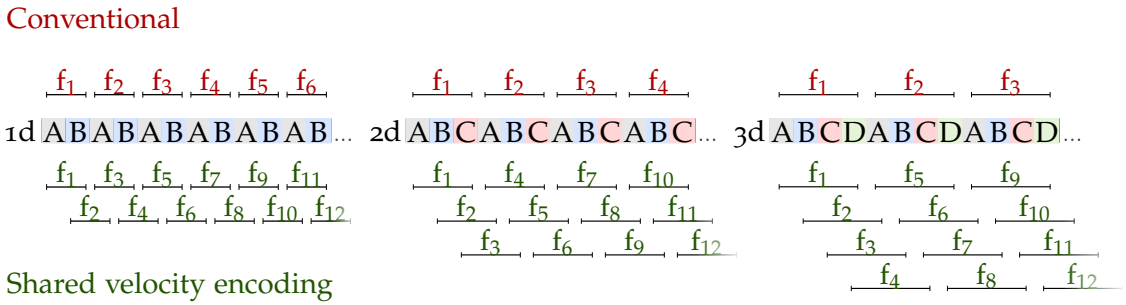

Figure 5.6: Shared velocity encoding for 1d, 2d and 3d flow. Each encoding step (A to D) contributes to multiple frames f_i which increases their rate. Note that under SVE 1d, 2d, and 3d encoding provide the same frame update rates, but different temporal footprints.

Originally described by Bernstein and Foo [57] the idea is investigated in [58] for 1d encoding reporting an improved determination of peak velocities. In this work, SVE is implemented and its performance tested for multi-directional flow.

Methods

The SVE method operates prior to image reconstruction and can be understood as a pre-processing step that replicates and resorts the raw data. Alternatively, the calculation of the additional frames can be realized by respective adaptations in raw data indexing inside the image reconstruction algorithm which is more memory efficient.
The increased frame rate naturally causes a higher similarity between successive frames, wherefore the prerequisites for the temporal regularization are better met and the convergence of the iterative optimization improves. As a result, the number of Newton iterations can be reduced (from 7 to 6) without compromising accuracy in velocity values. Other than that, no changes in the reconstruction procedure are needed and the mdMBR is used as described above (Chapter 4.2.2).
Concerning the image acquisition, the following adaptations have to be considered. The balanced velocity encoding is the only reasonable strategy for the SVE technique, as it is free of flow-compensating encodings that do not carry any velocity

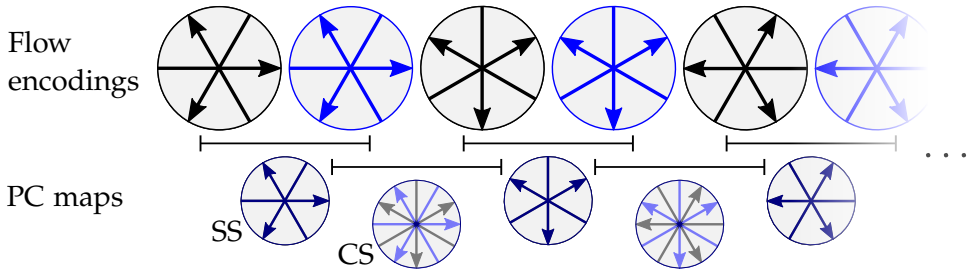

Figure 5.7: SAMESPOKES sampling pattern with different flow encodings *(black & blue)*. For SVE same set of spokes (SS) and complementary spokes (CS) alternate for intermediate frames. Every other PC map is based on different number of projections.

information. Pairing different of these zero-measurements with a flow-encoded step would result in identical velocity maps. Therefore, the one-sided velocity encoding strategy is not applicable for SVE, adding yet another point in favor of the balanced encoding strategy.
In order to achieve a continuous time progression of flow information, the *sequential* acquisition strategy is applied for SVE. The *interleaved* alternative would result in varying and longer temporal footprints (time window of data collection) for the image time series.

Furthermore, the k-space trajectory is adapted for SVE. Figure 5.7 shows the standard SAMESPOKES sampling pattern exemplary for 1d encoding and illustrates the PC maps in k-space under SVE imaging. Same spokes (SS) and complementary spokes (CS) alternate, wherefore the radial displacement and the total number of projections are not constant for successive frames. The same applies for multi-directional flow with more encoding steps.
An alternative trajectory, adapted for SVE, is shown in Figure 5.8. Using the TILTED-SPOKES sampling with a tilting factor of $TF = 1/N_T$ (one over number of turns) the angular displacement is held constant in time and the same number of projections is achieved over all frames. In addition, the tilting angle of complementary spokes is smaller than for the SAMESPOKES trajectory and it further decreases for higher number of flow-encodings. For 2d and 3d velocity encoding, the same tilting factor applies.

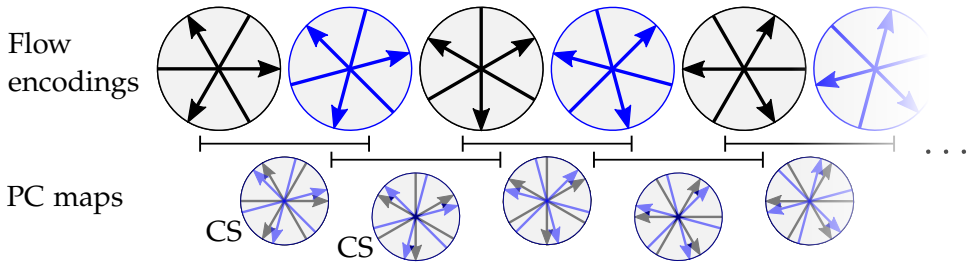

Figure 5.8: TILTEDSPOKES sampling pattern adapted for SVE reconstruction with $TF = 1/N_T$. Successive flow encodings are rotated to achieve a constant angular displacement over successive frames. All PC maps base on the same number of projections.

Comparative experiments were conducted at the aortic arch using the conventional and SVE approach. Except for the novel k-space trajectory, the acquisition parameters matched the ones given in Chapter 5.2 for *bal*3d encoding.

Results

The results are presented in Figure 5.9 showing systolic frames from continuous image time series. While the quantitative velocity maps are comparable, the magnitude image improves significantly with SVE. The four times higher number of projections translates into an increased image sharpness and the reduction of residual streaking artifacts. The difference is apparent in k-space obtained by Fourier transformation of ρ. At the same time, the frame update rate of SVE is four times higher.

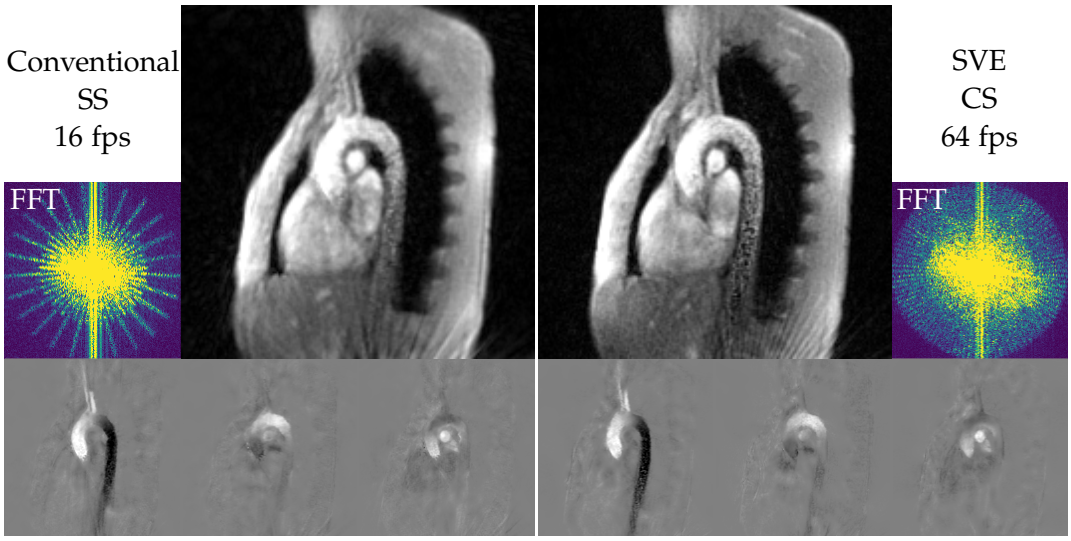

Figure 5.9: Conventional and SVE method for 3d flow at aortic arch. The higher number of projections is apparent in the Fourier space and translates into an improved spatial acuity of the magnitude image. The velocity maps remain comparable.

The sensitivity of complementary spokes to experimental errors mentioned in Chapter 5.2 varies from data set to data set and still affects the PC maps infrequently. Figure 5.10 gives another example of a 3d velocity-encoded data set and demonstrates the artifact creation due to off-resonances in fat regions. While the robustness of the SameSpokes trajectory is still unsurpassed and no artifacts occur, the TiltedSpokes trajectory shows artifacts at the sharp fat-air transition of the abdominal wall. The use of SVE reconstruction for this data set reduces them significantly. This effect can be ascribed to the higher regularization strength and to the higher similarity of succeeding frames and thus better initialization and condition of the inverse optimization problem. The actual flow regions of interest are represented comparably well for all three methods shown.

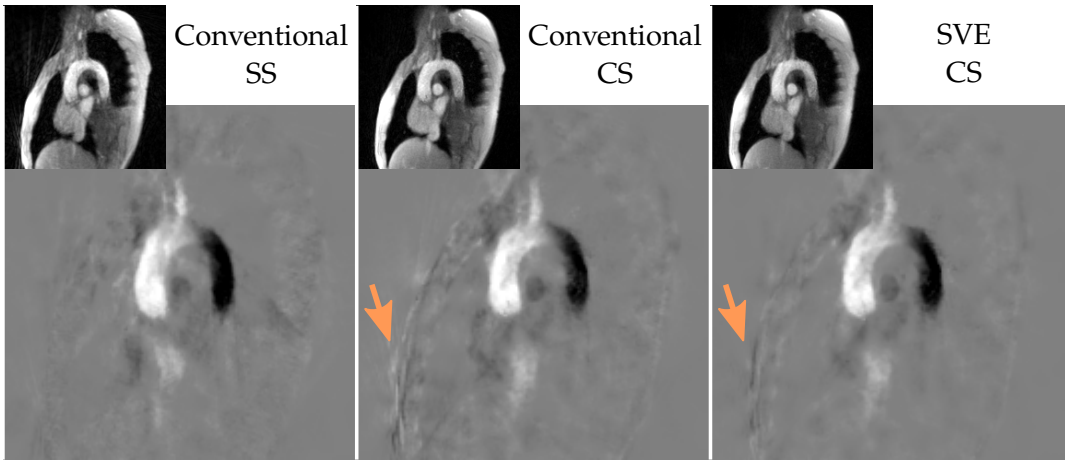

Figure 5.10: Sensitivity of complementary spokes (CS) towards off-resonances and its reduction by SVE. Orange arrows point out artifacts at fat-air transitions.

Even though SVE increases the frame rate, the true temporal resolution does not necessarily experience the same acceleration. Successive frames in SVE are statistically dependent as they share one or more flow-encoding measurements. Therefore the temporal footprint per velocity map remains largely unchanged.
Still, SVE reconstruction is substantially different from a retrospective temporal interpolation mostly in that each time frame in SVE has large contributions from the corresponding data fidelity term, especially in the k-space center. Interpolation, on the other hand, averages k-space centers blindly in time. On top of that, interpolation would be retrospective and would therefore further delay a direct online display.

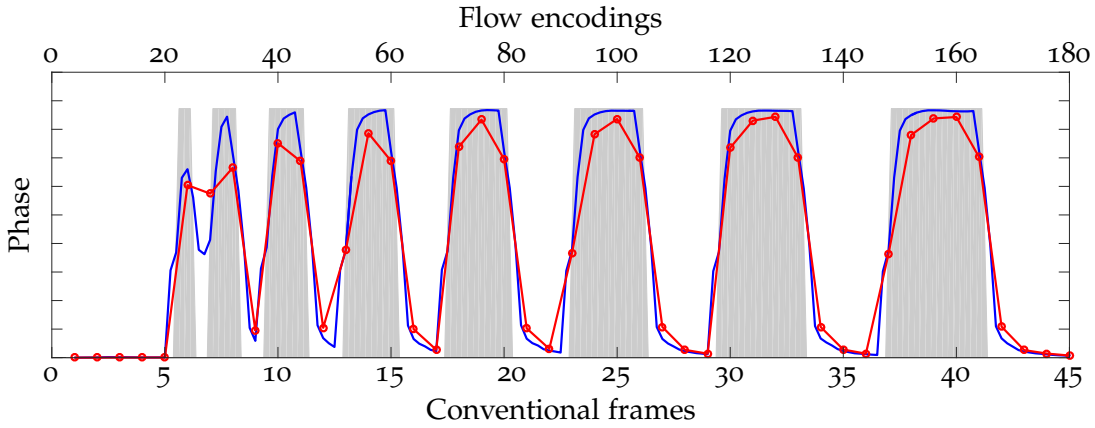

Figure 5.11: Simulated comparison of conventional and SVE reconstruction. *Gray:* ground truth, *red:* conventional method and *blue:* SVE with four times denser sampling. The data is obtained after ROI evaluation of a numerical phantom.

The prerequisites for the temporally regularized reconstruction are generally better met for the SVE technique than for conventional PC imaging, due to a higher similarity of successive frames. A quantitative comparison is given in Figure 5.11 showing velocity time curves obtained by means of the numerical phantom as introduced in Chapter 4.3.1. Here, the ground truth is known precisely and designed to dynamically switch between phase difference values of 0° and 100° with varying frequency.
The SVE approach better captures peak velocities and identifies shorter pulses than the conventional method which corresponds to an effective gain in temporal resolution.

Additional frames naturally come at the expense of extra computation times which constitutes the only drawback of the SVE approach. Nevertheless, the computational effort per frame decreases. That is because each frame is initialized closer to its solution and thus less Newton iterations are required for a proper convergence. In general, the mdMBR is expected to highly benefit from a parallelized implementation on multiple high-performance GPUs to minimize reconstruction times. For the SVE approach in particular, 3d encoding with a frame rate acceleration by a factor of two instead of four could be considered a reasonable compromise with lower computational demand.

Conclusion

Aside from its additional computation times, the SVE approach combines significant improvements in spatial and temporal domain, and therefore constitutes an important step in the development of multi-directional RT PC MRI. SVE allows to display quantitative 3d velocity information at the same frame update rate as the usually faster 1d velocity encoding technique. The temporal footprints per velocity map, however, remain unchanged.

5.4 SUMMARY

Subsequent to the development of multi-directional velocimetry based on cross-sectional real-time MRI (Chapter 4) this chapter proposed refinements to further improve the novel imaging technique. These are i) velocity denoising by SFD gaining VNR and preventing phase wrap artifacts, ii) alternative radial sampling trajectories exploiting complementary k-space information and thus gaining spatial acuity, and iii) an increase in frame update rate by SVE gaining effective temporal resolution and an improved initialization of the ill-posed reconstruction problem.

	PREVIOUS WAY	PROPOSED WAY
Sequence design:	independent gradients	merged gradients
Velocity encoding:	one-side	balanced
Trajectory:	same spokes	complementary spokes
Image reconstruction:	1dMBR	mdMBR
Velocity denoising:	none	SFD
Frame rate:	conventional	speed up by SVE

Table 5.2: Summary of refinements for multi-directional PC RT MRI.

Table 5.2 lists the individual steps of gradual methodical improvement presented in Chapters 4 and 5. The combined effect of all steps taken together was compared against the previous approach[1] for 2d in-plane flow encoding. For a fair comparison the nominal spatial resolution was kept constant at $1.8 \times 1.8 \times 6$ mm^3 and 5 spokes per flow encoding were used for both techniques, along with overlapping gradients and an asymmetric echo (s. Fig. 3.7). The results are demonstrated in Figure 5.12. The simultaneous improvement in spatial and temporal domain achieved here, can mainly be reduced and ascribed to i) the time-efficient pulse sequence design for fast acquisitions, and ii) the better use of redundancy inherent in multiple velocity encodings during image reconstruction.

1 The previous approach can be seen as a minimal goal obtained by a plane extension of the established 1d technique to multi directional flow.

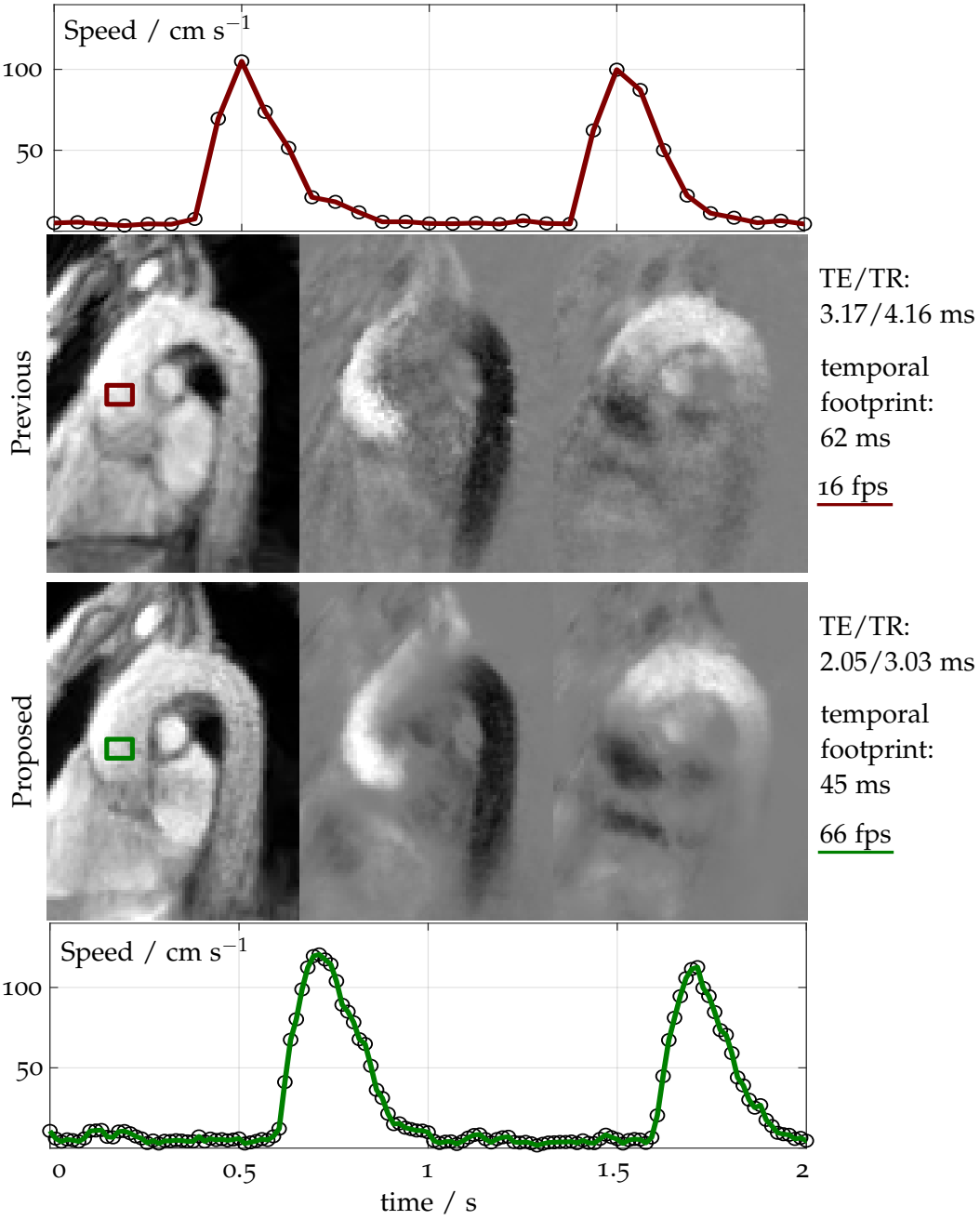

Figure 5.12: Comparison of previous and proposed method with all features listed in Tab. 5.2 for 2d in-plane flow at aortic arch. Higher SNR in the velocity maps and higher image sharpness of the magnitude image indicate the gain in spatial domain, whereas the ROI evaluations demonstrate the improved temporal acuity of the new method.

6

MAXWELL CORRECTION FOR RADIAL TRAJECTORIES

In the previous three chapters RT PC MRI is presented and technical extensions and improvements discussed. This chapter presents the Maxwell correction for radial PC MRI which constitutes another important and fundamental technical development. The technique predicts phase offset errors in quantitative velocity maps and automatically corrects for these during image reconstruction.
Parts of this chapter have been accepted for the annual conference of the *International Society for Magnetic Resonance in Medicine* (ISMRM) in 2020.

6.1 BACKGROUND

Whenever a linear magnetic field gradient is applied, so-called concomitant magnetic fields result. The B_0 field no longer aligns in z-direction but non-vanishing transversal components, B_x and B_y, arise. These additional magnetic fields are a consequence of Maxwell's equations that in the absence of electrical currents and vanishing temporal derivatives demand the magnetic field to be divergence- and curl-free [15]. In PC flow MRI, the deviations from the nominal magnetic field lead to the accumulation of extra phase terms, that in turn result in corrupted velocity maps. Fortunately, these concomitant magnetic fields B_C, also known as Maxwell terms, are analytically determinable and to the lowest order well approximated by:

$$B_C(x,y,z,t) = \frac{1}{2B_0}\left(G_x^2z^2 + G_y^2z^2 + G_z^2\frac{x^2+y^2}{4} - G_xG_zxz - G_yG_zyz\right) \tag{6.1}$$

Here, x, y and z denote the physical coordinates with respect to the isocenter and $G_{x/y/z}$ correspond to the (time dependent) magnetic field gradients.
The effect of concomitant fields is usually very small and often neglected under standard imaging conditions or high magnetic fields B_0. With high gradient amplitudes of modern MRI systems, however, the Maxwell terms gain in relevance, as reflected by its proportionality to G^2/B_0. In this case, non-negligible phase contributions have to be considered which are obtained by temporal integration:

$$\phi_C(x,y,z) = \gamma \int B_C(x,y,z,t)\,\mathrm{d}t \tag{6.2}$$

In PC MRI, the impact on quantitative velocity maps is corrected for by the so-called Maxwell correction, introduced by Bernstein et al. [15]. The phase error $\phi_C(x,y,z)$ is calculated and afterwards treated as a phase offset map to achieve clean velocity maps. For that purpose, Equation (6.1) and (6.2) are summarized in four coefficients

determined by the individual gradient waveforms and calculated in the pulse sequence:

$$\begin{aligned} A &= \frac{\gamma}{2B_0} \int G_x^2(t) + G_y^2(t)\,\mathrm{d}t & C &= -\frac{\gamma}{2B_0} \int G_x(t) G_z(t)\,\mathrm{d}t \\ B &= \frac{\gamma}{8B_0} \int G_z^2(t)\,\mathrm{d}t & D &= -\frac{\gamma}{2B_0} \int G_x(t) G_y(t)\,\mathrm{d}t \end{aligned} \tag{6.3}$$

Given these coefficients along with the physical coordinates of the imaging plane, the Maxwell phase with non-linear spatial dependency is calculated in image space and corrected for during the PC image reconstruction.

$$\phi_C(x, y, z) = A\,z^2 + B\,(x^2 + y^2) + C\,xz + D\,yz \tag{6.4}$$

Note that the original work defines the coefficients A to D based on the difference between different flow encodings in accordance to the phase-difference operation. This work, however, uses individual coefficients for each encoding to allow for a higher flexibility and, in particular, also the applicability to multi-directional and balanced velocity encoding.

The Maxwell correction [15] described above has evolved as the standard technique for the suppression of concomitant field effects in PC MRI [59, 60]. Unfortunately, it is not applicable to RT PC MRI with radial trajectories as it is conceived for standard Cartesian imaging. Previous publications on radial PC MRI either i) applied a retrospective manual correction [61] unsuited for interactive RT imaging and incapable of addressing potential inter-spoke differences in Maxwell terms, or ii) did not comment on Maxwell correction and neglected the influence of concomitant magnetic fields [62, 9].
This work demonstrates that Maxwell phase errors for multi-directional RT PC MRI as described in Chapter 4 are not negligible although applied at comparably high magnetic field strength ($B_0 = 3$ T). Furthermore, the influence of the key imaging parameters, TE and VENC, on respective Maxwell terms is investigated and a Maxwell correction proposed that is conformed to radial trajectories.

6.2 METHODS

For the most commonly used Cartesian sampling, Maxwell terms are constant over different k-space lines as only the phase-encoding gradient is incremented and the read gradient remains unchanged. Therefore it is sufficient to derive the Maxwell coefficients from the gradient waveform of one single (central) k-space line.
In radial imaging, however, the read gradients constantly change and corresponding Maxwell terms may vary. To account for that, the pulse sequence of this work determines the Maxwell coefficients as given in Equation 6.3 on a spoke-by-spoke basis. All coefficients are stored along with the raw data. In addition, the image position and orientation must be known to determine the coordinates of each pixel of the desired PC map.

Maxwell phase maps $\phi_{l,s}^M$ are calculated according to Equation 6.4 for each flow-encoding step l and each spoke s individually. Note that even though determined by the gradients responsible for k-space sampling, $\phi_{l,s}^M$ refer to phase maps in image space and thus have to be considered during image reconstruction. Using undersampled k-space data, a correction as a pre-processing step is not possible. The new and extended forward model of the mdMBR reads:

$$y_{j,l} = \frac{1}{N_s} \sum_{s}^{N_s} P_{l,s} \mathcal{F} \left\{ \rho \cdot \exp \left(i \, \phi_{l,s}^M + i \sum_{d=1}^{D} v_d S_{d,l} \right) \cdot c_j \right\} \tag{6.5}$$

Here, $y_{j,l}$ denotes the gridded raw data of the l^{th} encoding in the j^{th} receiver coil. While $\phi_{l,s}^M$ is predefined by the gradient waveforms and therefore known, the unknowns (ρ, v_d and c_j) remain the same (compare with the mdMBR without Maxwell correction: Equation 4.10). Using this formulation, the mdMBR performs a Maxwell correction implicitly and estimates clean velocity maps directly - free of concomitant field contributions. The derivative and adjoint derivative operators under Maxwell correction are listed in Chapter A.2 in the appendix.

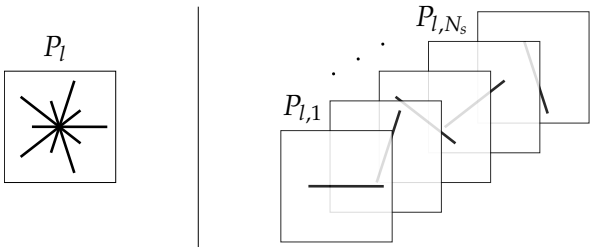

Figure 6.1: Sampling pattern for spoke-wise Maxwell correction. The pattern for the conventional model-based reconstruction (left) separates into individual patterns for the spoke-by-spoke Maxwell correction (right).

As depicted in Figure 6.1, the sampling pattern $P_{l,s}$ splits up into individual patterns to account for spoke-dependent Maxwell terms. Note that accordingly, the number of Fourier transformations increases by the number of spokes N_s implying an increased computational demand.
As a compromise, without additional Fourier transformations, a frame-wise correction can be performed as an alternative by using spoke-averaged Maxwell terms μ_l:

$$y_{j,l} = P_l \mathcal{F} \left\{ \rho \cdot \mu_l \cdot \exp \left(i \sum_{d=1}^{D} v_d S_{d,l} \right) \cdot c_j \right\}, \tag{6.6}$$

where the complex-valued μ_l is given by:

$$\mu_l = \frac{1}{N_s} \sum_{s}^{N_s} \exp \left(i \phi_{l,s}^M \right) \tag{6.7}$$

Note that μ_l can exhibit magnitude values smaller than one, accounting for signal loss due to phase cancelation introduced by concomitant fields.

In a first part, the concomitant field contributions for flow encoding in all three orthogonal directions were investigated and in particular its dependency on TE and VENC was studied. The image slice was orientated nearly sagittal as for measurements of the human aortic arch. Maxwell phase maps were calculated as described above and the maximal phase error was determined for different combinations of TE and VENC covering the parameter space relevant for RT PC MRI.
The second part addresses the novel correction technique which was validated experimentally. For that purpose, in vivo measurements were performed at the aorta representing the high-VENC regime with protocol parameters as in previous experiments (see Chapter 4.3.3). Model-based reconstructions of *os*3d and *bal*3d were conducted without correction as well as under frame-wise and spoke-wise Maxwell correction. Exemplary for the low-VENC regime, CSF flow was studied at the cervical spinal canal by means of *bal*2d flow. Detailed experimental parameters are summarized in Table 7.1 in Chapter 7.2.

6.3 RESULTS

Results I: Concomitant Magnetic Field Contributions

Figure 6.2 shows the phase offset maps based on *os*3d flow at the aortic arch for all spokes of the first frame. To represent the expected error in velocity maps, the maps are obtained by subtracting the Maxwell phase maps of the reference scan.

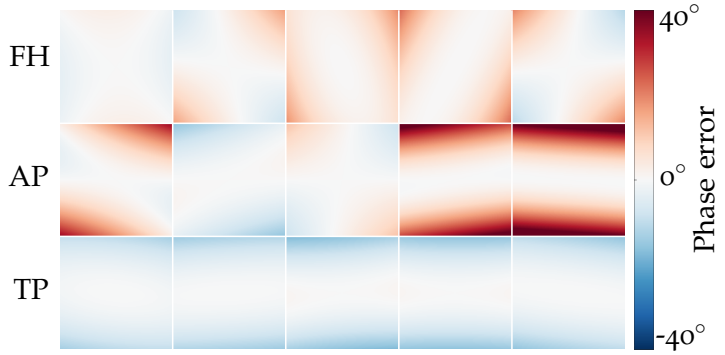

Figure 6.2: Phase error maps by concomitant magnetic fields for five individual spokes forming one frame. The uncropped FOV (oversampling of factor 2) is shown for feet-head (FH), anterior-posterior (AP) and through-plane (TP) velocity encoding.

The combination of sequence and protocol parameters for aortic imaging (VENC = 150 cm/s, TE = 2.12 ms) results in significant concomitant magnetic fields expressed by large phase errors. Following the theory of concomitant fields the errors increase with increasing distance from the iso-center (here coincides with image center). High phase values of up to 40° for individual spokes and large inter-spoke differences are observed.

The effect is most prominent in the AP encoding direction which corresponds to in-plane encoding nearly perpendicular to the B_0 direction. For the given example and a supine patient position, the imaging plane orientation comes close to a sagittal plane orientation (to capture the aortic arch) wherefore the FH encoding direction almost coincides with the B_0 direction and AP and TP direction orientate nearly perpendicularly to B_0. Errors in FH and TP direction are less pronounced as they describe flow encoding either in B_0 direction (FH) or slice-selection direction (TP), respectively. Both conditions are observed beneficial, however, not enough to prevent phase errors.

The influence of concomitant fields and the resulting phase errors were investigated in a more general context, i.e. for a wider range of sequence parameters. Figure 6.3 demonstrates the sensitivity of the maximal expected phase error towards TE and VENC. As both parameters influence each other, one was kept constant while changing the other. Additionally and more realistically, changes of VENC were followed by adaptations in TE such that in any case the shortest possible acquisition time is realized. The maximal phase errors were obtained by evaluating the Maxwell phase maps ϕ^M determined by the gradient waveforms of respective pulse sequences run on the MRI machine. Both, one-sided and balanced velocity encodings were considered.

The results show that the choice of TE and VENC has a tremendous effect on Maxwell phase errors. While for large VENC values and long TE the phase offsets vanish, decreasing the VENC or shortening TE results in a rapid increase with maximal phase errors exceeding 90°. The behavior is comparable for both velocity encoding techniques.
At this point it is important to note that the plotted values describe the maximal error as expected at the edges of images twice the FOV (oversampling of 2) and located in far distance to the iso-center. Even though the coil support is desired to be limited to the FOV, the maximal phase errors outside potentially contribute in form of streaking artifacts that reach into the actual FOV.
Inter-spoke differences of Maxwell phase errors are more pronounced in one-sided than in balanced velocity encoding as illustrated by shaded areas surrounding the spoke-average in Figure 6.3. This observation can be ascribed to the fact that the gradient design of balanced flow encoding is potentially more similar throughout different encoding steps than for the asymmetric one-sided approach.

As demonstrated by the results, the most intuitive way of avoiding concomitant magnetic fields is given by sufficiently increasing TE. This way, gradient amplitudes are lowered and Maxwell terms decrease accordingly. That approach, however, stands in contradiction to the general demands of PC MRI and especially to the demands of RT imaging which aims at keeping TE as short as possible. Also the choice of the VENC is non-negotiable. For a given application it is strictly linked to the maximal velocity of interest. Consequently, concomitant fields have to be corrected by means of the Maxwell correction.

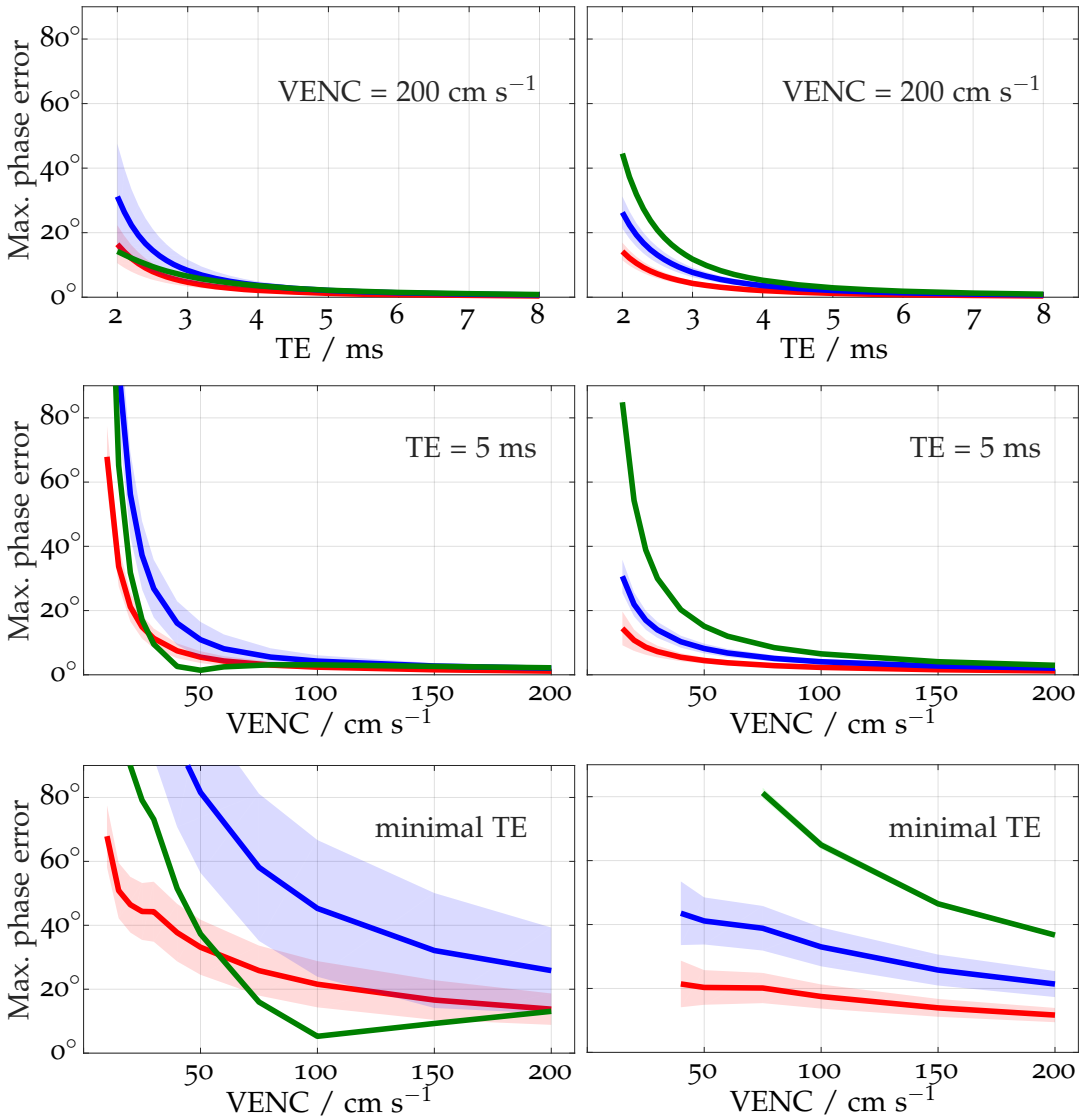

Figure 6.3: Maximal Maxwell phase error as function of TE and VENC. One-sided *(left)* and balanced 3d flow encoding *(right)* with colors indicating feet-head *(red)*, anterior-posterior *(blue)* and through-plane *(green)* velocity-encoding directions. Central lines show mean values and shaded areas the standard deviation over different spokes.

Results II: Maxwell Correction

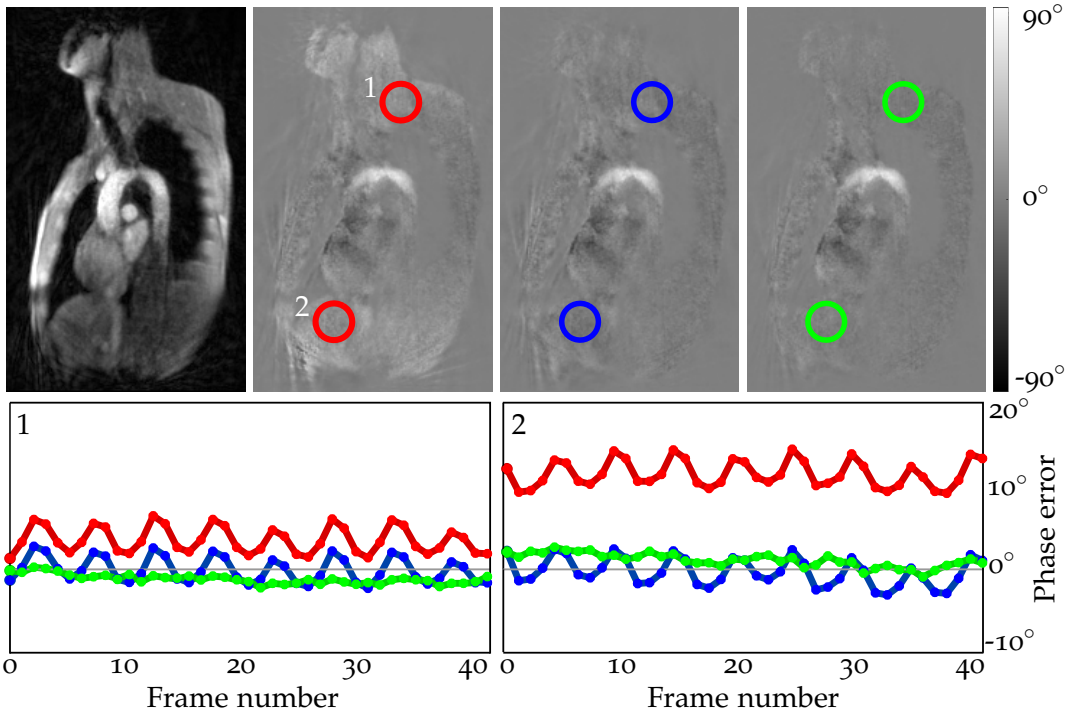

Figure 6.4: Maxwell corrections for the anterior-posterior (AP) encoding direction of *os*3d PC MRI at the aortic arch. *Top, from left to right:* magnitude image, velocity maps in AP direction without *(red)*, with frame-wise *(blue)* and spoke-wise Maxwell correction *(green)*. *Bottom:* ROI evaluation of static tissue in neck (1) and liver region (2).

Figure 6.4 demonstrates the performance of the novel Maxwell correction for an in vivo measurement acquired with the same acquisition parameters as used for Figure 6.2. PC maps in AP direction are shown without, after frame-wise, and after spoke-wise Maxwell correction as described in Equation 6.6 and 6.5, respectively. Visual inspection and ROI evaluations in the outer FOV reveal a strong influence of concomitant fields apparent via phase offset errors in areas of static tissue (liver and neck region) for the uncorrected data set.
The frame-wise correction reduces the phase errors insufficiently, as image artifacts and temporal oscillations of velocity values remain. The period of these oscillations coincides with the periodicity of the sampling pattern (number of turns $N_T = 5$). By means of the spoke-wise Maxwell correction phase errors and their temporal fluctuations are successfully corrected for. This approach best describes the underlying physics and for the given example significantly improves the image quality and accuracy of the velocity measurement.

For the TP-encoding direction a frame-wise correction was found to be sufficient which is reflected in similar phase errors for different spokes (Fig.6.2 and 6.3). This is a consequence of the fact that the amplitude of flow-encoding gradients in slice-selection direction (= TP) remains constant over different spokes.

The FH-encoding direction nearly coincides with the B_0 direction and thus reveals the lowest phase errors. In this case, as shown in Figure 6.5 little to no differences are observed in Maxwell-corrected reconstructions.

For balanced velocity encoding the velocity information and the Maxwell errors are entangled and therefore less intuitively distributed along the velocity components. As illustrated in the lower half of Figure 6.5, here, the TP encoding exhibits the largest errors for *bal*3d and benefits most from the Maxwell correction. The overall effect summarized in the speed image is comparable between one-sided and balanced velocity encoding.

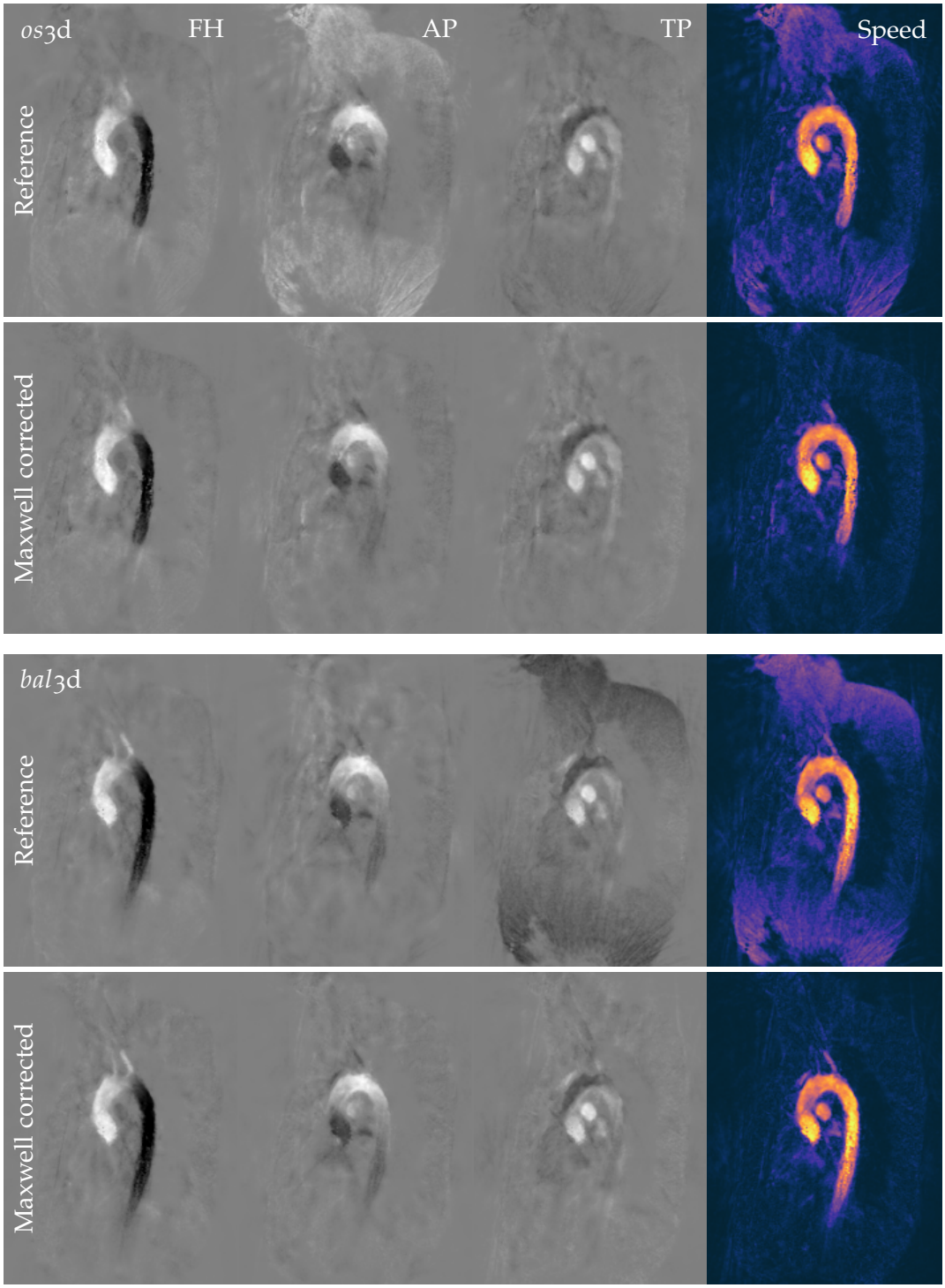

Figure 6.5: Spoke-wise Maxwell correction for one-sided *(upper half)* and balanced *(lower half)* 3d velocimetry at aorta. The uncorrected and Maxwell corrected velocity maps are shown in feet-head (FH), anterior-posterior (AP) and through-plane (TP) flow direction, as well as the corresponding speed images (root sum square).

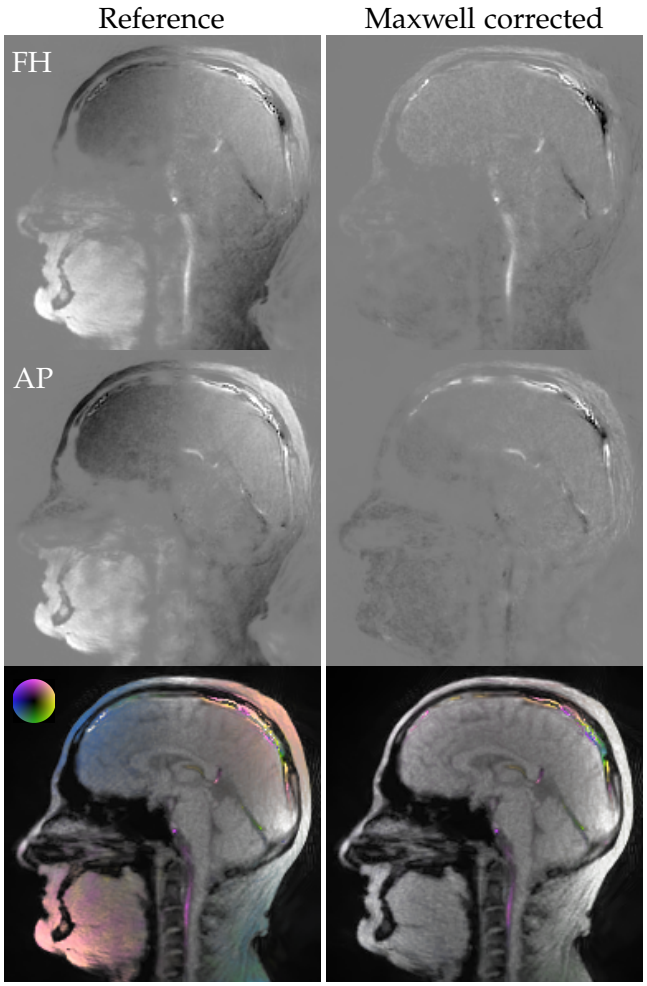

Figure 6.6: Spoke-wise Maxwell correction for CSF flow in cervical spinal canal. PC maps in feet-head (FH) and anterior-posterior (AP) direction, as well as color-coded in-plane flow maps overlayed onto magnitude images *(bottom)*. Artifacts in the superior sagittal sinus can be ascribed to phase wraps.

The necessity of Maxwell correction in the low-flow regime is demonstrated in Figure 6.6. CSF flow data was acquired with a VENC of 10 cm/s by means of *bal*2d flow. The image reconstructions are performed with and without spoke-wise Maxwell correction. Large phase offset errors of up to 76° (chin region) are prominent in both in-plane velocity components. The proposed Maxwell correction eliminates the phase offset artifacts.

The large gradient moments of 2d in-plane velocity measurements for low flow (VENC = 10 cm/s) render a Maxwell correction indispensable.

6.4 DISCUSSION

This work demonstrates the high sensitivity of multi-directional RT PC MRI to concomitant magnetic fields and presents a Maxwell correction technique that is applicable to the RT PC technique based on radial sampling.

Even though operating at high magnetic field strength ($B_0 = 3$ T) the image acquisition developed through out this thesis provokes significant Maxwell terms in the parameter range relevant for RT PC MRI. The reasons, why concomitant fields are higher than usually expected at 3 T, are found in different contributing factors:

- *High maximal gradients:* Modern MRI machines not only operate at higher field strength but commonly exhibit increased gradient amplitudes which are more decisively for Maxwell terms according to its proportionality to $\propto G^2/B_0$. The MRI system used in this work operates at 3 T and allows for maximal gradient amplitudes of 80 mT/m. In comparison to the values given in [15] (10 mT/m at 1.5 T), that alone corresponds to an increase of potential phase errors by a factor of 32.

- *Real-time imaging:* RT PC imaging aims at high spatio-temporal resolutions and therefore operates at the limit of possible sequence timings. The consequences include fast gradient switching and high gradient amplitudes at the upper limit. Both support the formation of high Maxwell terms. The high sensitivity towards short TE is demonstrated above.

- *Multi-directional flow encoding:* Previous RT PC methods [9, 11] are limited to through-plane flow and are almost exclusively applied to velocity directions that align along the B_0 field (as it usually coincides with the main vessel orientation). This condition is beneficial in a sense that lower Maxwell terms occur. The reason for that is a lower G_z dependency than for flow gradients in a transversal direction (G_x or G_y). With the introduction of flow-encoding in all three directions, and in particular measurements in x- and y- direction, Maxwell terms increase.

- *Low VENC values:* Measurements in the low-flow regime exhibit high gradient moments that result in high Maxwell terms. This relation and its high sensitivity in low VENC values are pointed out by this work's results (Figure 6.3).

All points contribute to significant concomitant magnetic fields rendering a Maxwell correction indispensable for multi-directional RT PC MRI.

The correction approaches proposed in this work, both frame-wise and spoke-wise, eliminate the undesired phase offset artifacts. Remaining temporal phase fluctuations, however, are only avoided by the spoke-wise approach which better describes the underlying physics. Unfortunately, this approach relies on an increased computational demand that scales with the number of spokes. In the current implementation and with 5 spokes per frame the reconstruction time approximately doubles.
The alternative frame-wise correction comes at low numerical costs and performs

sufficiently well, presuming that inter-spokes differences of Maxwell terms are small. The high sensitivity in sequence parameters, such as image orientation, FOV, TE and VENC, precludes a general statement on whether inter-spoke differences are small enough to apply the less expensive frame-wise approach. Therefore, the choice which correction option is preferable remains to be evaluated for a specific application with fixed parameters.

Future methodological investigations may focus on a correction strategy that operates on k-space segments instead of individual spokes. This idea can be considered a compromise between the frame-wise and the expensive spoke-wise approach at potentially lower computational costs.

7

APPLICATION EXAMPLES

This chapter presents preliminary results obtained by the novel RT flow technology and potential application fields that can broadly be classified according to the flowing medium. Starting with a self-developed in vitro experiment, the flow of *water* downstream of a cylindrical obstacle is quantified and the creation of a Kármán vortex street is observed. More clinically orientated, in vivo examples divide into measurements of *CSF* flow in the spinal canal and measurements of *blood* flow in the cardiovascular system.

7.1 WATER: KÁRMÁN VORTEX STREET

Previous flow phantoms only provided *laminar* and more particularly *stationary* flow. The latter is predictable and perfectly suited for the validation of respective velocity quantification techniques as presented in previous chapters. Defined by vanishing time derivates, however, stationary flow exhibits no need for high temporal resolution which is one of the key features of the novel imaging technique.
While laminar flow is located at low Reynolds numbers, its opposite, *turbulence*, occurs at high Reynolds numbers and is generally not accessible by means of PC MRI. Limited spatial resolutions of MRI and intra-voxel dephasing due to kinetic energy dissipation from large to smaller scales lead to significant signal decays up to complete signal voids for turbulent flow patterns. Therefore, neither the stationary nor the turbulent-flow regime are suitable candidates to illustrate the potential of the new flow imaging technique.
To test and demonstrate the performance of multi-directional RT PC MRI in vitro a new flow phantom is designed that operates in the intermediate regime of Reynolds numbers ($Re \approx 500$). In-between the laminar and turbulent-flow regime, the well-known phenomenon of Kármán vortex shedding is observed downstream of cylindrical obstacles. This repeating pattern of swirling vortices promises to be a suited candidate for testing the novel multi-directional PC MRI technique as it provides non-trivial and dynamic flow structures.

The experimental realization of the Kármán vortex street inside the MRI machine was based on a plastic flow chamber of 15 cm width, a length of 70 cm and 5 cm height. Inside this chamber inflowing water pumped at 9.5 L/min was laminarized by means of a foam and a customized tubing systems which consists of nearly 800 plastic straws. Each straw has an inner diameter of 3 mm and 20 cm length. This setup was used to prevent the occurrence of transversal velocity components. Figure 7.1 demonstrates its performance and shows the flow behavior at the individual stages of experimental phantom development.

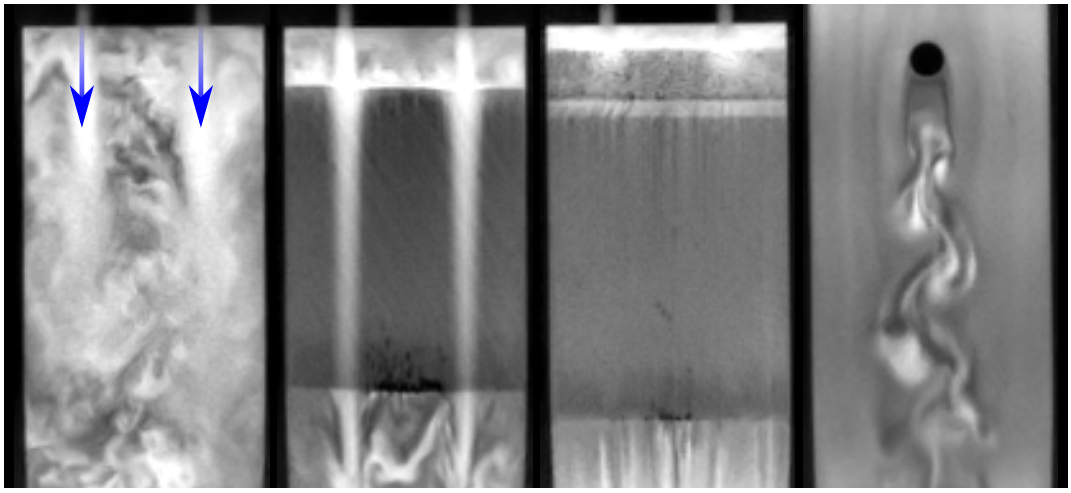

Figure 7.1: Phantom setup for Kármán vortex street. *From left to right:* Empty flow chamber with double inlet (*blue arrows*) resulting in turbulent flow; nearly 800 straws to laminarize the flow; foam upstream of straws for homogenous flow distribution; cylinder downstream of straws and Kármán vortex street in its wake.

While turbulent flow is apparent for an empty box, the flow downstream of the foam and straw setup is observed to be laminar. As a result, in the wake of a plastic cylinder (diameter: 2 cm) placed in the laminar flow, a Kármán vortex street builds up. Illustrated in Figure 7.2 the vortex street is distinctly visible by anatomical T_1-weighted RT MRI. Signal decay due to dephasing and signal increases due to inflow effects result in high image contrasts that enable a qualitative visualization of the vortex flow pattern.

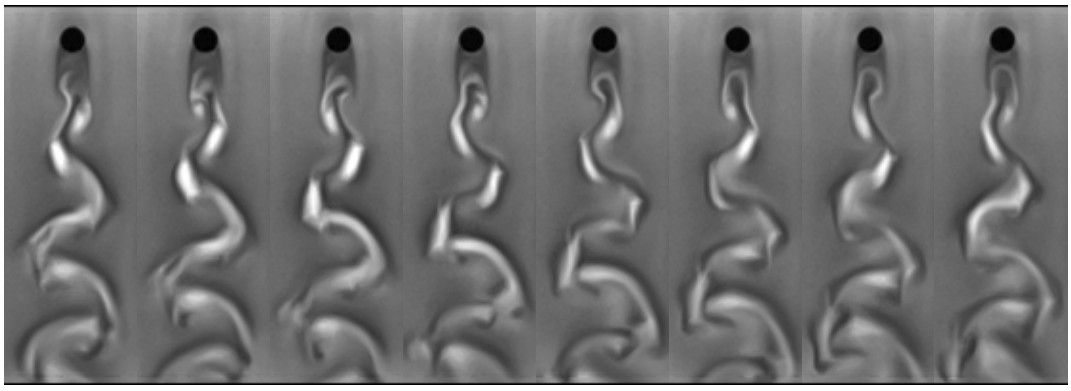

Figure 7.2: Kármán vortex street by RT MRI. Every tenth frame of a continuous image time series is shown.

Quantitative results were obtained by means of the 2d in-plane flow technique. Using a VENC of 10 cm/s, balanced velocity encoding, 5 spokes per encoding step, and TE/TR of 4.51/5.55 ms a temporal resolution of 83 ms was achieved. The FOV of 256 mm and matrix size of 192 result in pixel sizes of 1.3×1.3 mm^2 with a slice thickness of 6 mm. A flip angle of 10° was used for all PC experiments of this

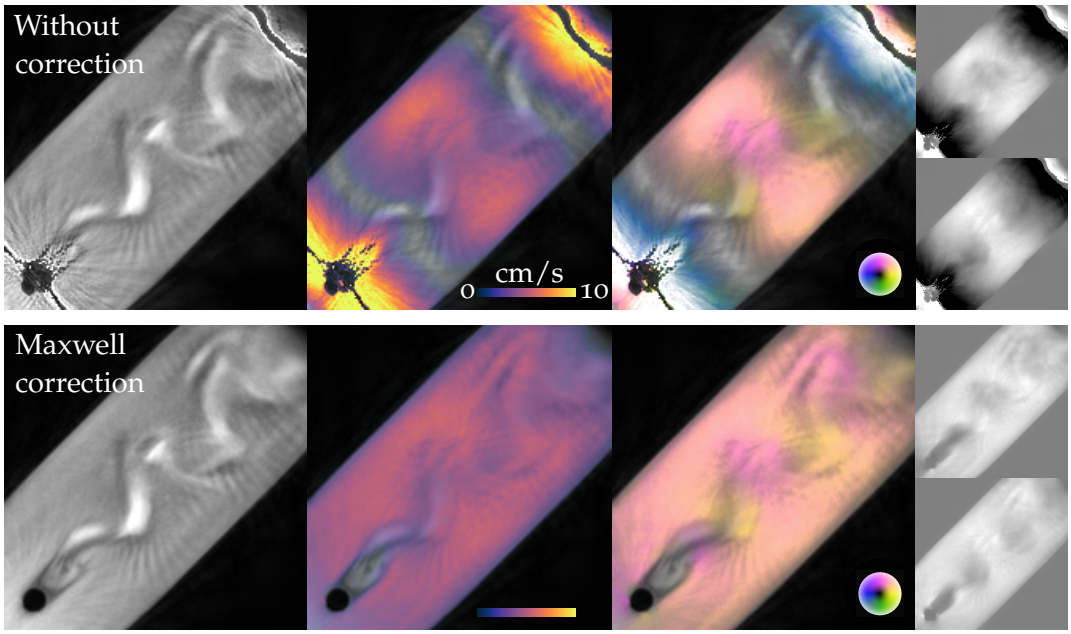

Figure 7.3: In-plane flow MRI of Kármán vortex street with and without Maxwell correction. *From left to right:* Magnitude, speed, in-plane flow map and the two underlying velocity maps.

work. The pump operated constantly at a flow rate of 9.5 L/min which resulted in an average velocity of $v_{avg} = 2.1$ cm/s determined by the physical dimensions of the flow chamber (cross-section $A = 75$ cm^2). Given the flow velocity and the dimensions of the cylinder, a Reynolds number of $Re \approx 500$ is estimated.
The results presented in Figure 7.3 underline the absolute need for a Maxwell correction. The experiments rely on a large FOV and a very low VENC which introduces strong concomitant magnetic fields. Phase wraps and severe image artifacts are observed in the outer part of the PC maps indicating phase errors that exceed 180°. Reasonable velocity maps are obtained by applying the spoke-wise Maxwell correction during image reconstruction as described in Chapter 6.

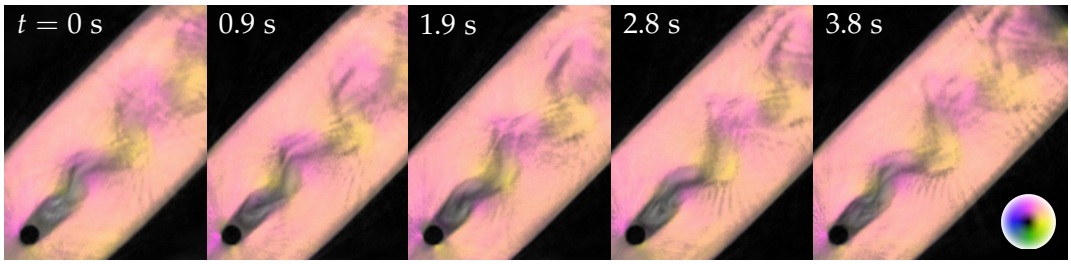

Figure 7.4: 2d in-plane flow of Kármán vortex street. The in-plane flow direction is shown for each quarter of a full period. Vortex shedding is indicated by periodic changes of pink and yellow.

Figure 7.4 shows in-plane flow images at selected time points taken from a continuous image time series with 36 fps. The vortex shedding is apparent by periodic

changes in flow direction downstream of the cylinder. These changes are expressed by color transitions of yellow *(horizontal flow)* and pink *(vertical flow)* and reveal a periodicity of $T = 3.79$ s obtained by sinusoidal fitting in time.
For cylindrical objects the frequency f of vortex shedding is linked to the flow velocity v by the so called Strouhal number $Sr = 0.2$ [63] and the diameter of $d = 2$ cm:

$$f = \frac{1}{T} = \frac{Sr \cdot v}{d} \qquad \Rightarrow \qquad v = \frac{d}{Sr \cdot T} = \frac{2 \text{ cm}}{0.2 \cdot 3.79 \text{ s}} = 2.6 \text{ cm/s} \tag{7.1}$$

This rough estimate of flow velocity is close to the average velocity $v_{avg} = 2.1$ cm/s. Actual flow velocities obtained by PC ROI evaluations left and right of the vortex street reveal a maximum of 5 cm/s and a lower speed of around 3 cm/s in the cylinder's wake. These values agree to the theoretically derived average velocity, as flow velocities in the center of the chamber are significantly higher ($v_{max} = 2 \cdot v_{avg}$ for laminar pipe flow).
The mismatch towards the flow velocity derived via Strouhal number might be explained by non-ideal flow conditions such as boundary effects of the spatially limited flow chamber, imperfect laminar flow and the occurrence of through-plane flow, rendering the flow phenomenon three- and not two-dimensional and consequently more complex. For that reason Equation 7.1 loses applicability for the given experimental setup and only allows a rough estimate.
The velocity values smaller than half of the VENC are represented with limited detail. The complex flow structure is better represented by the qualitative magnitude images. The temporal resolution of the applied PC MRI method, however, is more than sufficient considering the rather slow flow phenomenon.
The experiment is based on very low velocities that are difficult to capture as the VENC of 10 cm/s describes the lower limit of practical PC imaging. Employing the current electrical water pump with limited performance, higher velocities are out of reach. The use of too high velocities, however, runs the risk of destroying the harmonic vortices creation and instead introducing chaotic turbulence. Nevertheless, future experiments might benefit from higher pump rates resulting in higher velocities, more detailed PC maps and increased vortex shedding frequencies. Given that, the experimental setup can be considered a potentially useful candidate for future protocol optimization of multi-directional PC flow MRI in the low-VENC regime.

7.2 CEREBROSPINAL FLUID: CERVICAL SPINAL CANAL

An evolving application field of PC MRI, and of RT imaging in particular, is the quantification of CSF flow. At the current stage, the physiological functions and dynamics of CSF as well as their pathological disturbances are not fully understood and subject of ongoing research [64, 65, 66] .
Traditionally, CSF dynamics are investigated using ECG synchronized acquisitions which intrinsically highlight the cardiac dependency. Recently, respiration and in particular the inspiration has been identified as the main driver for CSF flow by means of RT MRI [67]. The continuous RT imaging allows observations of aperiodic dynamics or dynamics that are modulated by different frequencies. For CSF these comprise simultaneous influences of high-frequency cardiac action and lower-frequency respiratory motion.
The quantitative assessment of CSF flow via uni-directional RT PC MRI revealed an upward movement of CSF during deep inspiration [39]. This finding contradicts the common believe of a steady downwards flow from the head along the spinal canal. Follow-up studies based on RT PC MRI focused on CSF flow at different positions along the spinal canal [40] and on the influence of breathing conditions (thoracic or abdominal respiration) [41]. As mentioned in Chapter 3, the latter study exploited the minTE velocity encoding strategy implemented within the scope of this thesis. While the minTE approach significantly improved the uni-directional flow measurements at low VENC values, the CSF measurements so far suffered from restrictions on image orientation. As the 1d through-plane flow technique was limited to velocities along a certain direction, only transversal imaging slices perpendicular to the spinal canal were acquired and a simultaneous coverage of multiple layers along the spinal canal precluded. Furthermore, the acquisition of respiration navigators such as mouth or chest movements were hindered, limiting a retrospective respiration control. The novel multi-directional RT PC MRI technique promises to overcome these restrictions.

This work presents preliminary results of exploiting the novel in-plane flow sensitivity for CSF flow measurements. Balanced 2d velocity encoding was applied in the cervical spinal canal using a sagittal slice orientation. The healthy subject was asked to perform multiple deep breaths while inhaling through the mouth and exhaling through the nose. In this way, the respiration state can be assessed retrospectively in the images by means of open or closed lips and no breathing protocol is required. Detailed experimental MRI parameters are listed in Table 7.1. TE and TR and thus the temporal footprint are significantly longer than for heart measurements as the lowest practical VENC value is used for slow CSF measurements.

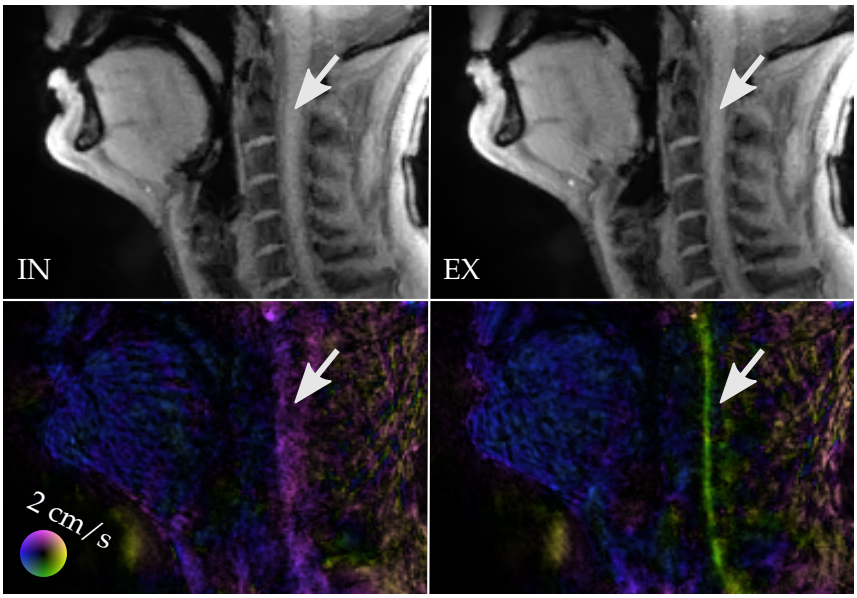

Figure 7.5: CSF in-plane flow in the cervical spinal canal. CSF flows upwards (cranial) during forced inspiration (IN) and downwards (caudal) for expiration (EX) as indicated by color coding.

PARAMETER	2D FLOW
VENC / cm s^{-1}	10
Field-of-view / mm^2	212 x 212
Resolution / mm^2	1.1 x 1.1
Slice thickness / mm	6.0
TE / ms	4.25
TR / ms	5.29
Bandwidth / Hz $pixel^{-1}$	815
Flip angle / °	10
Number of flow encodings	3
Spokes per encoding	9
Number of turns	5
Tilting factor TF	0.2
Temporal footprint / ms	143
Frame rate (SVE) / fps	21

Table 7.1: Acquisition parameters for 2d velocimetry in the cervical spinal canal.

Figure 7.5 shows the in-plane velocity field of CSF flow for in- and expiration. Both breathing states are distinctly identified by different lip and velum positions in the magnitude images. The slow CSF flow is detectable but offers limited SNR as the peak velocities of 2 cm/s only represent one fifth of the VENC value. Nevertheless, the flow direction is well defined and clearly evident by color coding. The results confirm previous findings and show an upward movement of CSF for inspiration and caudal flow for expiration.
The technique enables observation and quantification of in vivo CSF flow simultaneously on multiple levels along the spinal canal and thus is a potentially valuable tool for future studies on CSF dynamics and its perturbations leading to conditions like syringomyelia and hydrocephalus. However, further protocol optimization and a validation on a larger number of healthy subjects are warranted.

7.3 BLOOD: AORTIC ARCH

The predominant clinical application of PC MRI is the determination of blood flow velocities for the assessment of cardiovascular systems. Particularly the aorta is of high interest as it represents the heart's outlet and the central vessel for the oxygen-rich blood supply. It exhibits the highest flow velocities in the human body as well as the most abrupt changes in velocities which thus require the highest temporal resolutions for their detection.
This chapter presents the results of multi-directional RT PC MRI applied at the aortic arch by means of the novel imaging technique described in Chapter 4 and 5. All three velocity directions were acquired (3d flow) and reconstructed jointly by the iterative image reconstruction developed for velocity vectors (mdMBR). A second measurement relied on 2d flow, limited to the acquisition of both in-plane flow components. Furthermore, the applicability to other slice orientations is demonstrated by 3d flow results inside the human heart in a 3-chamber view. All relevant acquisition parameters are listed in Table 7.2.

PARAMETER	2D FLOW	3D FLOW
VENC / cm s^{-1}	150	150
Field-of-view / mm^2	320 x 320	320 x 320
Resolution / mm^2	1.8 x 1.8	1.8 x 1.8
Slice thickness / mm	6.0	6.0
TE / ms	2.05	2.12
TR / ms	3.03	3.12
Bandwidth / Hz $pixel^{-1}$	905	880
Flip angle / °	10	10
Number of flow encodings	3	4
Spokes per encoding	5	5
Number of turns	5	5
Tilting factor TF	0.2	0.2
Temporal footprint / ms	45	62
Frame rate (SVE) / fps	66	64

Table 7.2: Acquisition parameters for 2d and 3d flow at the aortic arch and the heart.

The in vivo measurements were performed without any physiological gating which is conventionally required for cardiovascular MRI. In particular, no ECG- or respiratory gating and no breath holds are needed. Instead, the continuous image acquisition runs under maximum freedom of patient's motion, e.g. free breathing. The total scan time is free of choice and is set to 10 s to cover around ten individual heart beats. Principally, even the acquisition of a single heart beat is possible.
The image reconstruction was performed offline. Under the current single GPU im-

plementation, reconstruction times demand roughly 6 seconds per frame, including the spoke-wise Maxwell correction and a SFD filter strength of $\sigma = 2$ pixel. The output frame rate is increased by means of the SVE reconstruction strategy.

Figure 7.6 shows the blood speed in the aortic arch for 60 successive frames nearly covering one second. Both, the diastolic and systolic heart phase are represented and distinctly recognizable by the visualization strategy described in Chapter 4.4. The starting and ending frames show the process of ventricle filling in the early-diastolic phase. Smaller velocities of around 50 cm/s are observed in the left atrium and left ventricle. The flow vanishes for the late-diastolic phase (full heart chambers) whereas the subsequent systolic phase is characterized by heart contraction and peak flow in the pulmonary artery and the aorta. The onset of strong blood flow is evident in the second half of the illustrated frames and the velocity propagation along the aortic arch is well documented.
The speed images do not visualize information on flow direction which is instead included in Figure 7.7 illustrating the systolic frames component-wise.
The results are impaired by minor undersampling artifacts and noise-like patterns in the lower part of the descending aorta. Two contributing reasons limited the MRI signal strength in that region and translate into compromised PC values. These are i) a limited receiver coil support and ii) a declining inflow effect. The latter usually describes MR signal increases because of unsaturated spins flowing into the imaging slice. As the spins travel *inside* the imaging slice, the MR signal strength (longitudinal magnetization) declines. The resulting reduced inflow effect constitutes a general disadvantage of cross-sectional in-plane flow imaging in comparison to through-plane flow and leads to inferior SNR.
Still, the results show an exceptional combination of spatio-temporal resolution and image quality for full 3d quantitative velocity information of a single individual heartbeat.

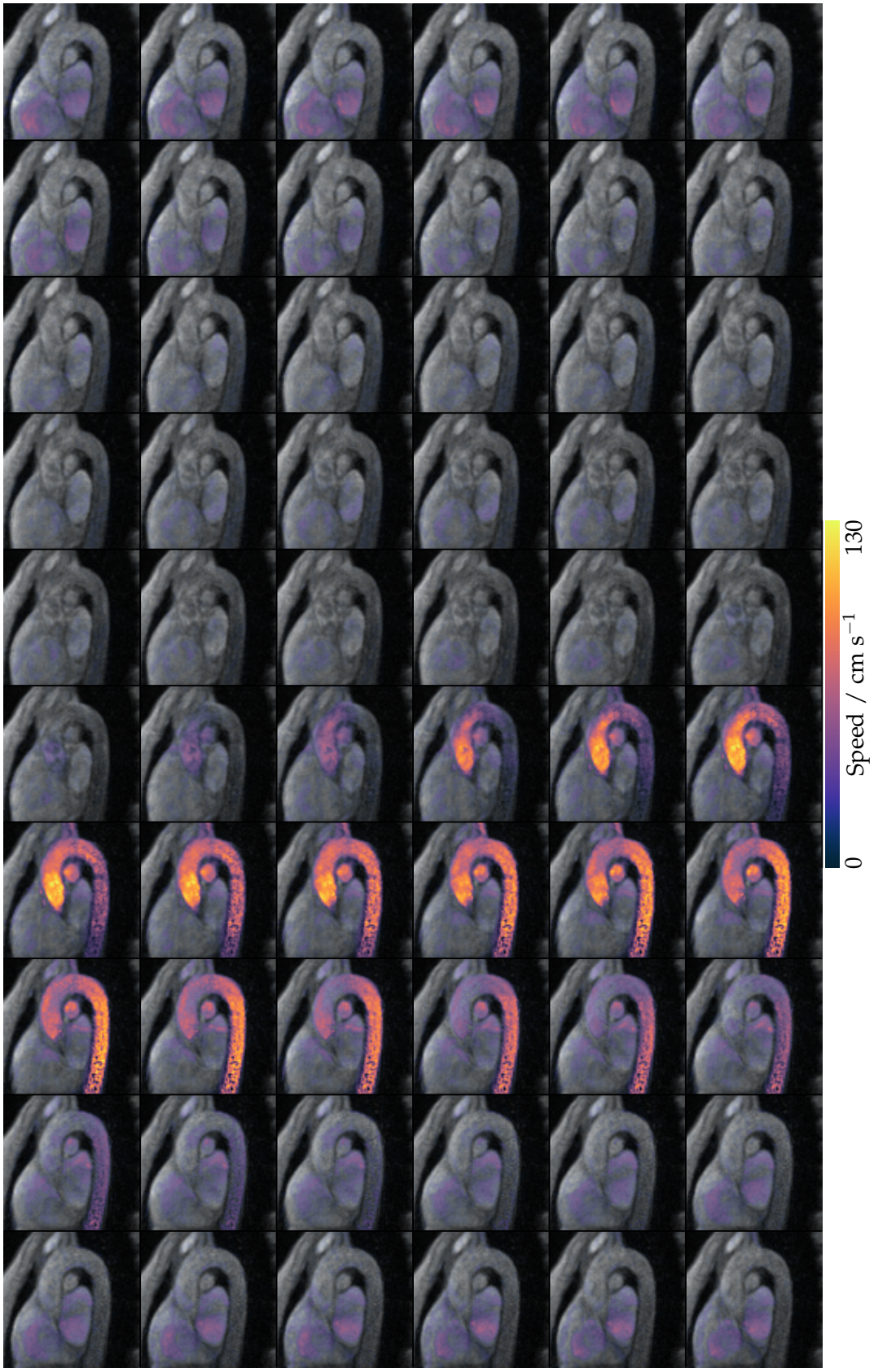

Figure 7.6: Blood speed in aortic arch for single heart beat. The quantitative 3d flow data is acquired at $1.8 \times 1.8 \times 6$ mm^3 spatial resolution and displayed at 64 fps.

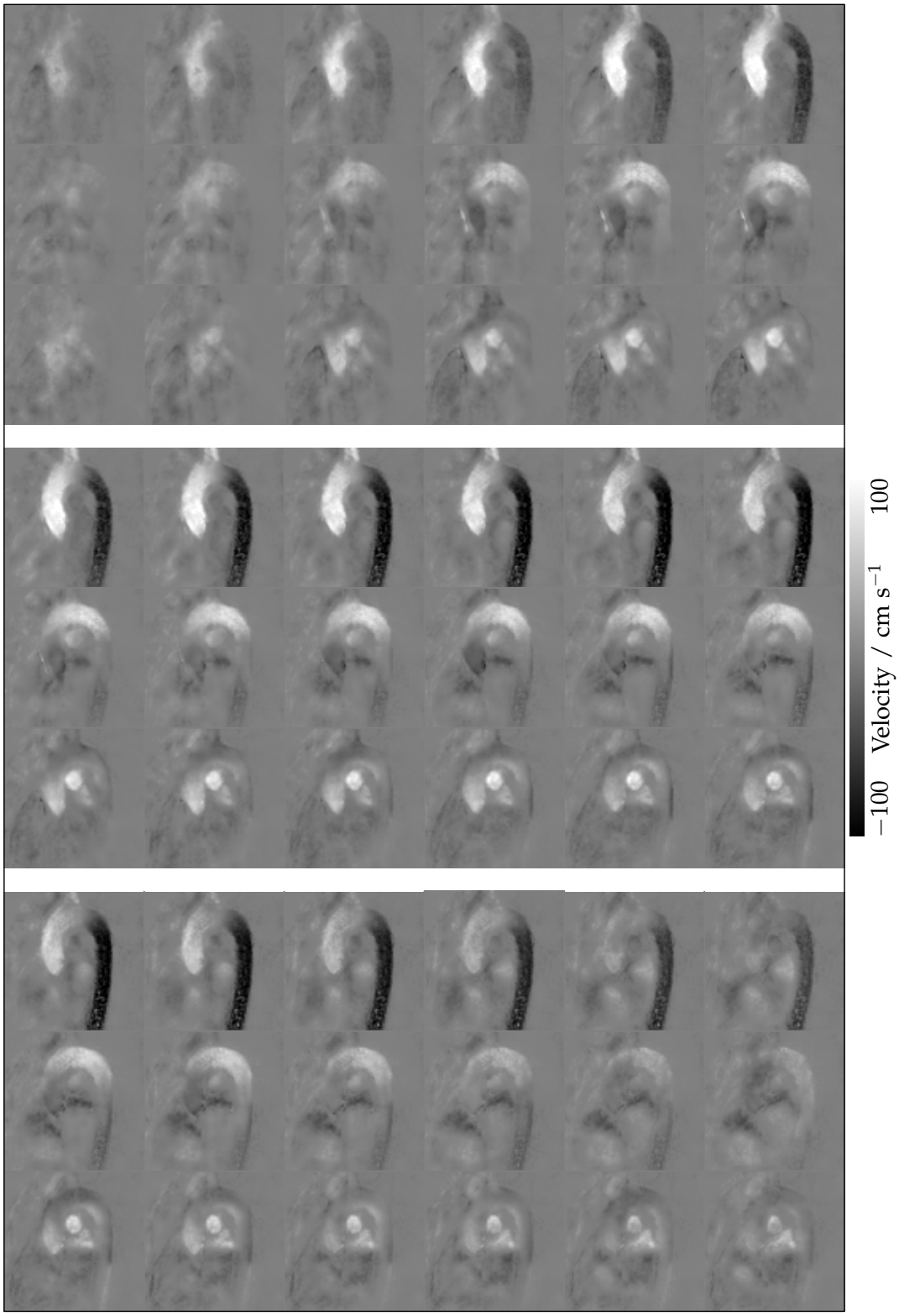

Figure 7.7: Velocity maps in all three flow directions. The systolic frames were taken from a continuous time series (Fig. 7.6) and provide full 3d velocity information for a single independent heart beat.

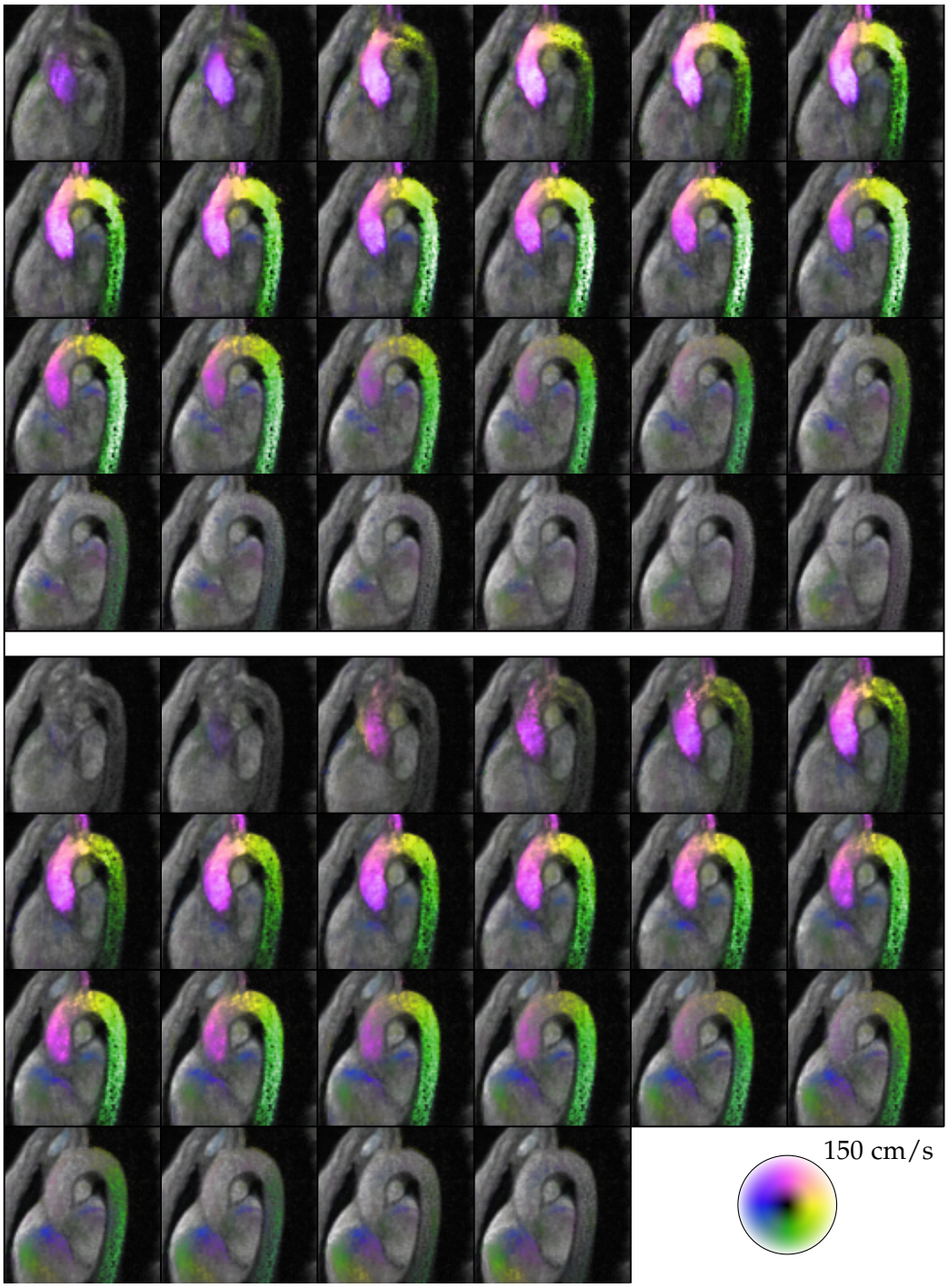

Figure 7.8: In-plane flow in aortic arch during systolic phase for two successive heart beats. The quantitative 2d flow data was acquired at $1.8 \times 1.8 \times 6$ mm^3 spatial resolution and displayed at 66 fps.

Figure 7.8 depicts the results of the 2d flow measurement for two successive systolic phases. The in-plane flow components are quantified and the flow direction is included by color coding. The difference towards 3d flow is evident in the pulmonary artery which, for the given slice orientation, mainly carries through-plane flow. The results show exceptional spatio-temporal resolutions and good image qualities considering the substantial degree of undersampling.
Two successive heart beats are illustrated and demonstrate beat-to-beat variations apparent by differing maximum speeds during systole (around 120 and 100 cm/s). Figure 7.9 shows the corresponding in-plane speed over the total scan time obtained by ROI evaluations in the ascending aorta.

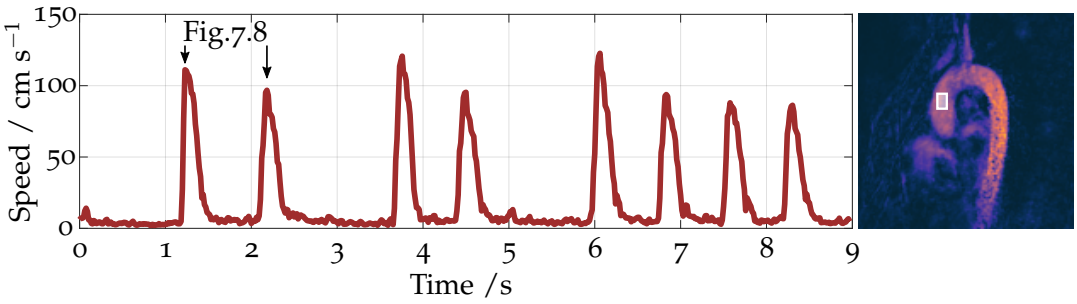

Figure 7.9: Aortic in-plane speed over time. The time curve was obtained by ROI evaluation in the ascending aorta as illustrated on the right. The RT technique operates reliably despite minor arrhythmia and allows to assess beat-to-beat variations.

The results reveal irregular heart beats indicating moderate and asymptomatic arrhythmia of the healthy volunteer. Extended diastoles are observed to be followed by compensating systoles with increased blood velocities in the cardiac output. The given in vivo example underlines one of the key advantages of the novel PC MRI technique, which does not rely on any periodicity of the investigated object and thus allows to assess beat-to-beat variations of cardiac functions. For the same reason, the method stably operates under free breathing.

Figure 7.10 shows a fragment out of a continuous image time series with different slice orientation and focus on the heart. The preliminary results confirm that the novel imaging technique is applicable for blood flow measurements aside from the aortic arch. In this imaging orientation, the outflow of blood from the left ventricle through the aortic valve into the aorta is well documented, as well as the subsequent inflow and ventricle filling via left atrium and mitral valve. The results serve as a proof of principle, while further protocol optimization and studies on a larger number of healthy subjects are warranted.

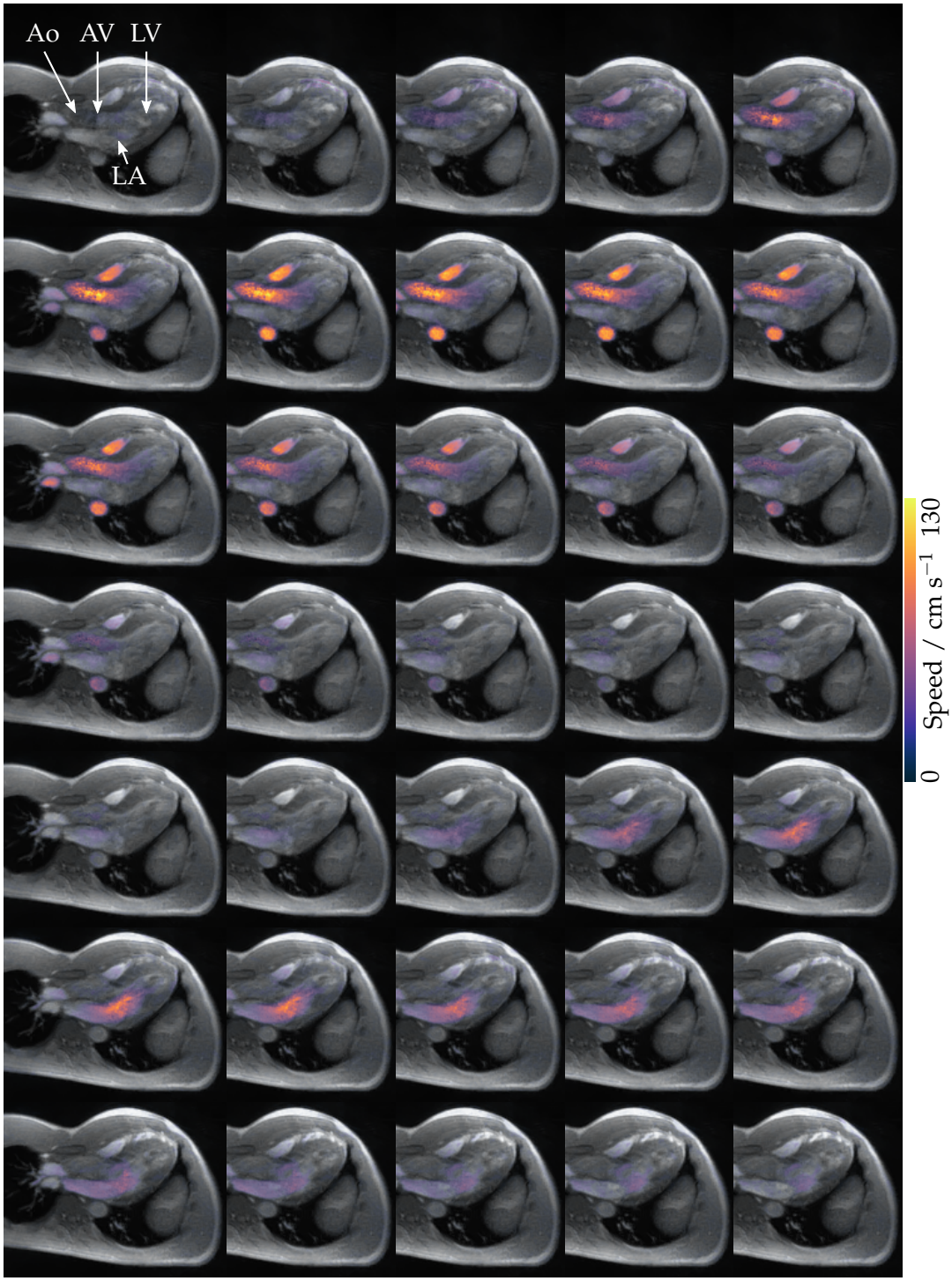

Figure 7.10: Blood speed in left ventricle (LV) for single heart beat by 3-chamber view. The quantitative 3d flow data was acquired at $1.8 \times 1.8 \times 6$ mm^3 spatial resolution and displayed at 64 fps. Ao: Aorta, AV: Aortic valve, and LA: Left atrium.

8

SUMMARY AND OUTLOOK

After their "engagement" in 2012 [9], this work completes the "marriage" of phase-contrast and real-time MRI based on undersampled radial FLASH and non-linear iterative image reconstruction.

For the first time, cross-sectional PC MRI with velocity quantification in all three physical directions is achieved at spatio-temporal resolutions that are suited for cardiac imaging and in accordance with the specifications on RT MRI [68]. Beyond the extension of a previous approach to more velocity dimensions, several improvements of the quantitative imaging technique are presented.
The uni-directional method is revised and upgraded by the time-efficient minTE velocity encoding which improves the flow measurements especially in the low-velocity regime. Flow-encoding or -compensating gradients are relaxed to reduce potential peripheral nerve simulation. The RT method in general benefits from modifications of the post-processing median filter which robustly treats complex data. Furthermore, a Maxwell correction strategy for uni- and multi-directional radial PC MRI was developed that operates in combination with the model-based image reconstruction and increases the accuracy of velocity maps by preventing significant phase offset errors.
Different methodological steps for the development of a multi-directional PC MRI method are presented and discussed. The best results are achieved using a time-efficient pulse sequence design in combination with a model-based image reconstruction which jointly estimates image content, receiver coil profiles and all velocity vector components.
The key principle and corresponding benefit of this reconstruction is the use of redundancy in multiple flow-encoding steps. Specific aspects exploit i) a balanced velocity encoding that allows short sequence timings and homogeneous phase reference estimates, ii) complementary radial k-space sampling which improves the spatial acuity of magnitude images, and iii) velocity denoising by smoothing of flow directions which improves SNR and eliminates phase wraps artifacts.
In addition to these assets mainly concerning the spatial domain, the temporal domain was greatly improved by sharing velocity encodings. The approach increases the frame rate of dynamic PC imaging up to four times and thus upgrades its effective temporal resolution. At the same time, less Newton iterations are required for the reconstruction of a single frame.
Preliminary in vivo results include cardiac flow imaging with velocity quantification in all directions at less than 2×2 mm^2 pixel-size and more than 60 fps.

The new MRI technique presented here allows maximal flexibility for PC based cross-sectional velocimetry. The framework provides uni-directional velocity measurements in any direction (1d flow) in combination with other directions (2d or 3d

flow) and arbitrary slice orientation. Robust imaging is performed without prospective or retrospective gating and thus without constraints on minimal acquisition times. Moreover, beat-to-beat variations are accessible which, for example, allows studies on patients with arrhythmias and during free breathing. In a more general context, the technique allows access to the immediate physiological flow response to respiratory maneuvers or physical exercises as potential novel diagnostic stress tests.

Unlike common 4D flow MRI methods [59, 69, 60] that rely on volumetric imaging (3D) and scan times of minutes, the PC method developed in this thesis is significantly faster. However, it is limited to cross-sectional imaging and therefore provides no three-dimensional visualization of complex flow phenomena. Without access to flow areas of in-plane velocity components the evaluation of flow rates (in ml/s) is precluded. Nevertheless, rapid volume coverage may be accomplished in future studies by sequential multi-slice acquisitions using automatic slice propagation [70].

Results acquired in the challenging low-flow regime underline the method's versatility. An in vitro experiment showing a Kármán vortex street and preliminary results of a CSF measurement in the spinal canal especially profited from the novel Maxwell correction technique. While these preliminary results prove the feasibility of multi-directional RT PC MRI aside from haemodynamics, further protocol optimization and clinical evaluations are warranted.

Future methodological investigations may focus on a L_1-norm regularization (instead of L_2) with promising denoising potential, or on more elaborated vector denoising strategies, e.g. based on total variation (TV) [71] and its vectorial extensions [72, 54]. Moreover, the incorporation of TV as a regularizer in the iterative image reconstruciton algorithm is reported beneficial for anatomical imaging [24, 73] and might be exploited for PC velocity maps. Here, a coupling between velocity components is desired, as pointed out in this work's investigations using SFD.

At this stage, the most limiting factor is a computationally intensive offline reconstruction. The lack of sufficient computational speed leads to reconstruction times of several minutes for 3d flow data sets acquired within seconds (aorta: 6 min for 1 s movie). Further progress is foreseeable by pronounced parallelization of the reconstruction algorithm and its implementation on a multi-GPU system already connected to the commercial MRI machine. It currently offers reconstruction speeds of up to 50 fps for anatomical RT MRI and online model-based reconstructions and display of uni-directional PC acquisitions. The extra computational load imposed by the spoke-wise Maxwell correction can be avoided by the less reliable frame-wise approach or may in future be reduced by a lower-cost correction that operates on k-space segments.
Either way, the high computational demand and the associated latency only represent a practical limitation and no conceptual conflict for the realization of true or interactive RT imaging (with minimal latency) as the reconstruction of a single frame only depends on its predecessor. Unlike reconstructions of retrospective nature [74, 61, 75] the developed novel imaging technique supports direct online

reconstruction and display, presuming the computational speed to be sufficient. As soon as the latency is minimized, flexible velocimetry with interactive slice positioning as hitherto only achieved by ultrasound technologies, can become reality.

A

APPENDIX

A.1 DERIVATION OF TIME-EFFICIENT GRADIENT DESIGN

The merge of flow-encoding and imaging gradients for TE minimization is described in [32] for Cartesian imaging conditions. Instead of an independent bipolar gradient two extra gradient lobes are used for velocity encoding in read direction. As illustrated in Figure A.1 the "inner" and "outer" gradient lobes are located directly in front of the read gradient. This work builds up on the work of Bernstein et al. [32] and presents the gradient design for *radial* imaging with rotating read direction, yet *Cartesian* velocity encoding.

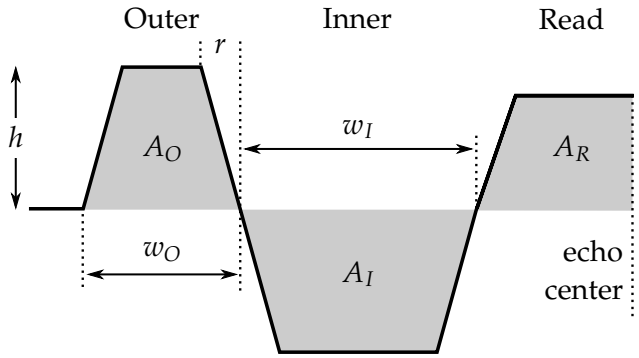

Figure A.1: Gradient lobes for merged flow-encoding and read gradients. Area A, width w, maximal gradient strength h and minimal ramp time r.

Given the read gradient, the inner and outer gradient lobes are designed such that they i) null the overall zeroth gradient moment (0^{th}GM = signed area under curve) and ii) compensate for the first gradient moment (1^{st}GM) of the read gradient M_R, while generating a desired first gradient moment M_V responsible for velocity encoding:

$$0^{th}\text{GM}: \qquad A_O + A_I + A_R = 0 \tag{A.1}$$

$$1^{st}\text{GM}: \qquad A_O\left(w_I + \frac{w_O}{2}\right) + A_I\frac{w_I}{2} - M_R = M_V \tag{A.2}$$

Here, A_O, A_I and A_R represent the 0^{th}GMs and w_O and w_I the gradient's width or duration as illustrated in Figure A.1. Under the constraints of a maximal gradient amplitude h and minimal ramp time r one can solve for A_O:

$$A_O = -\frac{hr}{2} + \frac{1}{2}\sqrt{(hr)^2 + 2\left(hrA_R + A_R^2 + 2h(M_R + M_V)\right)}$$

With rotating read gradients for radial sampling, the gradient preparation has to consider M_R and M_V to point in the same or opposing directions. For that reason, the minimal timing of both gradient lobes is initially calculated using $|M_V|$ instead of M_V:

$$A_O^{max} = -\frac{hr}{2} + \frac{1}{2}\sqrt{(hr)^2 + 2\left(hrA_R + A_R^2 + 2h(M_R + |M_V|)\right)}$$
$$A_I^{max} = -A_O^{max} - A_R$$

These maximal 0^{th}GMs then determine the minimal gradient duration and thus minimal sequence timing.

$$w_O = \left\lceil \frac{A_O^{max}}{h} \right\rceil + r \qquad\qquad w_I = \left\lceil \frac{A_I^{max}}{h} \right\rceil + r$$

Here, the widths of both gradient lobes are rounded up to fit the gradient raster time as demanded by the sequence programming environment. Both values stay constant for all read directions, i.e. over all projection angles φ, while the corresponding gradient amplitudes, G_I and G_O, are adapted for each φ. Initialized for the zeroth spoke ($\varphi = 0$), the gradient amplitudes follow:

$$G_O = \frac{A_O}{w_O - r} \qquad\qquad G_I = \frac{A_I}{w_I - r}$$

Using Equations A.1 and A.2, one can show that:

$$G_O = \frac{2(M_R + M_V) + A_R w_I}{(w_O + w_I)(w_O - r)} \qquad G_I = \frac{2(M_R + M_V) + A_R(2w_I + w_O)}{(w_O + w_I)(w_I - r)}$$

When rotating the read direction ($\varphi \neq 0$), the amplitude of the read gradient G_R is projected on the x-axis by $\cos(\varphi)$ and thus M_R and A_R are modulated accordingly. M_V however, remains constant in order to maintain the desired flow sensitivity in x-direction. Thus, the gradient amplitudes read:

$$G_R^x(\varphi) = G_R \cos(\varphi)$$

$$\begin{aligned} G_I^x(\varphi) &= \frac{2(M_R\cos(\varphi) + M_V) + A_R\cos(\varphi)w_I}{(w_O + w_I)(w_O - r)} \\ &= \frac{2(M_R\cos(\varphi) + M_V(1 - \cos(\varphi) + \cos(\varphi))) + A_R\cos(\varphi)w_I}{(w_O + w_I)(w_O - r)} \\ &= G_I\cos(\varphi) - 2M_V\frac{1 - \cos(\varphi)}{(w_O + w_I)(w_I - r)} \end{aligned}$$

$$G_O^x(\varphi) = G_O\cos(\varphi) + 2M_V\frac{1 - \cos(\varphi)}{(w_O + w_I)(w_O - r)}$$

The gradient lobes on the y-axis follow the same principles replacing $\cos(\varphi)$ with $\sin(\varphi)$. For flow sensitivity in x-direction, however, the gradient lobes on the y-axis are prepared using $M_V = 0$ to achieve flow-compensation.

A.2 MODEL-BASED RECONSTRUCTION: OPERATORS UNDER MAXWELL CORRECTION

Forward operator F of model-based image reconstruction (mdMBR) under spoke-wise Maxwell correction:

$$F_{j,l} : \mathrm{x} \mapsto \frac{1}{N_s} \sum_{s}^{N_s} P_{l,s} \mathcal{F} \left\{ \rho \cdot \exp\left(i\, \phi_{l,s}^{M} + i \sum_{d=1}^{D} v_d S_{d,l} \right) \cdot c_j \right\}$$

Derivative operator DF under spoke-wise Maxwell correction:

$$DF_{j,l}(\mathrm{x}) \begin{pmatrix} \mathrm{d}\rho \\ \mathrm{d}v_1 \\ \vdots \\ \mathrm{d}v_D \\ \mathrm{d}c_1 \\ \vdots \\ \mathrm{d}c_N \end{pmatrix} = \frac{1}{N_s} \sum_{s}^{N_s} P_{l,s}\, \mathcal{F} \left\{ \exp\left(i\phi_{l,s}^{M} \right) \exp\left(i \sum_{d=1}^{D} v_d S_{d,l} \right) \left[c_j\, \mathrm{d}\rho + \rho\, \mathrm{d}c_j + \sum_{d=1}^{D} \rho\, c_j\, i\, S_{d,l}\, \mathrm{d}v_d \right] \right\}$$

Adjoint derivative operator DF^H under spoke-wise Maxwell correction:

$$DF^H(\mathrm{x}) \begin{pmatrix} \mathrm{dy}_{1,1} \\ \vdots \\ \mathrm{dy}_{N,1} \\ \\ \vdots \\ \\ \mathrm{dy}_{1,D+1} \\ \vdots \\ \mathrm{dy}_{N,D+1} \end{pmatrix} = \begin{pmatrix} \sum_{j=1}^{N} c_j^* \left[\sum_{l=1}^{D+1} \mu_l^* \exp(-i \sum_{d=1}^{D} v_d\, S_{d,l}) \cdot \mathcal{F}^{-1}\{ P_l^H \mathrm{dy}_{j,l} \} \right] \\ \\ \Re\left(\sum_{j=1}^{N} \rho^* c_j^* \left[\sum_{l=1}^{D+1} \mu_l^*\, i\, S_{1,l} \exp(-i \sum_{d=1}^{D} v_d\, S_{d,l}) \cdot \mathcal{F}^{-1}\{ P_l^H \mathrm{dy}_{j,l} \} \right] \right) \\ \vdots \\ \Re\left(\sum_{j=1}^{N} \rho^* c_j^* \left[\sum_{l=1}^{D+1} \mu_l^*\, i\, S_{D,l} \exp(-i \sum_{d=1}^{D} v_d\, S_{d,l}) \cdot \mathcal{F}^{-1}\{ P_l^H \mathrm{dy}_{j,l} \} \right] \right) \\ \\ \sum_{l=1}^{D+1} \rho^*\, \mu_l^*\, \exp(-i \sum_{d=1}^{D} v_d\, S_{d,l}) \cdot \mathcal{F}^{-1}\{ P_l^H \mathrm{dy}_{1,l} \} \\ \vdots \\ \sum_{l=1}^{D+1} \rho^*\, \mu_l^*\, \exp(-i \sum_{d=1}^{D} v_d\, S_{d,l}) \cdot \mathcal{F}^{-1}\{ P_l^H \mathrm{dy}_{N,l} \} \end{pmatrix}$$

BIBLIOGRAPHY

[1] Krishna S Nayak et al. "Cardiovascular magnetic resonance phase contrast imaging." In: *Journal of Cardiovascular Magnetic Resonance* 17.1 (2015), p. 71 (cit. on pp. 1, 5).

[2] Stephen J Riederer et al. "Real-time interactive color flow MR imaging." In: *Radiology* 181.1 (1991), pp. 33–39 (cit. on p. 1).

[3] Hermann Körperich et al. "Flow volume and shunt quantification in pediatric congenital heart disease by real-time magnetic resonance velocity mapping: a validation study." In: *Circulation* 109.16 (2004), pp. 1987–1993 (cit. on p. 2).

[4] PD Gatehouse et al. "Real time blood flow imaging by spiral scan phase velocity mapping." In: *Magnetic Resonance in Medicine* 31.5 (1994), pp. 504–512 (cit. on p. 2).

[5] Krishna S Nayak et al. "Real-time color flow MRI." In: *Magnetic Resonance in Medicine* 43.2 (2000), pp. 251–258 (cit. on p. 2).

[6] Chia-Ying Liu et al. "Real-time color-flow MRI at 3 T using variable-density spiral phase contrast." In: *Magnetic resonance imaging* 26.5 (2008), pp. 661–666 (cit. on p. 2).

[7] Martin Uecker et al. "Image reconstruction by regularized nonlinear inversion—joint estimation of coil sensitivities and image content." In: *Magnetic Resonance in Medicine* 60.3 (2008), pp. 674–682 (cit. on pp. 2, 6, 8).

[8] Martin Uecker et al. "Real-time MRI at a resolution of 20 ms." In: *NMR in Biomedicine* 23.8 (2010), pp. 986–994 (cit. on pp. 2, 7, 11, 29).

[9] Arun A Joseph et al. "Real-time phase-contrast MRI of cardiovascular blood flow using undersampled radial fast low-angle shot and nonlinear inverse reconstruction." In: *NMR in Biomedicine* 25.7 (2012), pp. 917–924 (cit. on pp. 2, 11, 14, 15, 23, 58, 67, 83).

[10] Markus Untenberger et al. "Advances in real-time phase-contrast flow MRI using asymmetric radial gradient echoes." In: *Magnetic Resonance in Medicine* 75.5 (2016), pp. 1901–1908 (cit. on pp. 2, 11, 12, 16, 23).

[11] Zhengguo Tan et al. "Model-based reconstruction for real-time phase-contrast flow MRI: Improved spatiotemporal accuracy." In: *Magnetic Resonance in Medicine* 77.3 (2017), pp. 1082–1093 (cit. on pp. 2, 11, 14, 28, 29, 67).

[12] Juliana Serafim da Silveira et al. "Quantification of aortic stenosis diagnostic parameters: comparison of fast 3 direction and 1 direction phase contrast CMR and transthoracic echocardiography." In: *Journal of Cardiovascular Magnetic Resonance* 19.1 (2017), p. 35 (cit. on p. 2).

[13] Lars Wigström, Lars Sjöqvist, and Bengt Wranne. "Temporally resolved 3D phase-contrast imaging." In: *Magnetic Resonance in Medicine* 36.5 (1996), pp. 800–803 (cit. on p. 2).

[14] Michael Markl et al. "Time-resolved three-dimensional phase-contrast MRI." In: *Journal of Magnetic Resonance Imaging* 17.4 (2003), pp. 499–506 (cit. on p. 2).

[15] Matt A Bernstein et al. "Concomitant gradient terms in phase contrast MR: analysis and correction." In: *Magnetic Resonance in Medicine* 39.2 (1998), pp. 300–308 (cit. on pp. 2, 57, 58, 67).

[16] Paul C Lauterbur. "Image formation by induced local interactions: examples employing nuclear magnetic resonance." In: *nature* 242.5394 (1973), pp. 190–191 (cit. on p. 3).

[17] Erwin L Hahn. "Spin echoes." In: *Physical review* 80.4 (1950), p. 580 (cit. on p. 3).

[18] Axel Haase et al. "FLASH imaging: rapid NMR imaging using low flip-angle pulses." In: *Journal of magnetic resonance* 67.2 (1986), pp. 258–266 (cit. on pp. 3, 4).

[19] Matt A Bernstein, Kevin F King, and Xiaohong Joe Zhou. *Handbook of MRI pulse sequences*. Elsevier, 2004 (cit. on p. 4).

[20] Erwin L Hahn. "Detection of sea-water motion by nuclear precession." In: *Journal of geophysical research* 65.2 (1960), pp. 776–777 (cit. on p. 5).

[21] Joachim Lotz et al. "Cardiovascular flow measurement with phase-contrast MR imaging: basic facts and implementation." In: *Radiographics* 22.3 (2002), pp. 651–671 (cit. on pp. 5, 6).

[22] Shuo Zhang, Kai Tobias Block, and Jens Frahm. "Magnetic resonance imaging in real time: advances using radial FLASH." In: *Journal of Magnetic Resonance Imaging* 31.1 (2010), pp. 101–109 (cit. on p. 6).

[23] Volkert Roeloffs, Dirk Voit, and Jens Frahm. "Spoiling without additional gradients: radial FLASH MRI with randomized radiofrequency phases." In: *Magnetic Resonance in Medicine* 75.5 (2016), pp. 2094–2099 (cit. on p. 6).

[24] Kai Tobias Block, Martin Uecker, and Jens Frahm. "Undersampled radial MRI with multiple coils. Iterative image reconstruction using a total variation constraint." In: *Magnetic Resonance in Medicine* 57.6 (2007), pp. 1086–1098 (cit. on pp. 6, 84).

[25] Daniel K Sodickson and Warren J Manning. "Simultaneous acquisition of spatial harmonics (SMASH): fast imaging with radiofrequency coil arrays." In: *Magnetic Resonance in Medicine* 38.4 (1997), pp. 591–603 (cit. on p. 7).

[26] Klaas P Pruessmann et al. "SENSE: sensitivity encoding for fast MRI." In: *Magnetic Resonance in Medicine* 42.5 (1999), pp. 952–962 (cit. on p. 7).

[27] Mark A Griswold et al. "Generalized autocalibrating partially parallel acquisitions (GRAPPA)." In: *Magnetic Resonance in Medicine* 47.6 (2002), pp. 1202–1210 (cit. on p. 7).

[28] Martin Uecker, Shuo Zhang, and Jens Frahm. "Nonlinear inverse reconstruction for real-time MRI of the human heart using undersampled radial FLASH." In: *Magnetic Resonance in Medicine* 63.6 (2010), pp. 1456–1462 (cit. on p. 7).

[29] Shuo Zhang et al. "Real-time cardiovascular magnetic resonance at high temporal resolution: radial FLASH with nonlinear inverse reconstruction." In: *Journal of Cardiovascular Magnetic Resonance* 12.1 (2010), p. 39 (cit. on pp. 7, 11).

[30] Anatolii Borisovich Bakushinsky and M Yu Kokurin. *Iterative methods for approximate solution of inverse problems*. Vol. 577. Springer Science & Business Media, 2005 (cit. on p. 8).

[31] Arun A Joseph et al. "Real-time flow MRI of the aorta at a resolution of 40 msec." In: *Journal of Magnetic Resonance Imaging* 40.1 (2014), pp. 206–213 (cit. on p. 11).

[32] Matt A Bernstein, Ann Shimakawa, and Norbert J Pelc. "Minimizing TE in moment-nulled or flow-encoded two-and three-dimensional gradient-echo imaging." In: *Journal of Magnetic Resonance Imaging* 2.5 (1992), pp. 583–588 (cit. on pp. 12, 18, 22, 87).

[33] Zhengguo Tan et al. "An eigenvalue approach for the automatic scaling of unknowns in model-based reconstructions: Application to real-time phase-contrast flow MRI." In: *NMR in Biomedicine* 30.12 (2017), e3835 (cit. on pp. 13, 30).

[34] Kai Tobias Block and Martin Uecker. "Simple method for adaptive gradient-delay compensation in radial MRI." In: *Proceedings of the 19th Annual Meeting of ISMRM*. Vol. 19. 2011, pp. 2816–2816 (cit. on p. 16).

[35] Dana C Peters, J Andrew Derbyshire, and Elliot R McVeigh. "Centering the projection reconstruction trajectory: reducing gradient delay errors." In: *Magnetic Resonance in Medicine* 50.1 (2003), pp. 1–6 (cit. on p. 16).

[36] Sebastian Rosenzweig, H Christian M Holme, and Martin Uecker. "Simple auto-calibrated gradient delay estimation from few spokes using Radial Intersections (RING)." In: *Magnetic Resonance in Medicine* 81.3 (2019), pp. 1898–1906 (cit. on p. 16).

[37] Jakob Klosowski and Jens Frahm. "Image denoising for real-time MRI." In: *Magnetic Resonance in Medicine* 77.3 (2017), pp. 1340–1352 (cit. on p. 17).

[38] Jaakko Astola, Petri Haavisto, and Yrjo Neuvo. "Vector median filters." In: *Proceedings of the IEEE* 78.4 (1990), pp. 678–689 (cit. on p. 18).

[39] Steffi Dreha-Kulaczewski et al. "Identification of the upward movement of human CSF in vivo and its relation to the brain venous system." In: *Journal of Neuroscience* 37.9 (2017), pp. 2395–2402 (cit. on pp. 20, 73).

[40] Steffi Dreha-Kulaczewski et al. "Respiration and the watershed of spinal CSF flow in humans." In: *Scientific reports* 8.1 (2018), pp. 1–7 (cit. on pp. 20, 73).

[41] Gökmen Aktas et al. "Spinal CSF flow in response to forced thoracic and abdominal respiration." In: *Fluids and Barriers of the CNS* 16.1 (2019), p. 10 (cit. on pp. 20, 73).

[42] Jost M Kollmeier et al. "Real-time multi-directional flow MRI using model-based reconstructions of undersampled radial FLASH–A feasibility study." In: *NMR in Biomedicine* (2019) (cit. on pp. 21, 22, 28).

[43] Norbert J Pelc et al. "Encoding strategies for three-direction phase-contrast MR imaging of flow." In: *Journal of Magnetic Resonance Imaging* 1.4 (1991), pp. 405–413 (cit. on p. 25).

[44] Charles L Dumoulin et al. "Simultaneous acquisition of phase-contrast angiograms and stationary-tissue images with Hadamard encoding of flow-induced phase shifts." In: *Journal of Magnetic Resonance Imaging* 1.4 (1991), pp. 399–404 (cit. on p. 25).

[45] William K Pratt, Julius Kane, and Harry C Andrews. "Hadamard transform image coding." In: *Proceedings of the IEEE* 57.1 (1969), pp. 58–68 (cit. on p. 25).

[46] Kevin M Johnson and Michael Markl. "Improved SNR in phase contrast velocimetry with five-point balanced flow encoding." In: *Magnetic Resonance in Medicine* 63.2 (2010), pp. 349–355 (cit. on p. 27).

[47] Elizabeth J Nett et al. "Four-dimensional phase contrast MRI with accelerated dual velocity encoding." In: *Journal of Magnetic Resonance Imaging* 35.6 (2012), pp. 1462–1471 (cit. on p. 27).

[48] Hojin Ha et al. "Multi-VENC acquisition of four-dimensional phase-contrast MRI to improve precision of velocity field measurement." In: *Magnetic Resonance in Medicine* 75.5 (2016), pp. 1909–1919 (cit. on p. 27).

[49] Kristen M Thyng et al. "True colors of oceanography: Guidelines for effective and accurate colormap selection." In: *Oceanography* 29.3 (2016), pp. 9–13 (cit. on p. 37).

[50] Peter Kovesi. "Good colour maps: How to design them." In: *arXiv preprint arXiv:1509.03700* (2015) (cit. on p. 37).

[51] Samuel M Song et al. "Noise reduction in three-dimensional phase-contrast MR velocity measurementsl." In: *Journal of Magnetic Resonance Imaging* 3.4 (1993), pp. 587–596 (cit. on p. 45).

[52] Julia Busch et al. "Reconstruction of divergence-free velocity fields from cine 3D phase-contrast flow measurements." In: *Magnetic Resonance in Medicine* 69.1 (2013), pp. 200–210 (cit. on p. 45).

[53] Frank Ong et al. "Compressed sensing 4D flow reconstruction using divergence-free wavelet transform." In: *Proceedings of international society for magnetic resonance in medicine*. Vol. 22. 2014, p. 0326 (cit. on p. 45).

[54] Emrah Bostan et al. "Improved variational denoising of flow fields with application to phase-contrast MRI data." In: *IEEE Signal Processing Letters* 22.6 (2014), pp. 762–766 (cit. on pp. 45, 84).

[55] Stefanie Winkelmann et al. "An optimal radial profile order based on the Golden Ratio for time-resolved MRI." In: *IEEE transactions on medical imaging* 26.1 (2006), pp. 68–76 (cit. on pp. 46, 47).

[56] Stefan Wundrak et al. "Golden ratio sparse MRI using tiny golden angles." In: *Magnetic Resonance in Medicine* 75.6 (2016), pp. 2372–2378 (cit. on p. 47).

[57] Matt A Bernstein and Thomas K Foo. *MRA image produced by temporal flow data sharing*. US Patent 5,435,303. 1995 (cit. on p. 50).

[58] Hung-Yu Lin et al. "Shared velocity encoding: a method to improve the temporal resolution of phase-contrast velocity measurements." In: *Magnetic Resonance in Medicine* 68.3 (2012), pp. 703–710 (cit. on p. 50).

[59] Michael Markl et al. "4D flow MRI." In: *Journal of Magnetic Resonance Imaging* 36.5 (2012), pp. 1015–1036 (cit. on pp. 58, 84).

[60] Petter Dyverfeldt et al. "4D flow cardiovascular magnetic resonance consensus statement." In: *Journal of Cardiovascular Magnetic Resonance* 17.1 (2015), p. 72 (cit. on pp. 58, 84).

[61] Hassan Haji-Valizadeh et al. "Highly accelerated, real-time phase-contrast MRI using radial k-space sampling and GROG-GRASP reconstruction: a feasibility study in pediatric patients with congenital heart disease." In: *NMR in Biomedicine* 33.5 (2020), e4240 (cit. on pp. 58, 84).

[62] Tianliang Gu et al. "PC VIPR: a high-speed 3D phase-contrast method for flow quantification and high-resolution angiography." In: *American Journal of Neuroradiology* 26.4 (2005), pp. 743–749 (cit. on p. 58).

[63] Joseph Katz. *Introductory fluid mechanics*. Cambridge University Press, 2010 (cit. on p. 72).

[64] Thomas Brinker et al. "A new look at cerebrospinal fluid circulation." In: *Fluids and Barriers of the CNS* 11.1 (2014), pp. 1–16 (cit. on p. 73).

[65] Mitsunori Matsumae et al. "Changing the currently held concept of cerebrospinal fluid dynamics based on shared findings of cerebrospinal fluid motion in the cranial cavity using various types of magnetic resonance imaging techniques." In: *Neurologia medico-chirurgica* 59.4 (2019), p. 133 (cit. on p. 73).

[66] Helene Benveniste, Hedok Lee, and Nora D Volkow. "The glymphatic pathway: waste removal from the CNS via cerebrospinal fluid transport." In: *The Neuroscientist* 23.5 (2017), pp. 454–465 (cit. on p. 73).

[67] Steffi Dreha-Kulaczewski et al. "Inspiration is the major regulator of human CSF flow." In: *Journal of Neuroscience* 35.6 (2015), pp. 2485–2491 (cit. on p. 73).

[68] Krishna S Nayak. "Response to Letter to the Editor:"Nomenclature for real-time magnetic resonance imaging"." In: *Magnetic Resonance in Medicine* 82.2 (2019), pp. 525–526 (cit. on p. 83).

[69] Zoran Stankovic et al. "4D flow imaging with MRI." In: *Cardiovascular diagnosis and therapy* 4.2 (2014), p. 173 (cit. on p. 84).

[70] Dirk Voit et al. "Rapid and motion-robust volume coverage using cross-sectional real-time MRI." In: *Magnetic Resonance in Medicine* 83.5 (2020), pp. 1652–1658 (cit. on p. 84).

[71] Leonid I Rudin, Stanley Osher, and Emad Fatemi. "Nonlinear total variation based noise removal algorithms." In: *Physica D: nonlinear phenomena* 60.1-4 (1992), pp. 259–268 (cit. on p. 84).

[72] Peter Blomgren and Tony F Chan. "Color TV: total variation methods for restoration of vector-valued images." In: *IEEE transactions on image processing* 7.3 (1998), pp. 304–309 (cit. on p. 84).

[73] Florian Knoll et al. "Parallel imaging with nonlinear reconstruction using variational penalties." In: *Magnetic Resonance in Medicine* 67.1 (2012), pp. 34–41 (cit. on p. 84).

[74] Aiqi Sun et al. "Real-time phase-contrast flow cardiovascular magnetic resonance with low-rank modeling and parallel imaging." In: *Journal of Cardiovascular Magnetic Resonance* 19.1 (2017), p. 19 (cit. on p. 84).

[75] Aiqi Sun et al. "4D real-time phase-contrast flow MRI with sparse sampling." In: *2017 39th Annual International Conference of the IEEE Engineering in Medicine and Biology Society (EMBC)*. IEEE. 2017, pp. 3252–3255 (cit. on p. 84).

ACKNOWLEDGMENTS

Allen voran bedanke ich mich bei Prof. Dr. Jens Frahm für die Möglichkeit, diese Arbeit in der Abteilung *Biomedizinische NMR* anfertigen zu können. Seine gute Betreuung, seinen fachlichen Rat, sowie seinen ansteckenden Enthusiasmus für das Feld der MRT weiß ich sehr zu schätzen.
Darüber hinaus danke ich Arun Joseph, Zhengguo Tan und Dietmar Merboldt für wertvolle Einblicke in die Echtzeit- und Fluss-MRT und Steffi Dreha-Kulaczewski, die mir das spannende Feld der CSF Dynamik eröffnete. In gleicher Weise danke ich allen weiteren Kollegen der *Biomedizinischen NMR* für ein angenehmes Arbeitsklima und dafür, dass sie mir stets mit Rat und Tat zur Seite standen - insbesondere Dirk, Jakob, Sascha, Kurt, Sabine und Volkert. Für die gute Zusammenarbeit und die gemeinsame Zeit bin ich außerordentlich dankbar.
Des Weiteren bin ich meinen Probanden zum Dank verpflichtet, die ich nicht namentlich nenne, sowie den Mitarbeitern der Werkstätten des MPI BPC, die mir tatkräftig halfen neue Flussphantome zu realisieren.
Nicht zuletzt möchte ich meinen Eltern für eine sorgenfreie Studienzeit danken, sowie meiner Schwester, Annette, und Katharina für all die Unterstützung.